

Xinyue Li

Xinyue Li

Radboud Dissertation Series

ISSN: 2950-2772 (Online); 2950-2780 (Print)

Published by RADBOUD UNIVERSITY PRESS Postbus 9100, 6500 HA Nijmegen, The Netherlands www.radbouduniversitypress.nl

Design: Proefschrift AIO | Guus Gijben

Cover artwork: Proefschrift AIO | Guntra Laivacuma

Printing: DPN Rikken/Pumbo

ISBN: 9789465151458

DOI: 10.54195/9789465151458

Free download at: https://doi.org/10.54195/9789465151458

© 2025 Xinyue Li

RADBOUD UNIVERSITY PRESS

This is an Open Access book published under the terms of Creative Commons Attribution-Noncommercial-NoDerivatives International license (CC BY-NC-ND 4.0). This license allows reusers to copy and distribute the material in any medium or format in unadapted form only, for noncommercial purposes only, and only so long as attribution is given to the creator, see http://creativecommons.org/licenses/by-nc-nd/4.0/.

Proefschrift ter verkrijging van de graad van doctor

aan de Radboud Universiteit Nijmegen

op gezag van de rector magnificus prof. dr. J.M. Sanders,

volgens besluit van het college voor promoties

in het openbaar te verdedigen op

donderdag 6 november 2025 om 12.30 uur precies

door

Xinyue Li geboren op 11 januari 1992 te Qian'an, China

Promotoren:

Prof. dr. T.H.M. Rasing

Prof. dr. J. Xu (Nankai University, China)

Prof. dr. A.V. Kimel

Manuscriptcommissie:

Prof. dr. P.C.M. Christianen

Prof. dr. X. Bu (Nankai University, China)

Prof. dr. P. Naumov (New York University Abu Dhabi, Verenigde Arabische Emiraten)

Dissertation to obtain the degree of doctor

from Radboud University Nijmegen

on the authority of the Rector Magnificus prof. dr. J.M. Sanders,

according to the decision of the Doctorate Board

to be defended in public on

Thursday, November 6, 2025

at 12.30 pm

by

Xinyue Li

born on January 11, 1992

in Qian'an (China)

Supervisors:

Prof. dr. T.H.M. Rasing

Prof. dr. J. Xu (Nankai University, China)

Prof. dr. A.V. Kimel

Manuscript Committee:

Prof. dr. P.C.M. Christianen

Prof. dr. X. Bu (Nankai University, China)

Prof. dr. P. Naumov (New York University Abu Dhabi, United Arab Emirates)

Table of Contents

Cł	papter 1	
ln	troduction	13
	1.1 Thermosalient phenomena	14
	1.1.1 Thermosalient organic materials	14
	1.1.2 Structural phase transitions in thermosalient organic crystals	15
	1.2. Probing the phase transition in 4-DBpFO	16
	1.2.1 Thermosalient phase transition in 4-DBpFO	20
	1.2.2 Optical probing of charge and lattice dynamics	22
	1.3 Scope of thesis	25
Cł	napter 2	
M	aterial characterization and experimental approaches	29
	2.1 Crystallization	30
	2.2 Crystal characterizations	31
	2.2.1 Fluorescence microscopy	31
	2.2.2 Hot stage microscopy	32
	2.2.3 Profilometry	32
	2.2.4 Single crystal X-ray diffraction	33
	2.3 Experimental techniques and setups	33
	2.3.1 Raman spectroscopy setup	33
	2.3.2 Birefringence setup	35
	2.3.3 Absorbance setup	37
	2.3.4 FLARE setup	39
	2.4 Pump-probe techniques	40
	2.4.1 Optical pump-probe	40
	2.4.2 Home-built pump-probe setup	41
	2.4.3 Knife-edge method	43
	2.4.4 Fluence calculation	44
	2.4.5 THz pump-optical probe	44

Cha	pter	3
-----	------	---

Temperature dependent optical birefringence and fluorescence of two	
polymorphs of 4-DBpFO	49
3.1 Introduction	50
3.2 Crystalline structure of α and α phase 4-DBpFO	50
3.3 Anisotropic optical transmission in $lpha$ phase 4-DBpFO	54
3.4 Fluorescence emission of α phase 4-DBpFO	55
3.5 Static birefringence of α and α phase 4-DBpFO	57
3.6 Linear birefringence change across the thermosalient phase transition in α phase 4-DBpFO	60
3.7 Conclusion and outlook	61
Chapter 4	
Raman spectroscopic study of the thermosalient phase transition in	
4-DBpFO single crystals	65
4.1 Introduction	66
4.2 Polarization dependent Raman spectra	69
4.3 Temperature dependent Raman spectra	73
4.4 Molecular dynamics simulated Raman spectra	77
4.5 Line scan across phase boundary	80
4.6 Simulated spectrum for the transition order parameter	82
4.7 Conclusion and outlook	85
Chapter 5	
Optical pump-probe study of the phase transition in 4-DBpFO	
single crystals	87
5.1 Introduction	88
5.2 Static spectroscopic study of 4-DBpFO	88
5.3 Time-resolved transmission changes	90
5.4 Temperature dependent polarization rotation dynamics across the phase transition	95
5.5 Pump power dependent polarization rotation change	99
5.6 Conclusion and outlook	103

Chapter 6

THz pump-optical probe study of the thermosalient phase transition in	
4-DBpFO single crystals	105
6.1 Introduction	106
6.2 Simulation of photoinduced phase transition in 4-DBpFO	106
6.3 THz pump driven phase transition using FLARE	108
6.4 Time resolved THz pump-optical probe experiments	111
6.4.1 Pump polarization dependence	112
6.4.2 Time-resolved THz induced polarization rotation	114
6.4.3 Pump power dependence	117
6.5 THz induced SHG across phase transition	119
6.6 Conclusion and outlook	121
Summary and outlook	125
Samenvatting en vooruitzicht	129
Research Data Management	133
Acknowledgements	135
List of Publications	141
Curriculum Vitae	143
References	145



Chapter 1

Introduction

Smart materials^{1,2} that can respond to changes in their environment, such as pressure, temperature, humidity, light, magnetic field or pH, have been the subject of a plethora of investigations thanks to their various possibilities for applications^{2,3}. For example, self-healing materials^{4,5} and shape-memory materials^{6,7} have been extensively studied in terms of their potentials in automotive engines⁸, robots⁹ and actuators. Salient materials, typically responsive to physical stimuli such as pressure, temperature and light, are the emerging stars of the smart material family due to their fast mechanical response and robust exhibition of actuation¹⁰. These materials are categorized as thermosalient¹¹, photosalient¹² and mechanosalient materials, corresponding to the three external stimuli: heat, light and mechanical force. The collection of mechanical effects, usually observed as rapid self-propulsion, splintering, or even explosion that leads to complete disintegration, exhibited by these salient crystals are defined as thermosalient, photosalient and mechanosalient phenomena. The more recent research has focused on exploring the dynamical and adaptive responses to external stimuli, all of which are of paramount importance for the next-generation smart materials¹³.

Parts of this chapter are adapted from: S. Semin, X. Li, et al. "Nonlinear Optical Properties and Applications of Fluorenone Molecular Materials" Adv. Optical Mater. 2021, 9, 2100327

1.1 Thermosalient phenomena

1.1.1 Thermosalient organic materials

The very first thermosalient material was reported in 1983¹⁴ in a study of singlecrystal-to-single-crystal (SCSC) phase transition, where a sudden discontinuous expansion was observed upon heating, leading to a jumping behavior. Thus, thermosalient crystals are also colloquially called jumping crystals. Soon, a reversible SCSC phase transition accompanied with a jumping effect was reported for another organic crystal and the concept of thermosalient crystal was coined 15. From there on, more studies have been delivered on discovering thermosalient materials 16-18. Till now, there are more than 30 compounds that are reported to be able to form thermosalient crystals. Figure 1.1 presents a summary of all these compounds till 2015¹⁹.

Thermosalient materials include a large variety of compound types, such as organic molecules, organometallic compounds and metal complexes, all of which share the property of converting thermal energy into mechanical energy in the crystalline state²⁰. Thermosalient organic crystals, composed of discrete and highly ordered molecules bound through intermolecular forces, exhibit mechanically responsive properties that have positioned them as a platform for devices with a wide range of flexibility and complexity¹³.

Thermosalient organic crystals provide better performance in terms of response time and work density compared to traditional actuators such as electroactive polymers, piezo-actuators and thermal actuators¹³. The fastest thermosalient response was reported to be at the scale of a few microseconds²¹, second to the photosalient response¹³. The work density exerted by the jumping behavior is up to 270 J/kg in thermosalient organic crystals²², much higher than that of microelectromechanical systems²³. Thanks to the almost infinite possibilities on molecular composition and crystalline structures, thermosalient organic crystals also feature low-cost and easy fabrication comparing to metallic materials.

However, an inherent drawback that has precluded wider implementation of thermosalient organic crystals thus far, is their brittleness, resulting from the sudden structural change, which renders them incapable of ensuring mechanical compliance required for devices²⁴. The potential for practical applications of the thermosalient effect for thermal-to-mechanical energy conversion requires elucidation of the mechanism and detailed understanding of the relationship

between structural changes at the molecular level and their expression at the macrostructural level.

Thus, the most challenging task in this field is to first, find a robust thermosalient material that can maintain its integrity through the temperature cycles; second, understand the mechanism of this effect and achieve controllable motions in this type of material²⁵.

Figure 1.1. Molecular structures of reported thermosalient crystals¹⁹.

1.1.2 Structural phase transitions in thermosalient organic crystals

To understand the thermosalient effect and provide guidance for future applications, a lot of research has been done, utilizing the methods of thermal analysis (Thermogravimetric analysis²⁰, Differential scanning calorimetry²⁶), structural analysis like powder X-ray diffraction (XRD)²⁷ and single crystal XRD²⁸, and microscopic and spectroscopic analysis using hot stage microscopy²⁹ and Raman spectroscopy³⁰. So far, it is generally accepted that the origin of this phenomenon is related to the generation of mechanical stresses in the crystal. These stresses accumulate during an induction period due to structural strain before critical conditions of their relaxation via dislocation glide, twinning, and/or fracture are achieved. The jumping occurs as a result of instantaneous release of the colossal strain that has accumulated in the crystal interior. A rapid structural transition is related to large shear strain and shear stresses¹⁹.

Some essential concomitant features of thermosalient organic crystals²⁰:

- they present a first-order phase transition associated with a sudden change of cell parameters and
- they show a negative thermal expansion in at least one direction

Note that there is one case where a jumping behavior is reported without a phase transition happening²⁷.

The thermosalient phase transition is often compared to a martensitic phase transition, which can also be induced by temperature³¹. While both the martensitic phase transition and the thermosalient phase transition involve reversible changes in material properties, they occur in different types of materials (crystalline metals/ alloys vs. organic crystals) and are driven by different underlying mechanisms (structural transformation vs. stress release). Moreover, thermosalient phase transition also features two magnitudes faster transition rate than that of martensitic phase transition³¹.

In 2019, my predecessor Yulong Duan serendipitously discovered that the di([1,1'-biphenyl]-4-yl)-fluorenone (4-DBpFO) single crystal, originally designed and grown for its potential nonlinear optical properties, presented a very robust thermosalient crystal, that allowed cycling through its phase transition for hundreds of cycles without any noticeable degradation nor explosion²². In the following, the fluorenone materials and their linear and nonlinear optical properties will first be introduced, before we start focusing on the main topic of this thesis: the origin of this fascinating thermosalient effect.

1.2. Probing the phase transition in 4-DBpFO

Fluorenone based materials serve as a new promising class of molecular materials for nonlinear optics³². These derivatives can be easily synthesized by metal catalyzed condensations such as Suzuki coupling reactions. The superiority of fluorenone based derivatives for nonlinear optics is not only due to the high hyperpolarizability of single molecules but also because of the fact that they can exist in different non-centrosymmetric crystalline forms at room temperature³³.

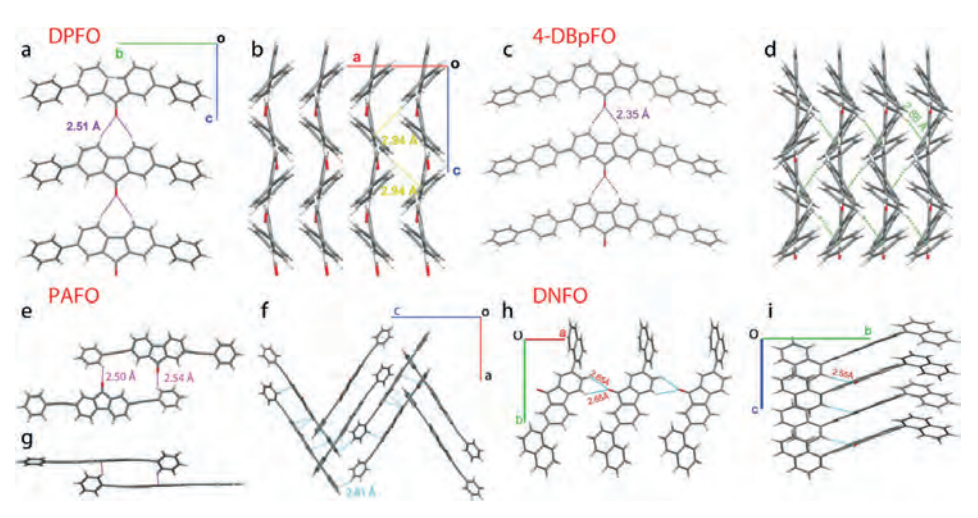


Figure 1.2. Molecular and crystallographic structure of fluorenone based materials: DPFO a) Hydrogen-bonded DPFO molecular chains for second-order nonlinear optical properties. b) Packed molecular columns along the a-axis, viewed along the b-axis. 4-DBpFO c) The hydrogen bonded molecular chains of 4-DBpFO. The dipole of each individual molecule accumulates to contribute to a permanent dipole of the molecular chain, as represented by the arrow. d) The zigzag C-H··· π interactions attaching the molecular chains in a non-centrosymmetric way. PAFO Crystal structure of PAFO in the a phase. e) The front view and f) the top view of the PAFO molecules with two different configurations. g) The unit cell of PAFO crystals in the α -phase. DNFO Crystal structure of DNFO in the 1a-phase. h) The intermolecular C=0⋅⋅⋅ H hydrogen bonds attach molecules along the a-axis (view along c-axis) i) C=O····H attraction induces the molecular chains to pack along the c-axis (view along a-axis).

By adjusting the ratio of good and poor solvents in the crystallization process using the liquid diffusion method, multiple polymorphs of 4-DBpFO molecule can be obtained, as summarized in Table 1.1. Notably, within the same crystalline phase, which shares an identical crystal structure, different morphologies may emerge. For instance, α' phase 4-DBpFO crystals can form as either microbelts or microplates, both of which fall in Ccm2₁ space group. Similarly, crystals exhibiting the same morphology, such as the microplates listed in Table 1.1, may belong to different phases. In other words, one cannot identify the phase of a crystal by its morphology.

 α' phase 4-DBpFO crystals have been thoroughly studied for its excellent second order nonlinearity originating from its non-centrosymmetric architecture ^{34,35}.

The α phase 4-DBpFO, while featuring a centrosymmetric structure, shows salient response to temperature change²². The thermosalient effect involves a reversible structural phase transition upon heating. In this thesis, we focus on studying the origin and the dynamics of the thermosalient phase transition in 4-DBpFO by employing multiple spectroscopic methods.

4-DBpFO crystals	Morphology	Space group	Point group	Centrosymmetry	Phase transition
α'-phase	microbelts and microplates	Ccm2 ₁	mm2	non- centrosymmetric	None
lpha-phase	microplates	Pnma		centrosymmetric	Thermosalient

Table 1.1. Polymorphs of 4-DBpFO under ambient conditions.

panoamo	Maximum	Maximum	Stokes	Quantum yield [%]	ield [%]	- Space group	Effective nonlinearity	Laser damage	Deferences
	absorption [nm]	absorption [nm] fluorescence [nm]	shift [cm ⁻¹]	Solution	Solid	Space group	value [pm V ⁻¹]	[m] cm ⁻²]	secielelle.
	433	537		21	28	Cmc2 ₁ ; Pbca	0.12 ^{a)}	50 (at 1350 nm)	J.Xu et al. ^[56] , M.Savioni
DPFO									פופו
	441	595	5216	9. 9.	35.8	Cmc2 ₁ ; Pnma	25.7 (800 nm)	3.0 (800-900 nm)	Y.Duan et al. [57]
4-DBpFO									
	300					Pca2 ₁ ; P2 ₁ /a	0.3 (800 nm) ^{b)} 4.8 (740 nm) ^{b)}		X.Li et al ^[100]
PAFO									
	427	553	5511	3.80	7.9	Pca2 ₁ ; Pc; P2 ₁ / c			C. Ju et al. ^[95]
1-DNFO									
999	445	559	4583	3.30	6.21	Pbca; P2 ₁ /n			C. Ju et al. ^[95]
2-DNFO									

 Table 1.2. Summary of the aggregation induced emission and SHG properties of selected fluorenone-based derivatives 33

1.2.1 Thermosalient phase transition in 4-DBpFO

The drastic shape deformation of 4-DBpFO crystals²² is accompanied by a strong mechanical response and a structural transformation inside the crystal lattice, where the molecules move and drive the structural change cooperatively. The deformation of the single crystal can be reproducibly controlled by many heating/ cooling cycles without destroying the crystal. Upon the low-temperature phase to high-temperature phase transition, a crystal with a size of 200 × 200 × 50 μm³ could kick a glass bead (0.15 mg), causing it to fly several centimeters away. The work density was estimated to be as high as 270 J/kg²².

The transition involves a small conformational change, which propagates through the crystal but can be frozen and even reversed by finely tuning the temperature. Moreover, this shear deformation can be observed along two orthogonal crystal sides that appear to be connected to its symmetrical and layered structure. The phase transition of 4-DBpFO single crystal can appear in two ways: one phase boundary and two phase boundaries. The phase boundaries can be temperature controlled to move forward, backward, or to halt, benefitting from the stored elastic energy between the parallel boundaries. Thus, it is possible to fix the phase boundary during its propagation³⁶. This property of the phase transition is strategically used in Chapter 4 where Raman spectra are obtained as function of an order parameter by making a line scan through the phase boundary while the crystal is fixed at a certain temperature.

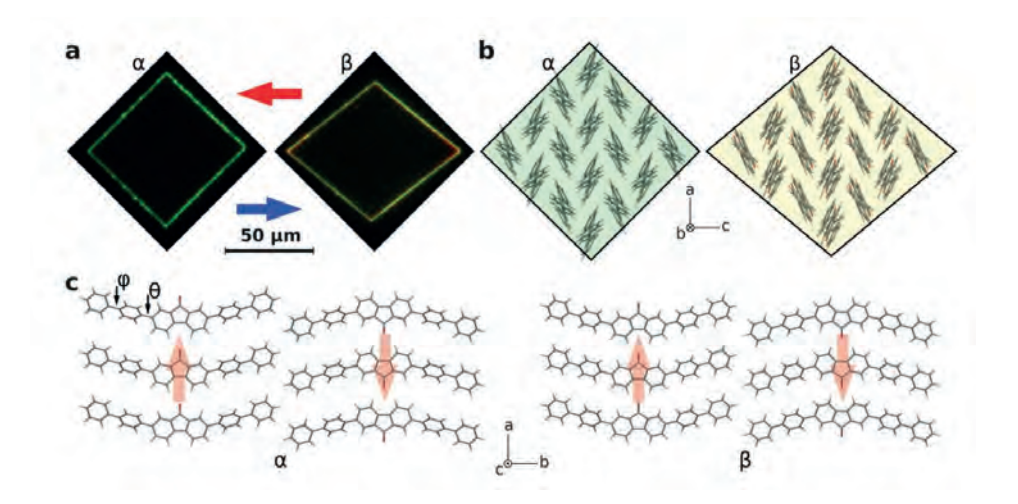


Figure 1.3. Crystal structure and morphology of the α -phase and β -phase 4-DBpFO. a) Fluorescence images of a typical macroscopic single crystal of the α -phase (at room temperature) and β-phase (at 178 °C), under UV light excitation. b) Molecular packing viewed along the b-direction of the two phases, c) Molecular packing viewed along the c-direction. The molecular arrangement shows an overlapping layered structure along the b-axis with anti-parallel dipoles. The light red arrows show the direction of the molecular dipoles. The structure shows that there is ample space between molecules, which is beneficial for the rotation of the flat planes in the molecules during the phase transition. Notice that the angles between the axes are all 90° in the α -phase while the α -angle is 93° in the β -phase. φ is the dihedral angle between the inner and outer phenyl rings and ϑ is the dihedral

angle between the inner phenyl rings and the rigid center.

The structural phase transition in the α -phase of 4-DBpFO does not fall in any of the three classes that were defined by the molecular shape and their packing structures²⁵. Instead, it shows a pronounced anisotropic crystal shape change with a shrinkage in one direction and an expansion in the perpendicular direction. The major shear deformation is caused by the in-plane anisotropic lattice expansion, which generate a shear force parallel to the rhombic crystal side.

The structural phase transition in 4-DBpFO single crystal that is induced by temperature change belongs to the martensitic phase transition³⁷ as there is no change in composition and the phase transition is reversible in terms of its mechanical and thermal properties.

4-DBpFO, featuring a robust and reversible thermosalient phase transition, is chosen as a prototype to study the origin and dynamics of this structural phase transition using several spectroscopic and ultrafast pump-probe techniques.

1.2.2 Optical probing of charge and lattice dynamics

In order to understand how light can probe lattice dynamics, we apply an approach based on thermodynamics. In particular, the first law of thermodynamics states that

$$dU = dQ + dW (1.1)$$

where U is the internal energy of the system, Q is the heat added to the system and W is the output work done by the system.

Here we assume for simplicity that there is no irreversible energy transfer of energy between light and medium. It means that the entropy of the whole system in the process of light-matter interaction does not change and dS=0. Consequently, dQ = TdS = 0. The energy of light-matter interaction in the electric dipole approximation is equal to

$$dW = \mathbf{E}d\mathbf{P} \tag{1.2}$$

where ${f E}$ is the electric field of light and ${f P}$ is the polarization induced in the material by this electric field.

If the electric field of light is a small parameter, i.e. the field is much smaller than interatomic electric fields (~20 V/nm), we can expand the polarization in series with respect to powers of \mathbf{E} :

$$P_{i} = \varepsilon_{0} \chi_{ij} E_{j} + \chi_{ijk}^{(2)} E_{j} E_{k} + \chi_{ijkl}^{(3)} E_{j} E_{k} E_{l} + \dots$$
 (1.3)

where $arepsilon_0$ is the fundamental constant representing the dielectric permittivity of is the linear optical susceptibility, and $\chi^{(2)}_{iik}$ vacuum, χ_{ij} nonlinear susceptibilities.

Limiting the consideration to the first term in the series means that we apply the approximation of linear optics. In this approximation, one also writes that

$$D_i = \varepsilon_0 \varepsilon_{ij} E_j \tag{1.4}$$

where D_i is the i-th component of the vector of electric displacement and $arepsilon_{
m ij}$ is the dielectric permittivity ($arepsilon_{ii}=\chi_{ii}+1$ and $arepsilon_{ij}=\chi_{ij}$ if $i
eq j)^{38}$.

Any lattice distortion can be represented by a strain tensor σ_{ij} . If lattice dynamic results in a specific σ_{ij} , which shows up in the interaction of light and matter, we can write

$$\varepsilon_{ij} = \chi_{ijkl}^{(EO)} \sigma_{ij} \tag{1.5}$$

where $\chi^{(EO)}_{ijkl}$ is a phenomenological tensor, which describes how lattice distortion links to optical properties (elasto-optical tensor)³⁹.

Since the crystals studied in this work have no magnetic order, the optical properties of the medium must be invariant with respect to time-reversal. Since strain is also invariant under time-reversal, the contributions of $\chi^{(EO)}_{ijkl}\sigma_{ij}$ to ε_{ij} must be also time-reversal invariants. From this it can be shown that $\chi^{(EO)}_{ijkl}\sigma_{ij}$ can only contribute to the symmetric part of the dielectric permittivity tensor $\varepsilon_{ij}^{(s)} = \varepsilon_{ij}^{(s)}$.

Assume for simplicity that light propagates along the z-axis and the electromagnetic field is represented by a plane wave, implying that $E_z=0.$ It can be shown that, if the strain changes the ratio between $\varepsilon_{xx}^{(s)}$ and $\varepsilon_{yy}^{(s)}$ or induces $\varepsilon_{xy}^{(s)}$, the polarization of initially linearly polarized light propagating along the z-axis will acquire ellipticity. The effect is known as linear birefringence and is discussed and used in Chapters 3, 5 and 6. If absorption cannot be neglected, the polarization of light will rotate due to linear dichroism.

In order to detect dynamic changes of σ_{ii} due to lattice vibrations, one has to measure the polarization ellipticity and rotation with temporal resolution. In the experiments presented in this thesis, no effect of (laser-induced) lattice vibrations could be resolved in the pump-probe birefringence experiments. Optical excitation of electrons can also lead to dynamic changes in ε_{ij} directly. This is studied in Chapter 5 where optical pump- probe is employed to disclose the time-resolved charge dynamics by probing the polarization rotation as a function of delay time.

Alternatively, lattice dynamics can be studied in the frequency domain. For instance, let us consider a particular lattice vibration mode, which preserves the translational symmetry of the crystal lattice and induces a mechanical deformation σ . Such a vibration would correspond to a phonon at the center of the Brillouin zone.

By expanding the dielectric permittivity with respect to σ one obtains

$$\varepsilon(\sigma,\omega) = \varepsilon(0,\omega) + \frac{d\varepsilon}{d\sigma}\sigma + \frac{1}{2}\frac{d^2\varepsilon}{d\sigma^2}\sigma^2 + \dots$$
(1.6)

After defining the electric field of the incident light as $E\left(t\right)=E_{m}\exp\left(i\omega t\right)+c.c.$ and the deformation as $\sigma=\sigma_{m}\exp\left(i\Omega t\right)$, one can see that if $\frac{d\varepsilon}{d\sigma}\neq0$, the net dipole moment (i.e. electric polarization) induced in the medium by the electric field of light $P=\varepsilon_{0}\frac{d\varepsilon}{d\sigma}\sigma E$ must have two additional spectral components at frequencies $\omega\pm\Omega$. Hence, after interaction with the medium the spectrum of light changes as a result of scattering of light waves (photons) by waves of lattice vibrations (phonons). Lattice vibrations of crystals consisting of two or more types of atoms are characterized by two types of branches, representing acoustic and optical phonons, respectively. Historically, scattering of light by optical phonons is called Raman scattering, while scattering of light by acoustic phonons is called Brillouin scattering. These explanations can also be expanded to the case of anisotropic media, where $\hat{\varepsilon}$ is the dielectric permittivity tensor. The derivative $\frac{d\hat{\varepsilon}}{d\sigma}$ is called the Raman tensor.

In a Raman experiment, the light from a laser is scattered by lattice vibrations (phonons). If the scattering results in a decrease of the frequency of light (increase of the wavelength), the effect is called Stokes-Raman scattering 40 . In this effect, a light wave at the frequency ω is inelastically scattered by the lattice – its frequency changes to $\omega-\Omega$ and lattice vibrations at the frequency Ω are launched. The scattering resulting in an increase of the light frequency (decrease of the wavelength) is called Anti-Stokes-Raman scattering. In this case, lattice vibrations at the frequency Ω are quenched upon scattering of a light wave at the frequency ω into a wave with the frequency $\omega+\Omega$. This refers to Chapter 4 where Raman experiments on 4-DBpFO are discussed.

Light can also detect dynamics in media employing nonlinear optical properties. For instance, the second and the third terms in Equation 1.3 represent such phenomena as Second Harmonic Generation and Third Harmonic Generation, respectively. For second order nonlinearities, a non-centrosymmetric structure is required, where $\chi^{(2)}$ is not zero. However, in the studied medium in this thesis, the centrosymmetric 4-DBpFO crystals, an SHG signal has been observed by means of THz pumping. This is so-called THz electric field induced SHG (TSHG)⁴¹⁻⁴³ and is discussed in Chapter 6.

If the THz pulse induces an electric polarization $P\left(E_{THz}\right)$ in the studied medium, it can be seen in the generation of a second harmonic response I^{2w} . For the SHG intensity in the electric dipole approximation one finds that

$$I^{2w} \propto \left|\chi^2 E^w E^w + \chi^3 E_{THz} E^w E^w
ight|^2$$

where E^w is the amplitude of the electric field of the infrared pulse, χ^2 and χ^3 are phenomenological tensors. The second term accounts for the nonlinear SHG source due to the electric polarization induced by the THz electric field $P\left(E_{THz}\right)$.

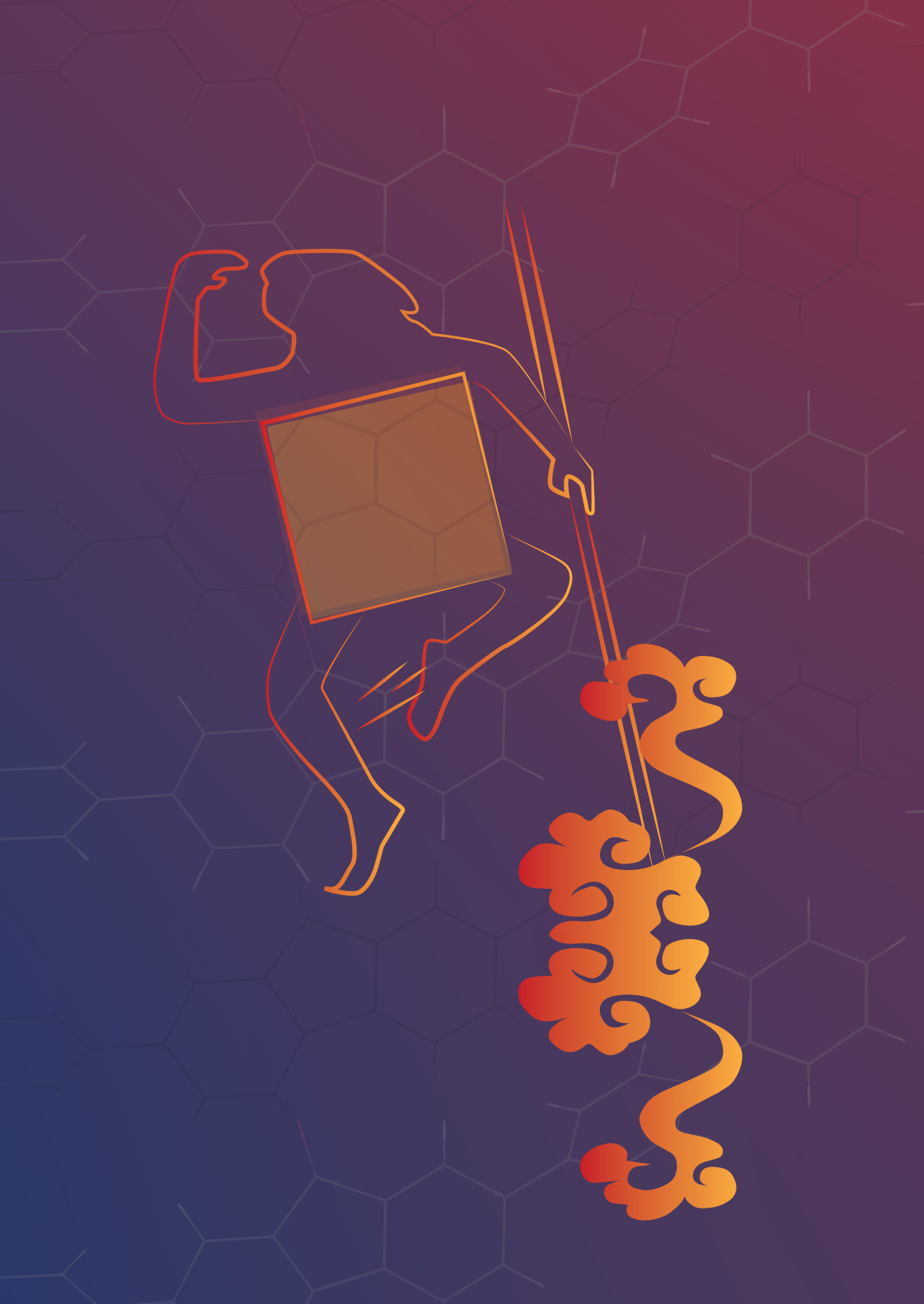
In electric dipole approximation, the SHG signal from an unperturbed centrosymmetric 4-DBpFO single crystal is zero. That is to say, the first term in the equation above is equal to zero. The external electric field of the THz pulse breaks the spatial inversion symmetry and results in a non-zero contribution $\chi^3 E_{THz} E^w E^w$ to the net SHG signal⁴¹.

Light-matter interaction can also be described in terms of polarizations induced by gradients of the electric field of light. For instance, in the case of a plane wave propagating along the x-axis and having a wave-vector k, for the electric field one can write $E\left(t\right)=E_{m}\exp\left(i(\omega t-kx)\right)$. In the case of linear optical approximation $P_j=arepsilon_0\chi_{jlp}rac{\partial E_l}{\partial x}$, which can be now rewritten as $P_j\sim kE_l$. Nonlinear optical properties in the quadrupole approximation can thus be considered accordingly.

1.3 Scope of thesis

To study the origin and dynamics of the structural phase transition in the thermosalient organic crystal 4-DBpFO, Raman spectroscopy and ultrafast pumpprobe techniques with different pump wavelengths are used.

The preparation of this crystal and the methods for characterization and optical setups that are used in this thesis are summarized and described in Chapter 2. Chapter 3 explores two different optical properties (fluorescence change and birefringence change across the phase transition) of 4-DBpFO, to define a proper probe parameter for later studies. Chapter 4 utilizes in-situ Raman spectroscopy to study the structural phase transition and reveals two important phonon modes that are closely related to and define the order parameter of the phase transition in 4-DBpFO. Chapter 5 aims to study the ultrafast dynamics of the phase transition on a picosecond timescale. The laser induced polarization rotation change indicates the possibility of an optically induced structural phase transition in 4-DBpFO. This means that the thermosalient effect can also be triggered optically and thus provides potential to control the salient behavior remotely. In Chapter 6 we demonstrate how the thermosalient structural phase transition in 4-DBpFO can be driven by strong THz pulses. Chapter 7 contains a summary and outlook of this thesis.



Chapter 2

Material characterization and experimental approaches

This chapter is an introduction to the materials studied and some experimental techniques used in this thesis. The materials are based on several polymorphs of one compound, 2,7-di([1,10-biphenyl]-4-yl)-fluorenone (4-DBpFO). In this chapter, we present the sample preparation methods, crystalline habits and structures of the two polymorphs of interest, the α and α phase of 4-DBpFO, as well as their linear optical properties. These two phases are stable at room temperature. The fluorescence microscope images show their crystal morphologies and their fluorescence colors. In this chapter, we also describe the experimental setups which are used to study the optical and dynamic properties of these materials.

2.1 Crystallization

Polymorphism and the corresponding crystal habits and symmetries rely highly on the crystal growth conditions, which provides possibilities for control. Therefore, many crystallographic growth methods have been explored to grow fluorenone-based molecular single crystals with sizes ranging from micrometer to millimetre, to satisfy various purposes. Slow evaporation from a saturated solution and slow liquid/liquid diffusion, by dropping a poor solvent solution of the compound in a good solvent to make crystals grow at the liquid/liquid interface^{34,35}, are two widely used methods to create large sized single crystals that can satisfy many applications and measurements, such as THz generation and X-ray diffraction (XRD) analysis, but these methods usually take a long time. Re-precipitation (by quick injection a solution of the compound into a poor solvent to quickly mix them) and drop-casting, by dropping a solution onto a flat surface followed by evaporation of the solution, are two popular methods that can quickly afford high-quality microcrystals for the application of nanophotonics⁴⁴.

The synthesis of the 4-DBpFO compound has been described in previous work³⁵.

Both the α and α' phase crystals were grown via a self-assembly method, in which the compound precipitates from the diffusion of a bad solvent (heptane) into a good solvent (chloroform). The good solvent indicates high solubility of 4-DBpFO compounds whereas bad solvent indicates low solubility. The best ratio of heptane and chloroform is 1:6. The saturated 4-DBpFO chloroform solution was first transferred into a clean vial, then the heptane was carefully dropped onto the surface of the solution. As the density of heptane (0.684 g/cm³) is lower than that of chloroform (1.49 g/cm³), a clear boundary will form between the saturated 4-DBpFO chloroform solution with heptane on top. These prepared vials will be put in a steady closet under ambient conditions. As chloroform has a lower boiling point (61.2 °C) than the heptane (98.42 °C), the chloroform will evaporate faster. During the evaporation of chloroform, these two solvents will mix and reduce the solubility of 4-DBpFO in the mixed solvents. Therefore, the molecules start to selfassemble itself via the Van der Waals and hydrogen forces, and form solid state crystals. Well-defined parallelogram-shaped microcrystals with side lengths varying from 50 to 100 µm are formed after 2-3 weeks. These crystals are often found on the wall and the bottom of the vials.

When preparing single crystals for measurements, one can use the bad solvents to rinse the crystals off the vials, and then drop-cast the suspension with freestanding microcrystals onto glass substrates. When the bad solvent completely evaporates,

crystals are left on the glass substrate, attached via surface tension. The single crystals can be manipulated using a needle.

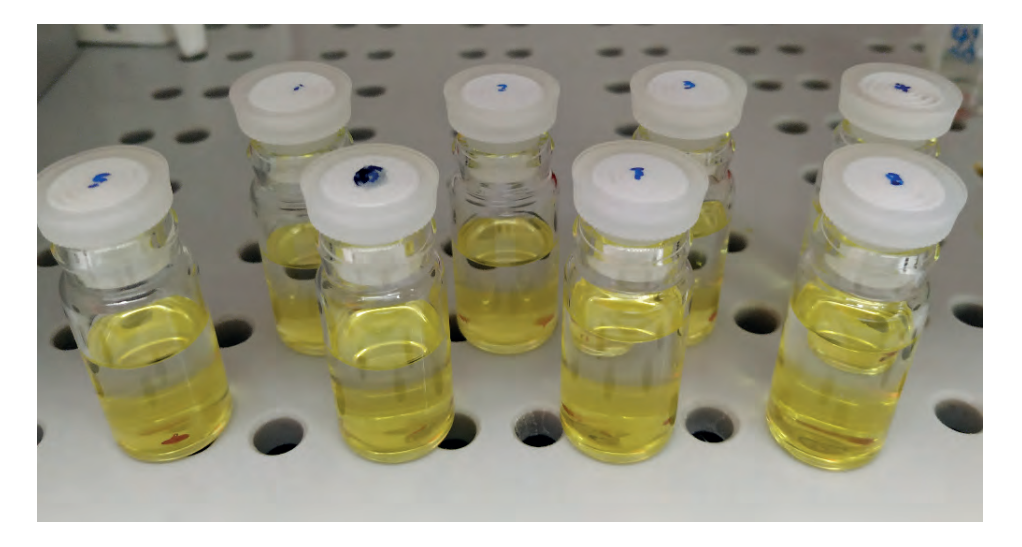


Figure 2.1. Vials for crystallization.

2.2 Crystal characterizations

In general, there are three ways to distinguish α phase 4-DBpFO crystals from the α' phase:

- 1. By examining the corner angles of a single crystal. If all of the four angles are 90 degrees (each adjacent side is normal to each other), then it is α phase. When the angles are shifted from 90 degree (thus in a rhombic shape), then it is α' phase.
- 2. By examining the color of emitted fluorescence. α phase crystals emit typically green light whereas the α ' phase emits yellow light.
- 3. By SCXRD. This is the most precise way and yet the most effort-costing way. SCXRD can give you the alignment of atoms in a crystal lattice thus determining the point group and the space group of the crystal. In this way one can easily assign the phase.

2.2.1 Fluorescence microscopy

One of the ways to distinguish the α phase crystals from the α' phase crystals is by examining the fluorescence emission. In order to distinguish the α phase crystals from the α' phase crystals, a fluorescence microscope (Leica Systems DM2500 microscope) is employed with a UV lamp source. At room temperature, these two crystals emit different colors under the fluorescence microscope: The α phase crystals emit green color fluorescence whereas the α' phase crystals emit yellow. The images acquired were also used to measure the lengths of the crystals, thanks to the calibrated scale of this microscope corresponding to each objective.

2.2.2 Hot stage microscopy

To identify the phase transition temperature of each single crystal, a hot stage measurement is necessary. In this thesis, the hot stage microscope (Zeiss Axiolpan 2) is used to identify the phase transition temperature. It is equipped with a Linkam hot stage (THMS600/HFS600 Temperature Controlled Stage, Linkam Scientific Instruments) and an Evolution VF Cooled Color camera by Media Cybernetics. The temperature range of this system is from -196°C to 600°C, which covers the transition temperatures of 4-DBpFO crystal (around 190°C). The hot stage is controlled by the Linksys32 software. It is possible to set the temperature in several cycles to let the crystal heat and cool repeatedly. In this way, the reversibility of this phase transition is tested.

2.2.3 Profilometry

The thickness of single 4-DBpFO crystal ranges from a few micrometers to tens of micrometers. It is thus difficult to measure the thickness with AFM. Instead, we used the Profilometry method to measure the thickness of crystals. In the lab of Applied Materials Science group at Radboud University, there is a Dektak 6M Surface Profiler which can measure the thickness of samples up to 25.4 mm. The Dektak 6M provides the flexibility to perform precise step height measurements for thin films down to less than 10 nm, as well as thick-film measurements up to several hundred microns thick. The conceptional scheme of the Profilometer is shown below in Figure 2.2. A typical thickness measurement result is shown in Chapter 3 Figure 3.10.

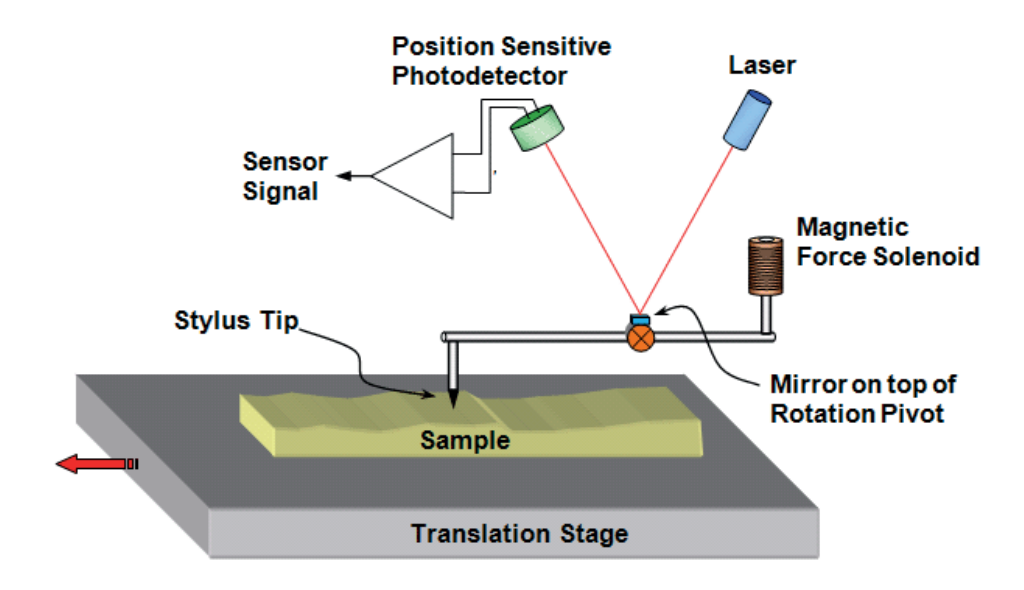


Figure 2.2. Profilometry setup from Nanoscience Instruments.

2.2.4 Single crystal X-ray diffraction

Single crystal X-ray diffraction (SXRD) measurements were collected on a Bruker D8 Ouest diffractometer with sealed tube (Mo Ka radiation) and Triumph monochromator. The software package Saint was used for the intensity integration. Absorption correction was performed with SADABS. The structures were solved with direct methods using SHELXT. Least-squares refinement was performed with SHELXL-2014 against $|F_b^o|^2$ of all reflections.

2.3 Experimental techniques and setups

2.3.1 Raman spectroscopy setup

Polarized Raman spectra were recorded with a micro-Raman Horiba LabRAM HR Evolution system in the 20-2500 cm⁻¹ spectral range at the Department of Chemistry, University of Coimbra, Portugal. Excitation was provided by a HeNe laser $(\lambda = 633 \text{ nm}, \text{ vertically polarized})$ which was focused on the sample by a microscope objective (×50 and ×100). The laser power at the sample was kept at around 1.7 mW, minimizing the local heating of the sample that may cause degradation. The collection time was set to 10 s with 10-30 accumulations averaged to produce the final spectra. In order to collect the polarized spectra, a half-wave polarization rotator (Horiba-Jobin-Yvon) was used to change the polarization of the incident light by 90° and a CorePol P-500-1000 polarizer (Horiba-Jobin-Yvon) was used to select the component of the scattered light to collect. The signal was dispersed using an 1800 g· mm⁻¹ grating with a spectral resolution of 0.4 cm⁻¹. The wavenumber calibration was performed using the characteristic Si wafer band at 520.5 cm⁻¹.⁴⁵

To perform temperature-dependent Raman measurements, a temperaturecontrolled heating stage THMS600 (Linkam Scientific) was used with an accuracy of 0.1°C.

The vertical (denoted as V) input polarization was parallel to the crystallographic a-axis, while the horizontal (denoted as H) input polarization was parallel to the crystallographic c-axis (see Figure 2.3). The input polarization is by default Vertically polarized, and can be tuned into Horizontal polarization by applying a half-wave plate as shown in Figure 2.3. An analyser was installed in front of the detector so that only certain polarization (V or H) scattered light is allowed to go into the detector.

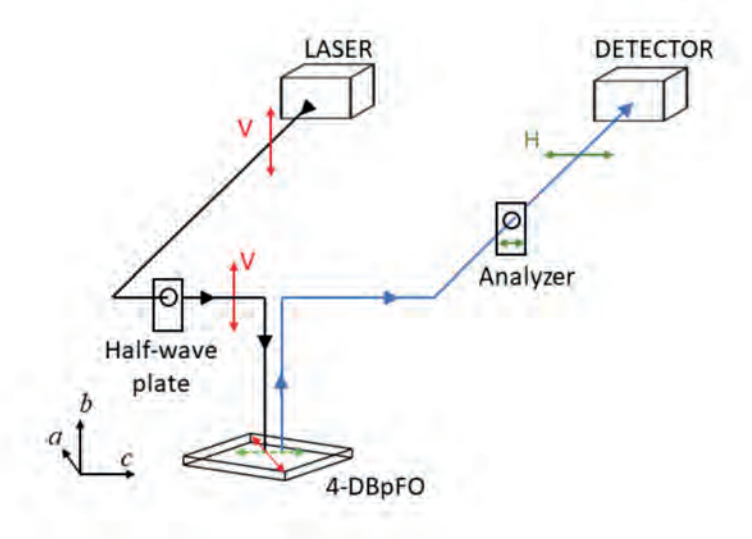


Figure 2.3. Schematic set up of the Raman experiment.

The black and blue traces correspond to the incident and scattered beams, respectively. The double arrows represent the direction of the polarization of the beam, classified as horizontal (H) and vertical (V) in the reference frame of the laboratory. The depicted Cartesian vectors, a, b, and c, refer to the crystallographic axes. (adapted from 45)

2.3.2 Birefringence setup

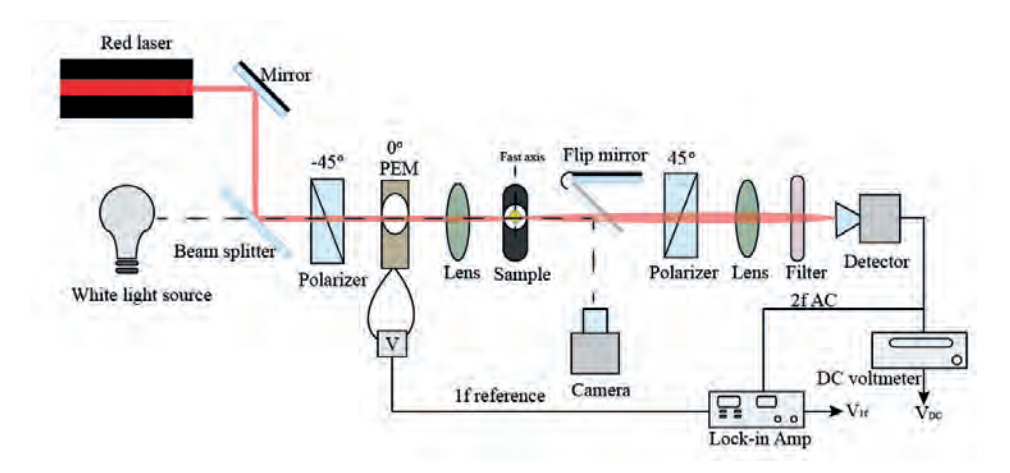


Figure 2.4. Home-built setup to measure the wave retardation of the 4-DBpFO crystal.

The red laser source was a cw HeNe laser centered at 632.8 nm. Two polarizers are set before and after the sample with crossed polarizations (-45° and 45°). A photoelastic modulator (PEM) is employed to modulate the phase of the propagating beam with setting as $\lambda/2$ (functioning as a half-wave plate). The polarization rotation of the output beam is registered on a photo-diode detector and converted into retardation value via the Lock-in amplifier. A white light source was employed to visualize the sample and the position of the sample was corrected by moving a X-Y translational stage during heating and cooling. The temperature on the sample was controlled by the LakeShore 340 Temperature Controller with a home-built heating head.

The PEM retardation was set to 2.405 radians. With this setting the DC voltage is constant and does not depend on the orientation of the analyzer, and sample. With a lock-in amplifier the retardation (birefringence of the sample) can be measured. With $A_0 = 2.405$, $J_0(A_0)$ becomes 0 and the magnitude of the retardation can be determined by the following formula:

$$\delta = \sin^{-1}\Big(rac{1}{\sqrt{2}J_1(2.405 ext{rad})}rac{V_{1f}}{V_{ ext{DC}}}\Big).$$

 $J_1\left(2.405\right) = 0.52, \, V_{1f}$ is the lock-in voltage at the frequency of the PEM and $V_{\rm DC}$ is the DC voltage. To measure the retardation magnitude, rotate the sample so that the V_{1f} is maximum which indicates that the fast axis of the sample is parallel to the PEM optical axis.

Another method to determine the retardation magnitude is when the sample is fixed. Then with the analyzer at -45 degrees, the calculated retardation is δ_1 . Then rotate the analyzer to 0 degrees and call this retardation δ_2 . Then the magnitude of the retardation can be calculated as $\delta = \sqrt{\delta_1^2 + \delta_2^2}$ and the angle of the fast axis of the sample can be calculated from: $\theta = \frac{1}{2} \tan^{-1} \left(\frac{\delta_2}{\delta_1} \right)$.

Jones Matrices calculation for the retardation measurements above:

Simplifying the calculations we will start with a linear input polarization which is polarized at a 45 degree angle:

$$P_{\mathrm{in}} = rac{1}{\sqrt{2}} \left[egin{array}{c} 1 \ 1 \end{array}
ight].$$

The polarization of the light after passing through the PEM (where the optical axis of the PEM is along the x-axis of the lab frame) can be described by the following Jones matrix

$$\mathrm{M}_{\mathrm{PEM}} = \left[egin{array}{cc} 1 & 0 \ 0 & M \end{array}
ight],$$

where $M=e^{i A \sin(2\pi f t)}$, and A is the amplitude of the modulation. The amplitude depends on the thickness of the optical element inside the PEM and the difference in the refractive index along the fast and slow axis. This shows that by changing the amplitude A to the right settings, the PEM can act as a $\lambda/2$ or $\lambda/4$ wave-plate. The operating frequency of the PEM used in this thesis is 50 kHz.

After the PEM, the light passes through the sample. Since we would like to know the optical properties of the sample we will take the Jones matrix for an arbitrary birefringence material:

$$\mathrm{M_s} = e^{-rac{\mathrm{i}\eta}{2}} \left[egin{array}{cc} \cos^2\! heta + e^{\mathrm{i}\eta} \mathrm{sin}^2 heta & \left(1-e^{\mathrm{i}\eta}
ight) e^{-\mathrm{i}\phi} \mathrm{cos} heta \mathrm{sin} heta \ \left(1-e^{\mathrm{i}\eta}
ight) e^{\mathrm{i}\phi} \mathrm{cos} heta \mathrm{sin} heta & \mathrm{sin}^2 heta + e^{\mathrm{i}\eta} \mathrm{cos}^2 heta \end{array}
ight]$$

Here $\eta=\phi_x-\phi_y$ is the phase difference between by the fast and slow axis and hetais the angle between the fast axis and the x-axis (horizontal) within the lab frame.

Then when the light passes through the second polarizer, positioned a -45 degree, the Jones matrix is defined as:

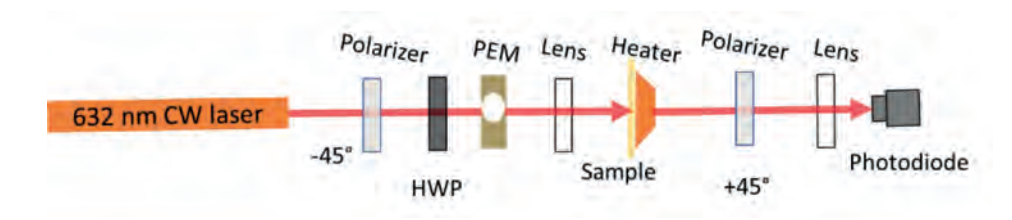
$$\mathrm{M_{pol}} = rac{1}{2} \left[egin{array}{cc} 1 & -1 \ -1 & 1 \end{array}
ight]$$

The output polarization is then defined as follows:

$$P_{\text{out}} = M_{\text{pol}} M_s M_{\text{PEM}} P_{\text{in}}$$

In the case of a birefringence measurement, the orientation of the fast and slow axis of the sample must be known first. This can be determined by rotating the sample to find the maximum signal. For the purpose of this paragraph we assume the orientation of the birefringence of the sample to be known and this will be set to be $\theta = 0$. The output polarization is then simplified to:

$$\mathrm{P_{out}} = rac{1}{2\sqrt{2}} \left[egin{array}{c} 1 - e^{i(2\pi \mathrm{ft} + \eta)} \ -1 + e^{i(2\pi \mathrm{ft} + \eta)} \end{array}
ight]$$



The output polarization is then defined as follows:

$$\mathbf{P}_{\mathrm{out}} = \boldsymbol{M}_{\mathrm{pol}} \boldsymbol{M}_{s} \boldsymbol{M}_{\mathrm{pol}} \boldsymbol{P}_{\mathrm{in}}$$

The input polarization at a 45 degree angle: $P_{in}=rac{1}{\sqrt{2}}\left[egin{array}{c}1\\1\end{array}
ight]$.

Then when the light passes through the second polarizer, positioned a -45 degree, the Jones matrix is defined as:

$$\mathrm{M_{pol}} = rac{1}{2} \left[egin{array}{cc} 1 & -1 \ -1 & 1 \end{array}
ight]$$

2.3.3 Absorbance setup

When continuous radiation passes through a transparent material, a portion of the radiation may be absorbed. If that occurs, the residual radiation, when it is passed through a prism, yields a spectrum with gaps in it, called an absorption spectrum 46.

In practice, the spectrum is often recorded in the ultraviolet-visible range (UV-vis) as a plot of absorbance versus wavelength⁴⁶. Since the present work focuses on spectra expressed explicitly in terms of absorbance, we will use the term absorbance spectrum throughout this thesis.

The absorbance spectrum of 4-DBpFO in solution has been obtained and presented in Figure 3.3a). The solution-phase spectrum can serve as a reference for comparison with the solid-state spectrum. In the condensed phase, the absorption bands of the same compound can exhibit peak shifts due to restricted molecular rotations and vibrations⁴⁷. To investigate the most prominent absorption features of 4-DBpFO single crystals in the visible spectral range, a home-built setup was employed, as illustrated in Figure 2.5. The resulting absorbance spectrum is presented in Figure 5.1.

During the experiment, the micro-sized 4-DBpFO single crystal (depicted as transparent square-shaped plates with yellow color in Figure 2.5) was placed on a glass substrate. When light passes through the sample, attenuation occurs primarily due to the absorption in the crystal. However, additional losses from reflection, scattering, or absorption in the glass substrate may also affect the results. To compensate for these effects, the transmitted power through the sample and substrate (p) was compared with the transmitted power through the identical substrate alone (p_0) . The experimental transmittance is thus defined as:

$$T = \frac{p}{p_0}$$

The absorbance can then be calculated according to Beer-Lambert's law:

$$A = -{
m log}T = -{
m log}rac{p}{p_0}$$

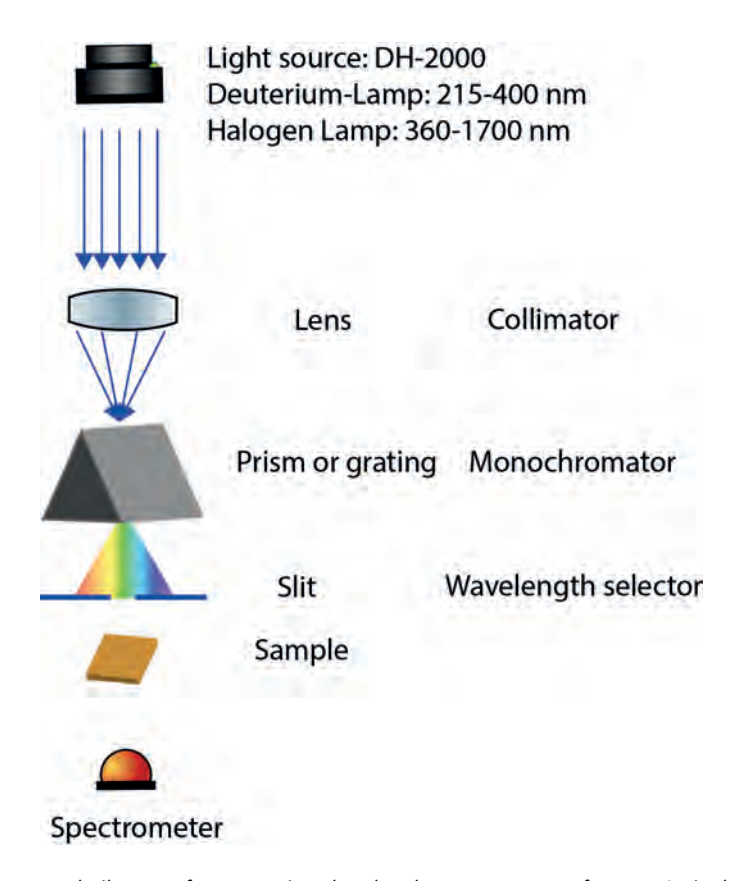


Figure 2.5. Home-built setup for measuring the absorbance spectrum of 4-DBpFO single crystals at room temperature.

The accessible spectral range is determined by the selected light source of the DH-2000 lamp: the deuterium lamp covers 215-400 nm, while the halogen lamp covers 360-1700 nm. For the spectrum shown in Figure 5.1, the halogen lamp was used, providing coverage from 360 to 1050 nm. The focusing lens allows adjustment of the beam spot size, enabling measurements on crystals of different sizes.

2.3.4 FLARE setup

The FLARE beam is generated by a free electron laser in the institute of HFML-FELIX, Radboud University. FLARE operates in the range from 20-1500 microns in 3 GHz and 20 MHz mode. The beam contains macro pulses (5 Hz) that each consists of micro pulses (at 3 GHz or 20 MHz). The pulse width of the macro pulses is approximately 10µs while the pulse width of the micro pulses is estimated to be ~10 ps for the 3 GHz mode. In our experiment, we first started with the 20 MHz mode but failed to see anything. The results presented in Chapter 6 are obtained with the 3 GHz mode.

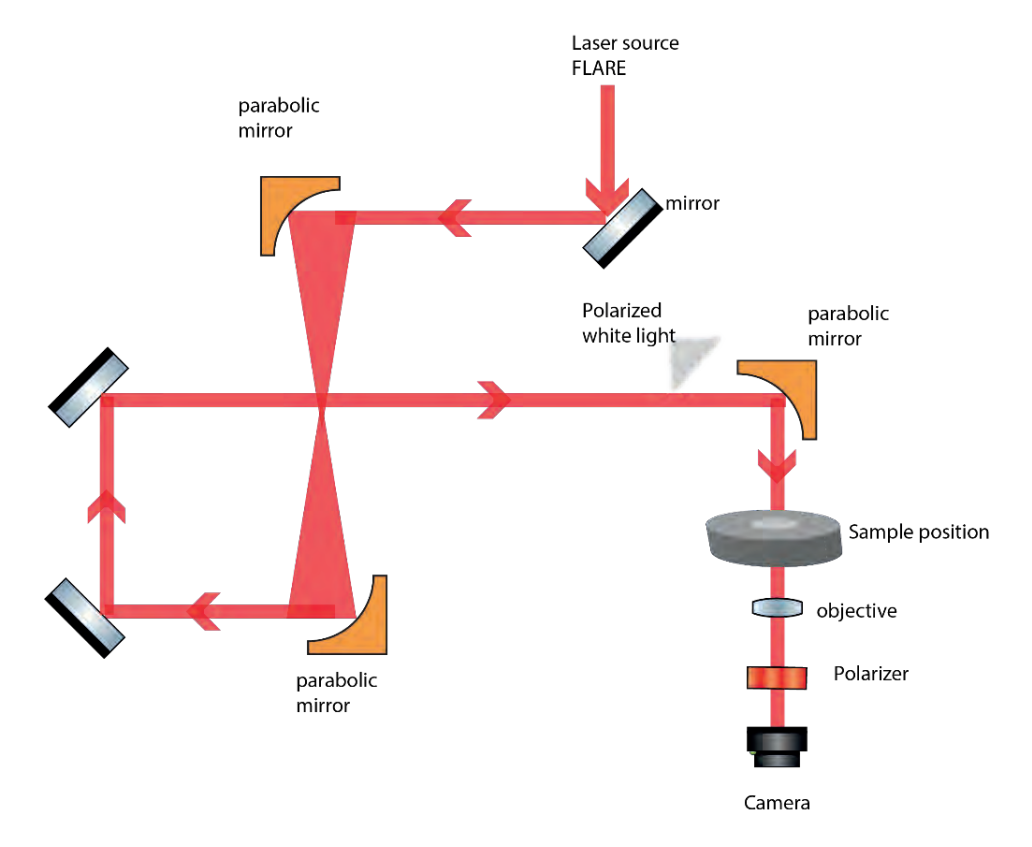


Figure 2.6. Home-built microscope setup to visualize the THz induced phase transition in 4-DBpFO crystals.

FLARE: 5Hz macro pulses composed out of 3GHz micro pulses; 46-47 cm⁻¹; highest pump power reached 95±2.5 mW. The direct output of FLARE beam is vertically polarized. An analyser is set in horizontal polarization in front of the camera to detect the birefringence.

2.4 Pump-probe techniques

2.4.1 Optical pump-probe

In 1967, Armstrong and Shelton first demonstrated the utility of a pump and probe technique using picosecond optical pulses. A train of intense picosecond pulses was used to saturate the absorption of a Q-switching dye. An attenuated image of the saturating pulse train was used to monitor the absorption recovery as a function of relative time delay between the pumping and probing trains of pulses. Since the time of that experiment a number of techniques have been developed to excite, probe, delay, gate and synchronize picosecond pulses.

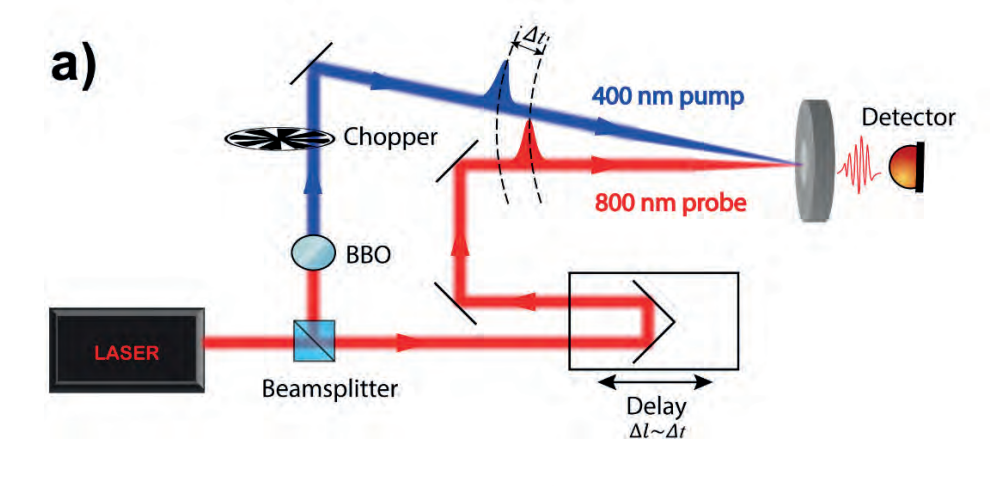
Typically, two laser pulses are needed for performing time-resolved experiments. One strong pulse serves as pump to trigger the excited state of a sample, and the other pulse, generally 10 times weaker in power/fluence, comes in as a probe to register the optical property change, after a specific delay time, in the pumped sample. Based on the geometry, this type of experiment can be divided into reflection geometry and transmission geometry. In the transmission geometry one can measure the transmission change or polarization rotation change, while in the reflection geometry, the reflectivity and phonon oscillations are normally the interest.

The time delay between pump and probe is defined by two factors: repetition rate of the ultrafast laser pulses and the precision of a mechanical delay stage. The mechanical precision of the delay stage defines the time resolution that we can achieve in pump-probe experiments, as the time resolution Ts = D/c, where D is the smallest unit of the delay stage and the c is light speed. The smallest unit of our delay stage is 0.05 mm, which is corresponding to a time resolution of 50 fs. The repetition rate of the laser source is 1 KHz, which means that there is one pulse output per millisecond with a pulse length of 80 fs. The pulse length and the time resolution together determine the fastest dynamics we can detect on the setup.

2.4.2 Home-built pump-probe setup

The ultrafast pump-probe experiments in transmission geometry were performed with a Ti: sapphire amplified laser (Spitfire Ace) of 800-nm pulses for a duration of 80 fs at a 1 kHz repetition frequency. The pump was impinging at an angle of 20° to spatially separate from the normal incident probe beam. The pump and probe spot sizes were determined by knife-edge measurement (an example see Figure 2.8). The pump and probe pulses were set to be cross polarized and the transmitted signal is sent to a home-made balanced detector⁴⁸.

Regeneratively amplified pulses from a Ti: sapphire laser at a wavelength of $\lambda = 800$ nm and a repetition rate of 1 kHz are used in this study. Each pulse had a Gaussian intensity profile, with a full width at half maximum of 80 fs. The probe laser pulses were incident normal to the sample surface, so that the correspondence of the orientation of crystallographic axes and the polarization of the probe beam can be easily resolved. The beam was focused down to a 40 µm spot and the laser-induced transmission changes are studied at various temperatures. The sample was put on a glass substrate and exposed to air.



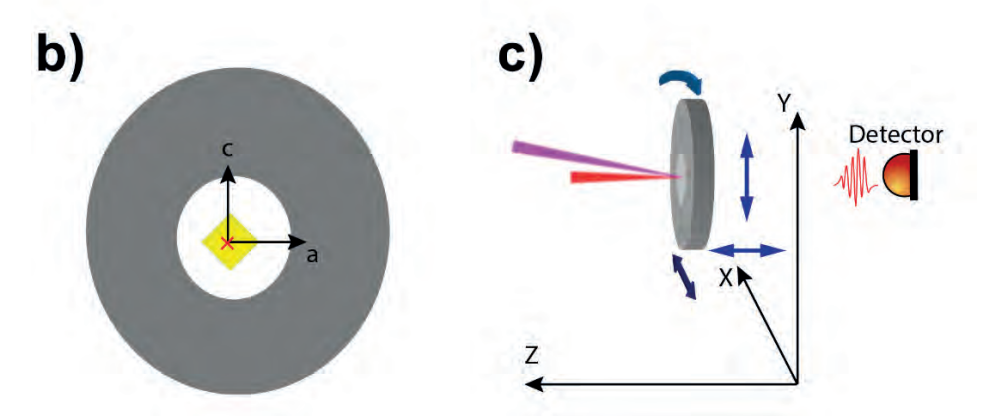


Figure 2.7. Home-built optical pump-probe setup and the crystallographic geometry on the sample holder.

a) A laser beam was split into two beams by a polarized beam splitter, where a beam with strong power serves as pump beam and the beam with a relatively weak power serves as a probe beam. The setup is built in a geometry where both transmission and reflection experiments can be done. The transmitted/reflected photons fall on a photodiode/home-built balanced detector. The wavelengths of both pump and probe are interchangeable by using a nonlinear crystal BBO. The time-resolved measurements can achieve a resolution as small as ~100 femtoseconds, depending on the output pulse width from the laser. The stable output wavelength is centered at 800 nm. b) The orientation of crystallographic axes of 4-DBpFO single crystal on the sample holder. The crystallographic b-axis is along the incident pump beam direction, perpendicular to ac plane. c) The relative orientations of the optical setup and the sample holder. X direction is parallel to the optical table and the Y direction is perpendicular to the optical table. Z direction is parallel to the pump beam direction (perpendicular to the sample holder). The sample holder is adjustable in all X, Y, and Z directions. Besides, it is also rotatable up to 360°, giving enough space for placing the micro-sized crystal properly on the setup. The sample holder is also connected with a home-built heating head so that a temperature-dependent measurement can be achieved with it.

2.4.3 Knife-edge method

Considering the laser pulse as a Gaussian shape beam, to measure the beam waist of the pulse, one can use the knife-edge method.

The beam is focused by a lens and the beam waist is the diameter of the Gaussian beam at the focal point. At a distance of z from the position of the focal point, the beam is progressively covered by a knife edge (a blade) and the transmitted power is registered as $P^{49,50}$. P is at its maximum (P_{max}) when the beam is not covered by the blade and its minimum (P₀) is reached when the beam is completely covered by the blade. All the visited scanning position of the blade is registered as x in mm. One curve of P as a function of x can be obtained and can be fitted by an error function stated in equation 2.1 (see Figure 2.8a).

$$P = P_o + rac{P_{
m max}}{2} * \left(1 - {
m erf}\left(\sqrt{2} * rac{x-x_0}{r}
ight)
ight) \qquad \qquad (2.1)$$

where P is the transmitted power in the unit of watt, P_0 is the background power, P_{max} is the maximal power, erf is a standard error function, x is the position of knife edge.

After fitting, one can obtain a central position x_0 of the blade where the beam radius r sits. Note that beam waist (diameter, 2r) is twice of the beam radius.

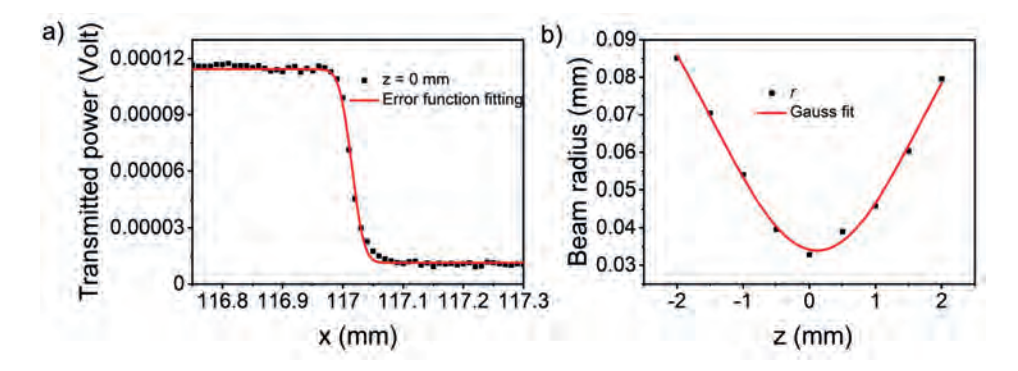


Figure 2.8. a) A typical curve obtained during the measurement by the knife-edge method. The red line is the fitting by an error function stated in equation 2.1. b) The Gauss fit of beam radius obtained by error function fitting in a).

Repeat this for several z positions around the focal point, and register the z values in order to find the precise focal point. Plotting the calculated r as a function of z, one can define the precise focal point using a Gauss fitting (see Figure 2.8b). Figure 2.8 shows a typical knife-edge result measuring the beam radius of a probe beam. The results show that the focal point is at z=0 mm where the beam waist reaches its minimum of 65 um. The area where the laser pulse was focused can be calculated as πr^2 . From here on, one can calculate the fluence when the laser power and pumping area are known (see section 2.4.4 for fluence calculation).

2.4.4 Fluence calculation

Based on the intensity profile of the laser spot, the fluence can be calculated in different ways. In the first method we assume the laser spot has a flat-top profile, which means that the energy is distributed homogeneously over the area A. Then the fluence is calculated using the formula:

$$f = rac{P}{\pi * r^2}$$

In the other method, the laser spot is assumed to have a gaussian profile. In this case, the energy is not distributed evenly over the area and it is therefore not possible to get a single fluence value representing the whole beam spot area. Above certain pump power, the sample will be burned immediately upon pumping. Therefore, valid optical measurements should stay below the laser damage threshold (LDT) of the sample system. The LDT is defined by the peak fluence. To calculate the peak fluence we use the formula:

$$f=rac{P}{\pi*rac{r^2}{2}}$$

where P is the power and r is the radius of the pump beam.

2.4.5 THz pump-optical probe

The terahertz frequency range falls in between the infrared and microwave region of the electromagnetic spectrum (0.1 THz to 10 THz) and it shares some properties with each of these³². Many common materials and living tissues are semitransparent for THz radiation and have "THz fingerprints", allowing the ease of imaging, identification, and analysis. Nowadays, there are several ways to generate single or few cycle THz pulses using femtosecond lasers: photoconductive switches 51 , the photo-Dember effect 52,53 and NLO rectification in inorganic and organic crystals⁵⁴⁻⁵⁶. Here we want to emphasize the technique of THz generation using optical rectification in molecular crystals that offer relatively simple ways to

obtain THz table top systems. Optical rectification is the result of the second order NLO process of difference frequency generation in which two incoming photons of the same frequency lead to a "zero" frequency response ($\omega_2 = \omega_1 - \omega_1 = 0$). Due to the finite bandwidth of fs laser pulses (a 100 fs pulse at 800 nm corresponds to a width of 4.5 THz), a THz response is generated in the material⁵⁷. There is an astonishing amount of organic materials which can be used for THz generation. The list of widely used compounds includes DAST^{55,58}, DSTMS⁵⁴, OH1⁵⁴ and HMQ-TMS^{59,60}. As each of these materials only cover a part of the THz spectrum of interest, there is an ongoing search for new materials that can efficiently convert higher frequency light into the THz-frequency range.

High-power THz radiation is needed to drive the structural phase transition in thermosalient organic crystal 4-DBpFO⁶¹. While several MV/cm of peak THz field intensity can be achieved by using organic nonlinear optical crystals^{55,58,62}, here we employed tilted-pulse-front optical rectification in LiNbO₃ to generate intense nearly single-cycle THz pulses⁶³ to achieve peak intensities of 1 MV/cm.

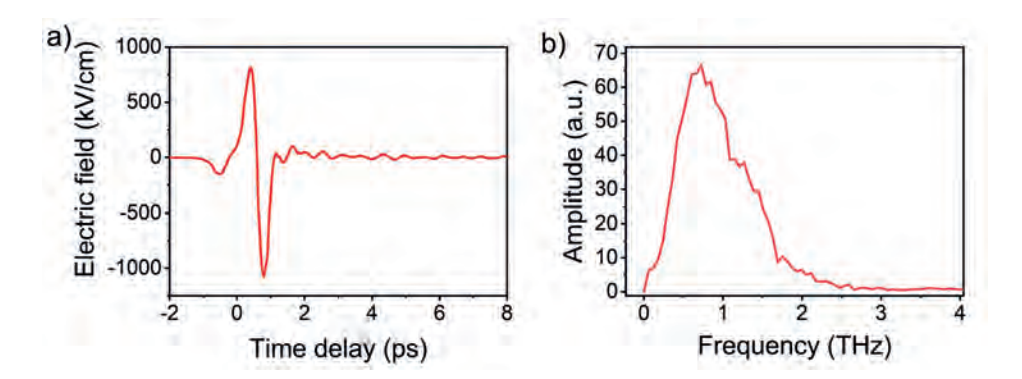


Figure 2.9. a) THz pulse waveform; b) Corresponding Fourier spectrum.

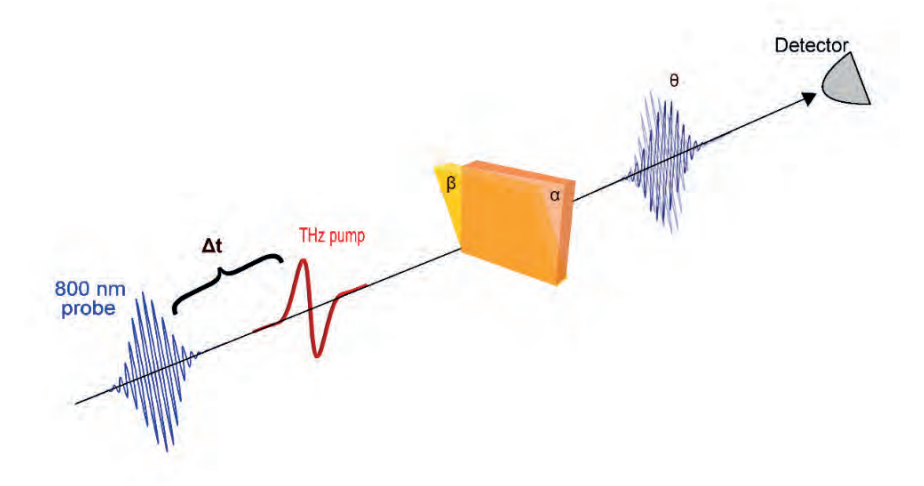


Figure 2.10. Conceptual scheme of THz pump-optical probe setup.

To generate the strong THz pulse, an amplified Ti:saphire laser system was employed with a central wavelength of 800 nm and a pulse duration of 100 fs, operating at a repetition rate of 1 kHz. The tilted pulse front for the THz generation was created using a diffraction grating. The peak amplitude of the THz electric field was around 1 MV/cm (Figure 2.9a). The THz spectrum of the pulse was peaked at around 0.8 THz with the FWHM of 1.0 THz (Figure 2.9b), covering the low frequency spectrum (1.0 - 1.6 THz) that is of interest in this project. Using a set of parabolic mirrors, the generated THz beam was expanded, collimated and focused onto the sample with a spot size of $\sim 300 \mu m$. The probe pulse is directed through a small hole in the parabolic mirror onto the sample and the THz induced rotation change θ of the 800 nm probe beam is detected with a balanced detector (Figure 2.10). This setup can also be used to detect THz induced SHG by introducing a color filter to block 800 nm and only transmit 400 nm. Although the thermosalient α phase 4-DBpFO features a centrosymmetric structure, non-zero SHG signal can still be detected by breaking the spatial inversion symmetry with external electric field of the THz pulse. This is so-called THz electric field induced Second Harmonic Generation (TSHG)⁴¹⁻⁴³. In Chapter 6, it shows that TSHG can also be an effective parameter for characterizing the structural phase transition in α phase 4-DBpFO crystals.



Chapter 3

Temperature dependent optical birefringence and fluorescence of two polymorphs of 4-DBpFO

In this Chapter, the temperature-dependent optical birefringence and fluorescence are measured in two orthorhombic phases of the molecular crystal 4-DBpFO. Though both structures show a similar lattice thermal expansion, their temperature-dependent birefringence value changes are very distinct. The polar structure (a'-phase) with parallel in-plane dipoles demonstrates a nonlinear birefringence value rapidly decreasing with temperature. On the other hand, the non-polar thermosalient structure (α -phase) with anti-parallel in-plane dipoles shows a quite stable birefringence value in static measurements. A clear birefringence change is observed in a dynamic pump-probe measurement in the vicinity of the phase transition temperature where the lattice undergoes a large and sudden anisotropic in-plane expansion. The results show structure related temperature-dependent birefringence changes for both crystals. Moreover, the birefringence change is proven to be a reliable probe parameter for characterizing the structural phase transition in α phase 4-DBpFO crystals. The fluorescence shows a typical temperature dependence with no clear relation to the structural change during the phase transition in α phase 4-DBpFO crystals.

3.1 Introduction

Birefringence, arising from the difference in value of the refractive index along two directions of an optically anisotropic material, is a very common phenomenon in non-cubic crystalline structures⁶⁴. As birefringent crystals play an important role in many optical elements such as optical filters⁶⁵, wave plates⁶⁶, polarizers^{64,67}, and various nonlinear optical components⁶⁸, a lot of research has been devoted on developing anisotropic crystals with large birefringence values, through a combination of both molecular packing and molecular polarizability 67,69-78. Nevertheless, the temperature dependence of the birefringence, which is very important for many optical applications, has been rarely considered. Anisotropic crystals having thermal sensitive or insensitive birefringence values are both valuable for many optical applications. For example, anisotropic crystals with thermal stable birefringence are required in designing optical elements applied in extreme environments with large temperature variations⁷⁹. On the other hand, temperature sensitive birefringent crystals can also find applications such as a temperature tunable retardation wave plates^{80,81}. In such non-centrosymmetric crystals, phase matching for optical second harmonic generation can also be easily achieved through temperature tuning⁸².

Due to thermal induced lattice expansion and molecular vibrations/rotations which can modify the anisotropy of the crystal permittivity, temperature variations can thus affect the birefringence of anisotropic crystals 83,84 . An extreme situation occurs at the point of a structural phase transition, where the molecular packing undergoes an abrupt change, and thus may result in a sudden change in optical anisotropy 85,86 . Here, we studied the temperature-dependent birefringence in two layered-polymorphs of the compound 4-DBpFO 22,87 . Although the two structures are possessing similar crystal habits, both having an orthorhombic crystal symmetry, their temperature-dependent birefringence is quite different: one structure (α -phase) shows quite stable birefringence up to its thermosalient phase transition, where it changes suddenly, while the other (α '-phase) demonstrates a deceasing birefringence with temperature. Our results show that the molecular packing plays a crucial role in affecting the temperature-dependent birefringence in the studied organic molecular crystals.

3.2 Crystalline structure of α and α phase 4-DBpFO

Molecular 4-DBpFO contains a fluorenone center with two phenyl rings at each end, which can rotate freely around their linked single bounds. Due to the molecular

symmetry, the permanent dipole of a mirror symmetric molecule is always parallel to the carbonyl group and toward the oxygen atom⁸⁷, independent of the magnitude of the dihedral angles between different planes. Because of this flexible molecular configuration, the compound can exist in several crystalline forms in the solid state. The studied crystalline structures are the α -phase (Figure 3.1) and the α '-phase (Figure 3.2) of molecular 4-DBpFO with space groups *Pnma* and *Cmc2*₁, respectively. Both structures are orthorhombic, showing similar thin plate-like morphologies at room temperature. When white light passes through such micronsized thin crystals that are positioned between two crossed polarizers of a polarization microscope, most of them demonstrate a monochrome birefringent color (Figure 3.1a and 3.2a). The monochromaticity of the birefringent color indicates a uniform thickness of these crystals, which facilitate the in-plane birefringent measurement and application. Moreover, although the molecule has a weak visible absorption between 400 and 500 nm, visible light vertically passing through a plate-shaped crystal is hardly absorbed in both phases (Figure 3.3). This is due to the fact that the molecular transition dipole, which is parallel to the molecular long axis, is oriented perpendicularly to the surface plane of the plate crystals in both phases⁸⁷. Therefore, absorption in the visible light range will hardly affect their birefringence measurements. Even though both shapes of the as-grown crystals are rhombus, the α - and α -phase can be easily distinguished from the slight difference in their corner angles. The in-plane cell lengths of the α -phase are 6.8552(6) Å (crystallographic-a axis) and 6.9557(6) Å (crystallographic-c axis) while they are 6.629(2) Å (crystallographic-b axis) and 7.2402(3) Å (crystallographic-c axis) in the α '-phase, which makes the corner angles of the rhombic-shaped crystals of the α -phase to be 90.8° and 89.2° while they are 95.0° and 85.0° in the α '-phase, respectively. Molecules in both structures are layered packed along the normal direction (crystallographic b- and a-axis in the α - and α '-phase, respectively) of the thin plate-shaped crystals. Therefore, all the molecular permanent dipoles are oriented in-plane, parallel to the layer planes, and the intermolecular forces between adjacent layers mainly arises from dipole-dipole interactions. However, there is a main difference between the two phases: the molecular permanent dipoles in adjacent layers orient in opposite directions in the α -phase (Figure 3.1b and 3.1c) while they point toward the same direction in the α '-phase (Figure 3.2b) and 3.2c). This difference in dipole orientations endows the α -phase with a nonpolar structure and the α '-phase with a polar structure, respectively.

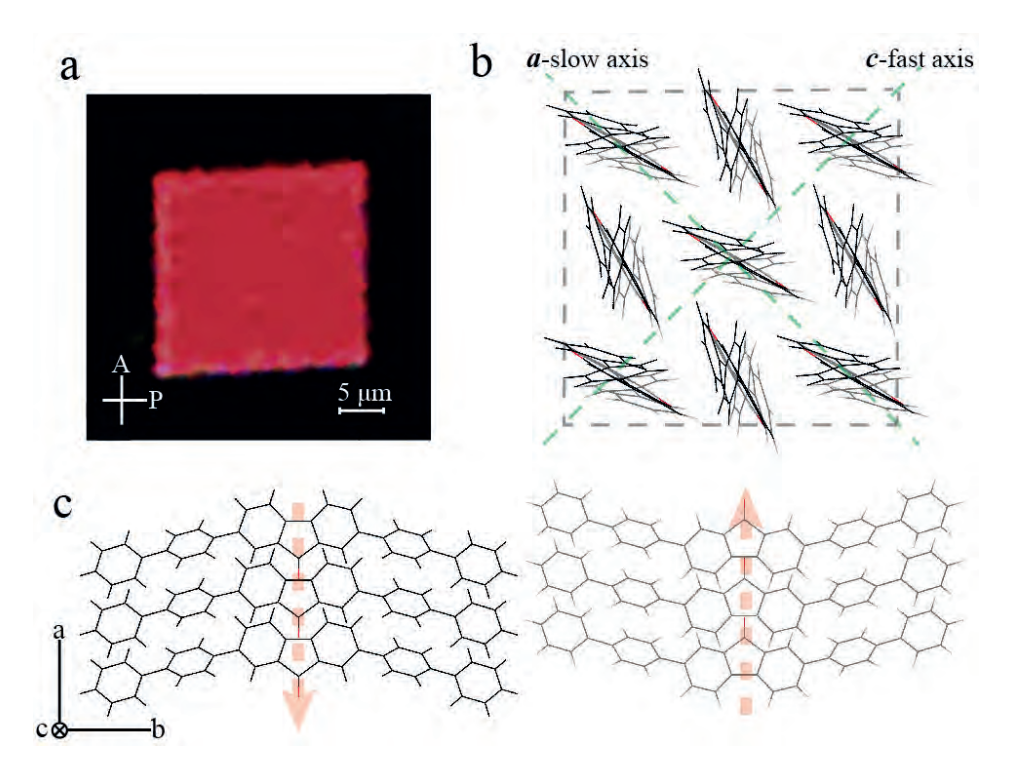


Figure 3.1. Crystal structure and morphology of the α -phase.

a) Birefringence microscope image of an as-grown crystal. The inset shows the direction of the polarizer (P) and analyzer (A); b) In-plane ((101) plane) molecular packing. The grey dotted frame outlines the crystal shape. The green dotted line shows the direction of the fast and slow optical axes which are parallel to the crystallographic-c and -a axes, respectively; c) Molecular packing along the normal direction of the crystal. The arrows demonstrate the antiparallel permanent dipoles in neighboring layers.

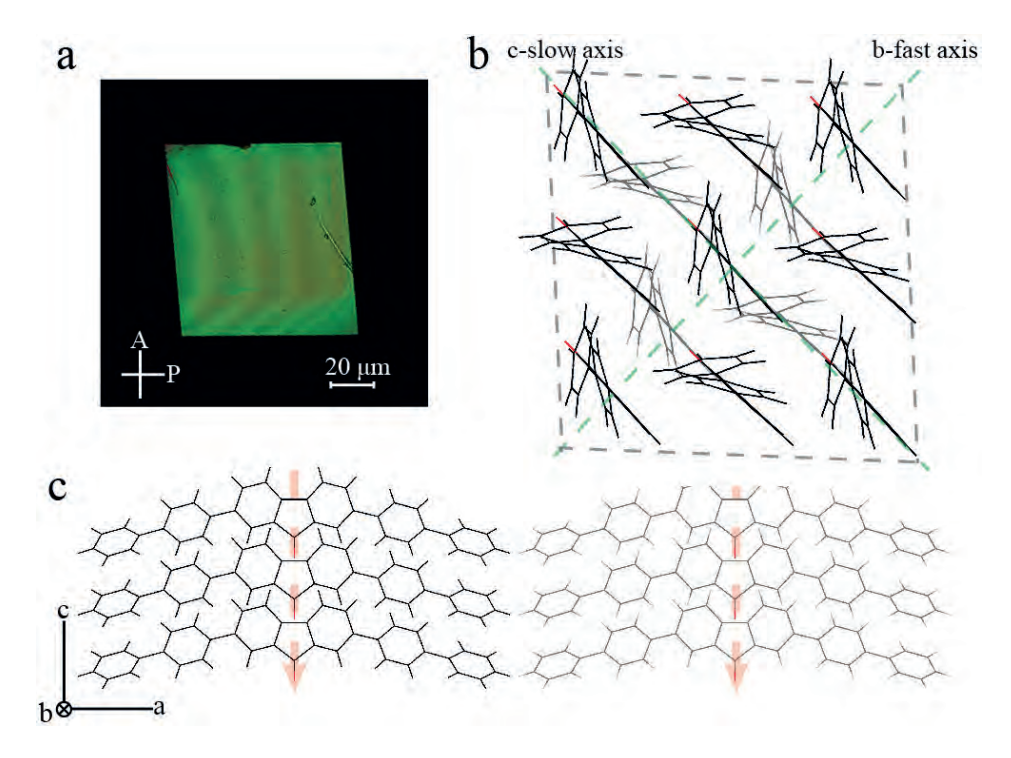


Figure 3.2. Crystal structure and morphology of the α '-phase.

a) Birefringence microscope image of an as-grown crystal. The inset shows the direction of the polarizer (P) and analyzer (A). b) In-plane ((011) plane) molecular packing. The grey dotted frame outlines the crystal shape. The green dotted line shows the direction of the fast and slow optical axes which are parallel to the crystallographic-c and -a axes, respectively; c) Molecular packing along the normal direction of the crystal. The arrows demonstrate the parallel permanent dipoles in two neighboring layers.

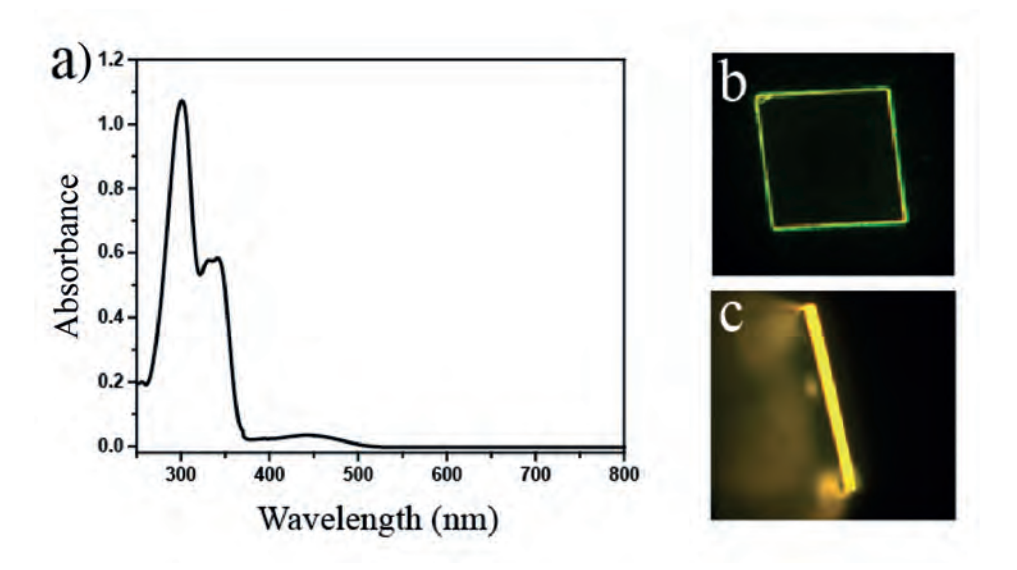


Figure 3.3. a) Optical absorbance of 4-DBpFO in chloroform solution (1× 10^{-4} M); b) and c), Fluorescent microscope images of the α phase 4-DBpFO crystal 'lying' (a) and 'standing' (b) on the substrate. Because the molecular transition dipoles are all perpendicular to the crystal top plane, transition dipoles can hardly be excited when the crystals are 'lying' on the substrate.

3.3 Anisotropic optical transmission in α phase 4-DBpFO

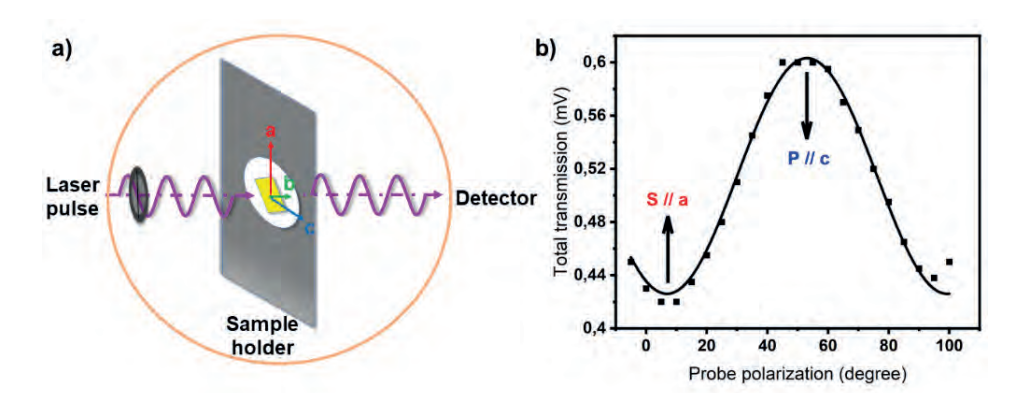


Figure 3.4. Anisotropic transmission at 800 nm obtained from a phase 4-DBpFO single crystal. a) A sketch of transmission geometry setup where the probe beam is transmitted perpendicularly through the crystal and falls on the photodiode detector. The polarization of the probe beam was tuned by rotating a half-wave plate. b) Measured transmission (dots) fitted with a sine wave function (solid line) with a period of 46.2 ± 0.8 degree. The transmission is largest when the polarization of the probe is *P-polarized*, being parallel to the crystallographic c-axis, whereas the signal is lowest when the beam is parallel to a-axis.

The S-polarized incident beam is parallel to the crystallographic c-axis and the Ppolarized incident beam is parallel to the crystallographic a-axis. We are measuring in the transmission geometry as indicated in Figure 3.4 a). With a home-made balanced-detector we are able to acquire both the transmission and polarization rotation changes in this geometry.

As can be seen in Figure 3.4, the optical transmission of α phase 4-DBpFO is strongly anisotropic at room temperature. This anisotropy experiment is done in a transmission geometry where the probe beam was led onto the sample and transmitted through it. The transmission is fitted with a sine wave function and the maximum turns out to be at P-polarization, which is parallel to the crystallographic c-axis (fast axis of the crystal).

3.4 Fluorescence emission of α phase 4-DBpFO

For organic crystals, the fluorescence (FL) emission is often related to the crystalline structure⁸⁸. A structural change of the crystal lattice thus often leads to a color change of the fluorescence, thanks to the different molecular packings in the crystal lattice. In 4-DBpFO single crystals, the crystal structure is clearly different in the α and β phases. This motivated us to study the fluorescence spectrum of this crystal in the different phases. A sharp change upon the occurrence of the structural phase transition is expected. To study this, the temperature dependent fluorescence was studied below and above the phase transition. The results are presented in Figure 3.5.

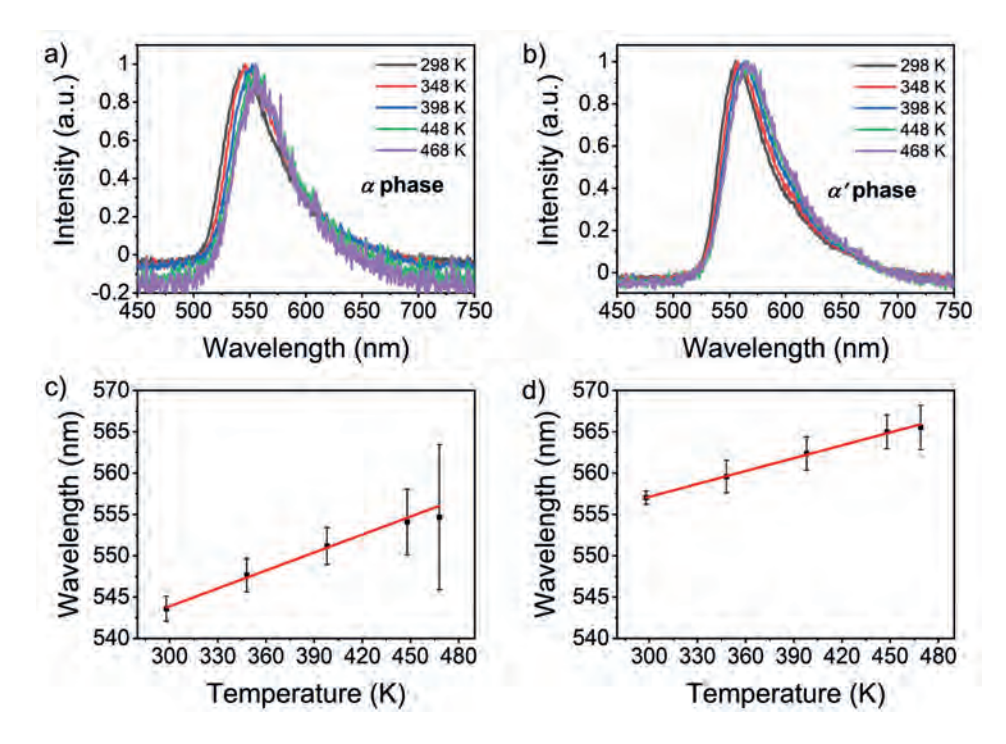


Figure 3.5. FL spectra of a phase 4-DBpFO and α ' phase 4-DBpFO at different temperatures. FL spectrum of a) a phase 4-DBpFO and b) a' phase 4-DBpFO single crystals. All spectra were normalized by the maximal intensity. Central wavelengths of the FL spectrum as function of temperature of c) a phase 4-DBpFO and d) a' phase 4-DBpFO single crystals. The red solid lines indicate linear fit. The error bars are obtained via peak fit of the spectra in a) and b).

The fluorescence emission spectra were obtained by exciting the crystal with a CW laser centered at 405 nm and detecting the emitted light with an Avantes spectrometer assisted with a LakeShore 340 temperature controller. Both α phase and α ' phase 4-DBpFO crystals are examined and compared in Figure 3.5. At room temperature, the central wavelength of FL emission for α phase 4-DBpFO is at 544 nm, for a' phase 4-DBpFO it is at 555 nm, indicating the energy difference of the excited states and the ground states in these two polymorphs. Upon heating up to 469 K, the FL spectrum of each crystal showed a linear red shift with a spanning range of 14 nm and 12 nm respectively (Figure 3.5c and 3.5d). The red shift of the FL central wavelength can be fitted very well with a linear function up to 469 K. The observed red shift is 0.07 nm/K with an error of 0.007 nm/K (Figure 3.5c). This can be attributed to temperature induced lattice expansion. Besides, the spectra became noisier at higher temperatures for both phases, as can be seen in Figure 3.5a and 3.5b, suggesting an unstable state at high temperatures. The intensity of the original spectra for both α and α phase was reduced upon increasing temperature, which is likely caused by non-radiative relaxation⁸⁹⁻⁹¹.

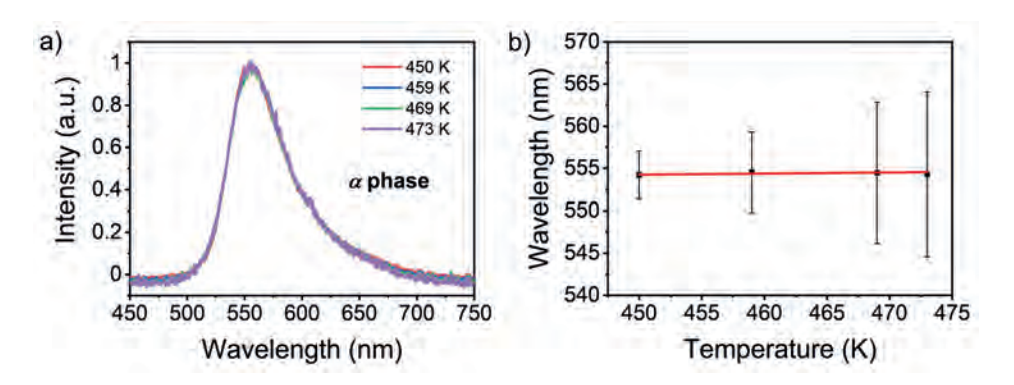


Figure 3.6. a) Temperature-dependent FL spectrum of α phase 4-DBpFO in the vicinity of the phase transition temperature of around 463 K. b) The central wavelengths extracted from the spectra are located around 554 nm, showing no abrupt changes across the phase transition. The error bars are obtained via peak fit of the spectra in a).

To prepare for further dynamic study of the phase transition in α phase 4-DBpFO, additional FL spectra were acquired in the vicinity of the phase transition temperature of α phase 4-DBpFO. The phase transition temperature for this specific crystal was determined at 463 K with a hot stage microscope. However, no significant spectral change was observed across the phase transition, as can be seen in Figure 3.6a. The central wavelengths of the FL spectra were extracted and plotted in Figure 3.6b. It is nicely fitted with a horizontal linear function, suggesting no frequency shift of FL spectra between the α and β phase 4-DBpFO. This finding shows that FL cannot serve as a probe to characterize the phase transition in 4-DBpFO in an optical pump-probe measurement.

3.5 Static birefringence of α and α ' phase 4-DBpFO

Crystals with orthorhombic symmetry are optically biaxial, and their refractive index can be described by an optical indicatrix with three principal axes parallel to their crystallographic axes. For both the α - and α '-phase that have rhombic crystal shapes, two crystallographic axes are parallel to the in-plane diagonals of the rhombus, while the other one is perpendicular to the surface of the crystals. When rotating such a rhombic crystal between two crossed polarizers under a polarization microscope, the crystal turns dark completely when its two in-plane diagonals are parallel to the polarizers. This means that the in-plane optical axes are along the diagonal directions, which is consistent with the crystal structures determined from XRD. When white light passes through a crystal placed between two crossed polarizers, the crystal shows birefringent color as the result of wave retardation between the two in-plane optical axes. The retardation value can be expressed by

$$R = d \cdot \Delta n = |n_f - n_s|$$

where d is the crystal thickness and Δn is the in plane birefringence value which is determined by the difference between the refractive index along the fast and slow axes. The fast optical axis is observed to be parallel to the crystallographic-c axis in the α -phase while it is parallel to the crystallographic-b optical axis in the α '-phase.

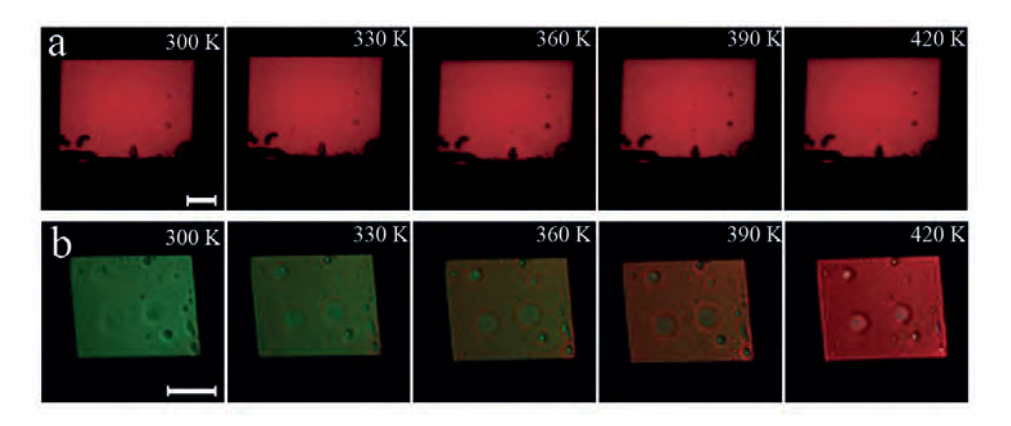


Figure 3.7. Birefringent color change of the α -phase (a) and the α '-phase (b) with temperature.

Interestingly, when single crystals are heated from room temperature to 420 K under a polarization microscope, the birefringence color of the α -phase stays unchanged (Figure 3.7a) while the color of the α '-phase changes rapidly with temperature (Figure 3.7b). This indicates that the wave retardation of the α -phase is insensitive to the temperature while it is very sensitive to temperature variation in the α '-phase. As there is no structural phase transition below 420 K in both structures, a structural phase transition induced birefringence change can be excluded in the α '-phase. The magnitude of the wave retardation change as a function of temperature was determined by an optical bench setup equipped with a photo-elastic modulator system (PEM) (refer to Chapter 2 Figure 2.4). Single crystals were positioned between two crossed polarizers which were oriented at -45° and 45° with respect to the PEM retardation axis, respectively. To measure the maximum wave retardation, the fast axis of the microcrystals was oriented parallel to the retardation axis of the modulator. A camera was used to calibrate the change of crystal positions during temperature variation. The used light source was a He-Ne laser with a wavelength of 632.8 nm. A lock-in amplifier and a DC voltmeter were used to detect the rms voltage V_{1f} of the detector signal at the PEM

frequency and the average voltage V_{DC} , respectively. The sample retardation value in radians r_a was calculated by

$$r_a = \sin^{-1}\left[rac{R_{1f}}{\sqrt{2}J_1\left(A
ight)}
ight]$$

where $J_1(A)$ is a Bessel function of the PEM retardation A and R_{1f} is the ratio of V_{1f} and V_{DC}

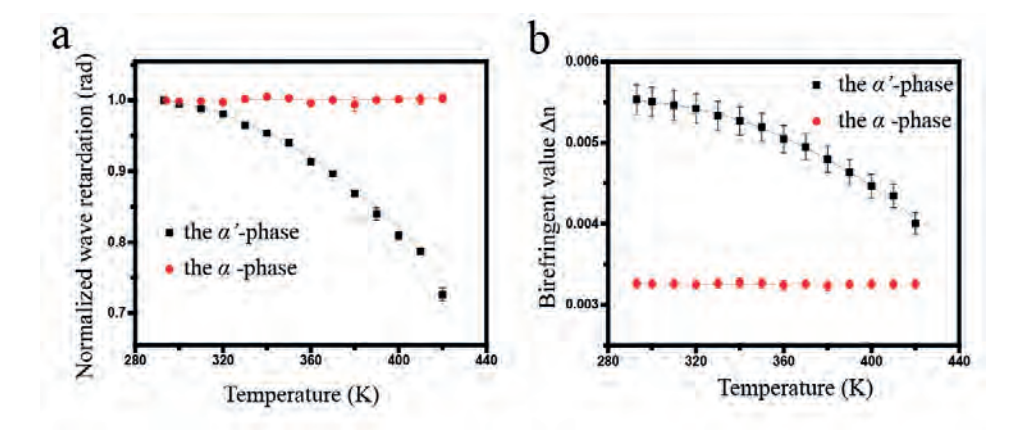


Figure 3.8. Retardation (a) and calibrated birefringence value (b) as a function of temperature.

The normalized results show that the wave retardation of the α -phase stays very stable upon heating (Figure 3.8a) up to the phase transition. On the other hand, the value of the birefringence in the α ' phase undergoes a strong and nonlinear decrease from room temperature to 420 K. As the thermal expansion along the normal direction of the crystal will slightly increase the wave retardation 92, this effect has to be taken in account. To quantitively determine the birefringence change, the thermal expansion ratio along crystallographic axes was determined by measuring the unit cell parameters via single crystal X-ray diffraction (Figure 3.9). The thermal expansion of the fast and slow optical axes changes linearly in both phases, which can be expressed by the Linear thermal expansion coefficients as $\alpha = \Delta L/(L \cdot \Delta T)$. Figure 3.8b shows a plot of Δn versus temperature after calibrating the thermal induced crystal thickness changes. The thicknesses of the α and α' phase refer to Figure 3.10. As the crystal is grown by self-assembly method, the surface is not completely flat. The thickness used in calibration is averaged as the laser beam covers a relatively large area of the sample surface. The Δn of the α -phase stays constant at around 0.0033 in the measured temperature range while the Δn of the α '-phase undergoes a nonlinear decrease from 0.0055 at room temperature to

0.0041 at 420 K. As the magnitudes of the thermal expansion ratio are very approximate in both phases and the α -phase even shows a larger anisotropy of inplane thermal expansion ratio than the α '-phase, this difference in their temperature dependent birefringence values cannot be simply explained by their thermal lattice expansions but should be closely related to their differences in molecular packing.

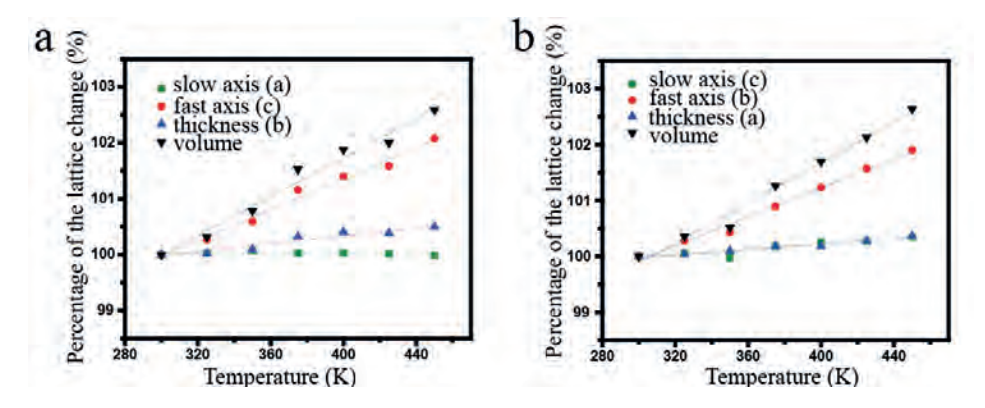


Figure 3.9. Thermal lattice expansion of the α -phase (a) and the α '-phase (b).

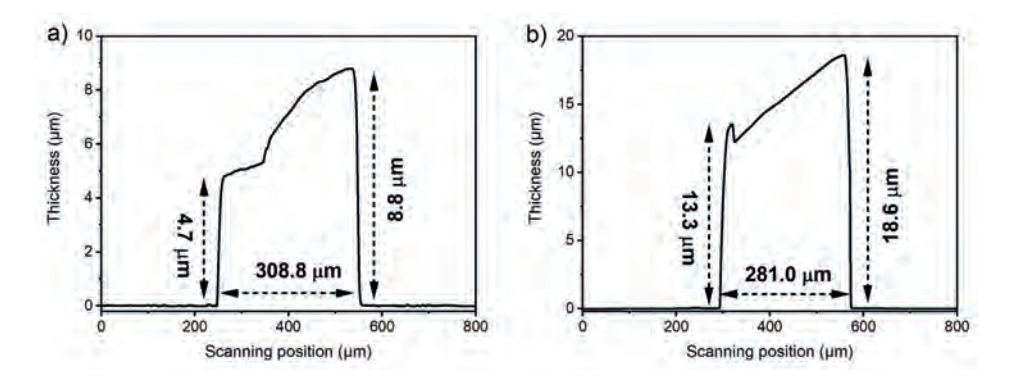


Figure 3.10. Thickness of a) α ' phase (8.8 µm) and b) α phase (18.6 µm) single crystals.

3.6 Linear birefringence change across the thermosalient phase transition in α phase 4-DBpFO

A structural phase transition with a large shape change in organic crystals will result in an abrupt change in birefringence because of the molecular rearrangement. The α phase 4-DBpFO crystal undergoes an abrupt large anisotropic in-plane shape change with the crystallographic α -axis shrinking 9.3% and the c-axis expanding 6.9%²². Therefore, a strong difference in birefringence is expected

to be observed before and after the structural phase transition. Figure 3.11 shows the birefringent change in the vicinity of the phase transition temperature, where a hysteresis loop is obviously seen, coinciding with the first-order nature of this structural phase transition. This is measured with a polarized probe beam going through the α phase 4-DBpFO crystal and the rotation of the probe polarization is registered as birefringent change. The intensity of rotation change is converted into the unit of degree. The fitted phase transition temperatures are 462 K for heating and 460 K for cooling processes. The fact that the rotation change recovers back to its original value is in line with the fact of the reversibility of the structural phase transition in α phase 4-DBpFO crystal, consolidating the reliability of using the birefringence change as a probe parameter to detect the structural change in α phase 4-DBpFO crystals.

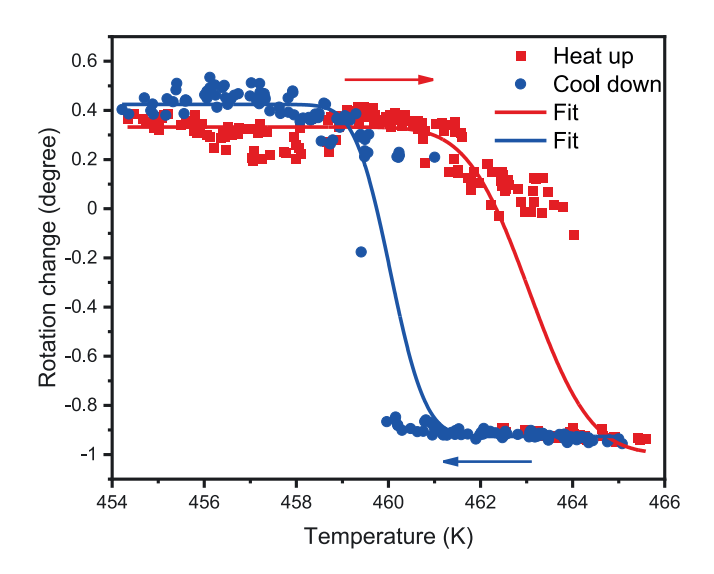


Figure 3.11. Polarization rotation change as a function of temperature. The sample system is heating at a speed of 2 K/min. The raw data are registered as squares and dots for heating and cooling respectively. The solid lines are the fitting results by error function. The y-axis has been calibrated into rotation angles in unit of degrees.

3.7 Conclusion and outlook

In summary, we reported the photoluminescence and birefringence of two orthorhombic crystal structures with similar crystal habits, being assembled from the same compound of 4-DBpFO, but showing totally different birefringence changes with temperature. The birefringence value changes rapidly with temperature in the polar structure of the α '-phase which involves parallel dipoles. In contrast, it stays very stable in the α -phase involving anti-parallel dipoles before

the structural phase transition temperature. When the in-plane lattice undergoes a significant anisotropic expansion at the thermosalient phase transition, the birefringence changes suddenly. These results show that the temperature dependent birefringence value changes are independent of lattice expansion but closely related to their molecular packing. The distinct behavior of temperature dependent birefringence in the two structures of the same compound provide not only a reliable probe parameter but also a reference for designing birefringent crystal structures for various applications that involve temperature variation.



Chapter 4

Raman spectroscopic study of the thermosalient phase transition in 4-DBpFO single crystals

The drastic shape deformation that accompanies the structural phase transition in thermosalient materials offers great potential for applications as actuators and sensors, but the microscopic origin of this fascinating effect has remained obscure. Here we present direct spectroscopic evidence of the role of specific lattice vibrational modes in the structural phase transition in the robust thermosalient molecular crystal 4-DBpFO. Temperature-dependent Raman measurements supported by molecular dynamics simulations reveal that two low frequency vibrational-librational modes are directly related to the order parameter that describes this phase transition. These results reveal the importance of vibrational modes in this structural phase transition and provide a new aspect on the research of thermosalient effects and thermosalient material design.

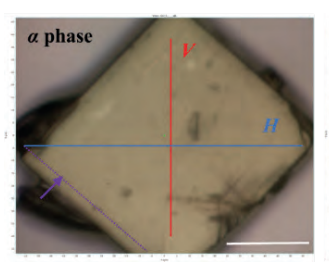
Part of this chapter is adapted from: S. Ghasemlou, X. Li, et al. "Identifying and controlling the order parameter for ultrafast photoinduced phase transitions in thermosalient materials" Proc. Natl. Acad. Sci. U.S.A. 121 (46) e2408366121 and from: X. Li, et al. "Revealing the role of vibrational modes in a thermosalient structural phase transition using Raman spectroscopy" (in preparation).

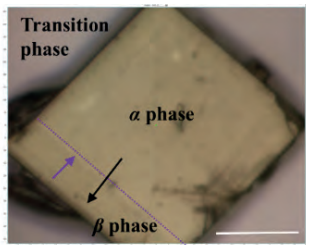
4.1 Introduction

Thermosalient crystals exhibit drastic shape deformations, which may lead to jumping or splitting, once they experience temperature changes²⁵. These remarkable properties grant them great potential for applications in actuators, sensors and artificial muscles⁹³. The macroscopic drastic responses are the external results of a microscopic solid-to-solid structural phase transition inside these crystals^{22,25}. However, these dramatic shape deformations often result in breaking, separation, or explosion, preventing detailed studies. As a result, the underlying microscopic mechanisms of these fascinating structural phase transitions have remained largely unknown. Recent studies have demonstrated that identifying the mechanism of the solid-state phase transitions is not only an academic discussion but also important for practical purposes. For a pharmaceutical agent, it is safer to find a polymorphic form that does not undergo a cooperative phase transition since the low energy barrier for the transition can be supplied in ambient conditions. In organic electronics, however, fast-reversible transitions give access to forms with varying charge carrier mobility without destroying the structure⁹⁴.

Recently, a thermosalient crystal self-assembled from the fluorenone derivative 4-D BpFO (2,7-di([1,1'-biphenyl]-4-yl)-fluorenone) 32,35 was reported with excellent reversibility and robustness 1 of going from the low temperature α phase to the high temperature β phase. Moreover, the phase boundary appeared controllable by finely tuning the temperature 36 , which offers the unique possibility to study the optical properties in both phases simultaneously.

The thermosalient phase transition in 4-DBpFO is a temperature induced structural transformation from an orthorhombic α phase to a monoclinic β phase, resulting in a crystal shape change from square to rhombic around 190°C (see Figure 4.1). Single crystal XRD revealed that this phase transition is accompanied by a change of the dihedral angles θ and φ^1 (indicated in Figure 4.2). However, the origin and mechanism of this structural change from the α phase to the β phase, and the corresponding transition order parameter have remained largely unknown, not in the least because of the fragility of the materials.





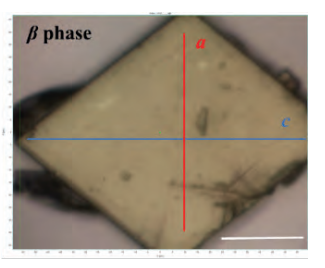


Figure 4.1. Shape transformation and phase boundary propagation of 4-DBpFO single crystal upon heating.

a) Square shape α phase single crystal at 180°C. The red line denotes the vertically polarized input laser beam and the blue line denotes the horizontally polarized output beam. A phase boundary is appearing from the bottom left edge, marked with a dashed purple line. The purple arrow points into the propagation direction of the phase boundary. b) Transition state single crystal at 182.5°C. The phase boundary has propagated further and is fixed at the dashed purple line position. The black arrow indicates the line scan measurement direction from the α to the β phase. c) Rhombic shape β phase crystal at 188.4°C. The red line marks the contracted crystallographic a-axis and the blue line marks the stretched crystallographic c-axis. This means that the crystallographic a-axis is parallel to the vertical polarization of the incoming laser beam (V||a) and the crystallographic c-axis is parallel to the horizontal beam (H||c). Scale bar is 50 μ m.

The images of the crystals were obtained with a built-in optical microscope, where the structural phase transition is identified by the drastic shape deformation from a square shaped α phase 4-DBpFO single crystal into a rhombic shape β phase crystal at 188.4°C²². Note that the exact phase transition temperature varies from crystal to crystal due to differences in size, thickness and impurities.

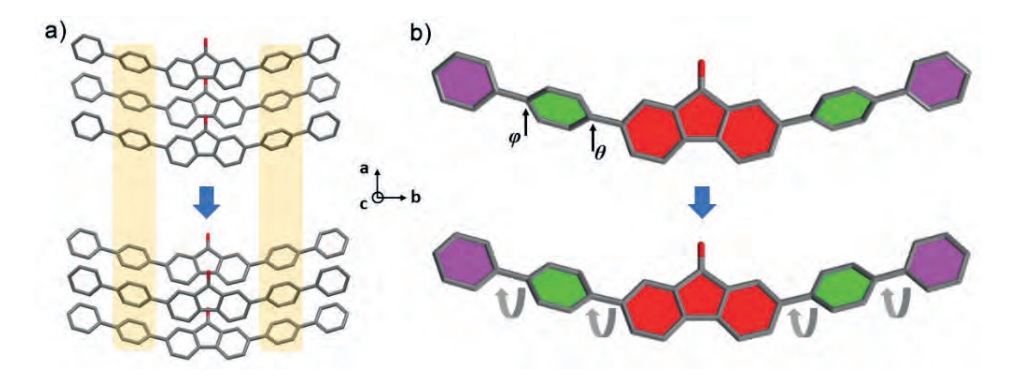


Figure 4.2. Molecular conformation of a phase (top row) and β phase (bottom row) 4-DBpFO. a) Crystal lattice viewed along the crystallographic c-axis. The permanent dipole (C=O double bond direction) is along the crystallographic a-axis and the transition dipole (the long molecule direction) is along the crystallographic b-axis. The blue arrow indicates the transition from the α phase to the β phase. The yellow shadow points out the phenyl ring that rotates during the phase transition b) Zoomed in molecular conformation comparison before (top) and after (bottom) phase transition. The phenyl rings on both sides of the fluorenone core are indicated with green (ring1 groups) and purple (ring2 groups), respectively. The fluorenone core is colored red. The dihedral angles ϑ and φ that accompany the phase transition are marked with black arrows, and their rotations are indicated with gray curly arrows in the β phase, suggesting a more planar molecular structure in the β phase. Crystallographic structures of these two phases are adapted from 22 .

Previous studies on thermosalient phase transition using Raman spectroscopy hardly observed differences between two phases, mostly because the study focused on the molecular features which are above 200 cm⁻¹, neglecting the vibrational modes at low frequencies²⁰. Relative Raman studies on fluorenone-based molecular structures are also reported in the mid- and near- infrared regions⁹⁵⁻⁹⁷. However, the typical Raman features that are closely related to the structural phase transition are located at the far-infrared region, where the phonon modes are active. Therefore, in our work, we will mainly focus on the low-frequency region of the Raman spectra.

Here, we report a temperature dependent study of the vibrational modes in 4-DBpFO single crystals by micro-Raman experiments. We identified two low frequency lattice vibrational-rotational modes that exhibit strong broadening and blue shifting upon the thermosalient structural phase transition. Molecular dynamics simulations allow us to identify these modes with rotations of the phenyl rings with respect to the fluorenone centre, consistent with the observed static rotations of these rings in the new phase. In addition, we observe changes of some other modes, consistent with the change of symmetry going from the low temperature orthorhombic α phase to the high temperature monoclinic β phase. These results show that, in contrast to a soft vibrational mode behaviour as is

usually observed in second order phase transitions 98,99, this first order thermosalient phase transition is induced by two rotational modes, the symmetries of which are directly related to the new phase.

4.2 Polarization dependent Raman spectra

Polarization and temperature dependent Raman experiments were performed to study the α to β phase transition in 4-DBpFO. The polarization dependent measurements assist mode assignment with respect to crystal and molecular symmetries⁴⁵, whereas the temperature induced changes aim to deduce the underlying mechanism and order parameter of the phase transition.

The experimental set up was described in Chapter 2 Figure 2.3. In brief, we used the Horiba LabRAM HR Evolution system for the polarized Raman experiments. The vertical (denoted as V) input polarization was parallel to the crystallographic aaxis, while the horizontal (denoted as H) input polarization was parallel to the crystallographic c-axis (see Figure 2.3 and 4.1). The input polarization is by default vertically polarized, and can be tuned into horizontal polarization by applying a half-wave plate, as shown in Figure 2.3. An analyser was installed in front of the detector so that only certain polarization (V or H) scattered light is allowed to go into the detector.

In a molecular crystal with N atoms per molecule and Z molecules per unit cell, each atom possesses three degrees of freedom and therefore a total of 3NZ vibrational modes are possible 100. In a single unit cell of 4-DBpFO crystal, there are 4 molecules. Each of the molecules contains 62 atoms. Therefore, there are 744 (3*62*4=744) normal modes of vibrations for the 4-DBpFO molecule, including 3 acoustic branches and 741 optical branches 101,102. Among the optical modes, part of them are Raman active, and other infrared active. As both α (Pnma) and β (P2₁/n) phases are centrosymmetric structures, the infrared-active modes cannot be present in a Raman spectrum¹⁰³. Identifying all these modes is not only extremely complex but also beyond the scope of this chapter, where we use Raman spectroscopy to help to unravel the mechanism of the thermosalient phase transition. As that involves changes in the crystal structure and symmetry, we will focus our attention to the low frequency (below 200 cm⁻¹) lattice vibrations.

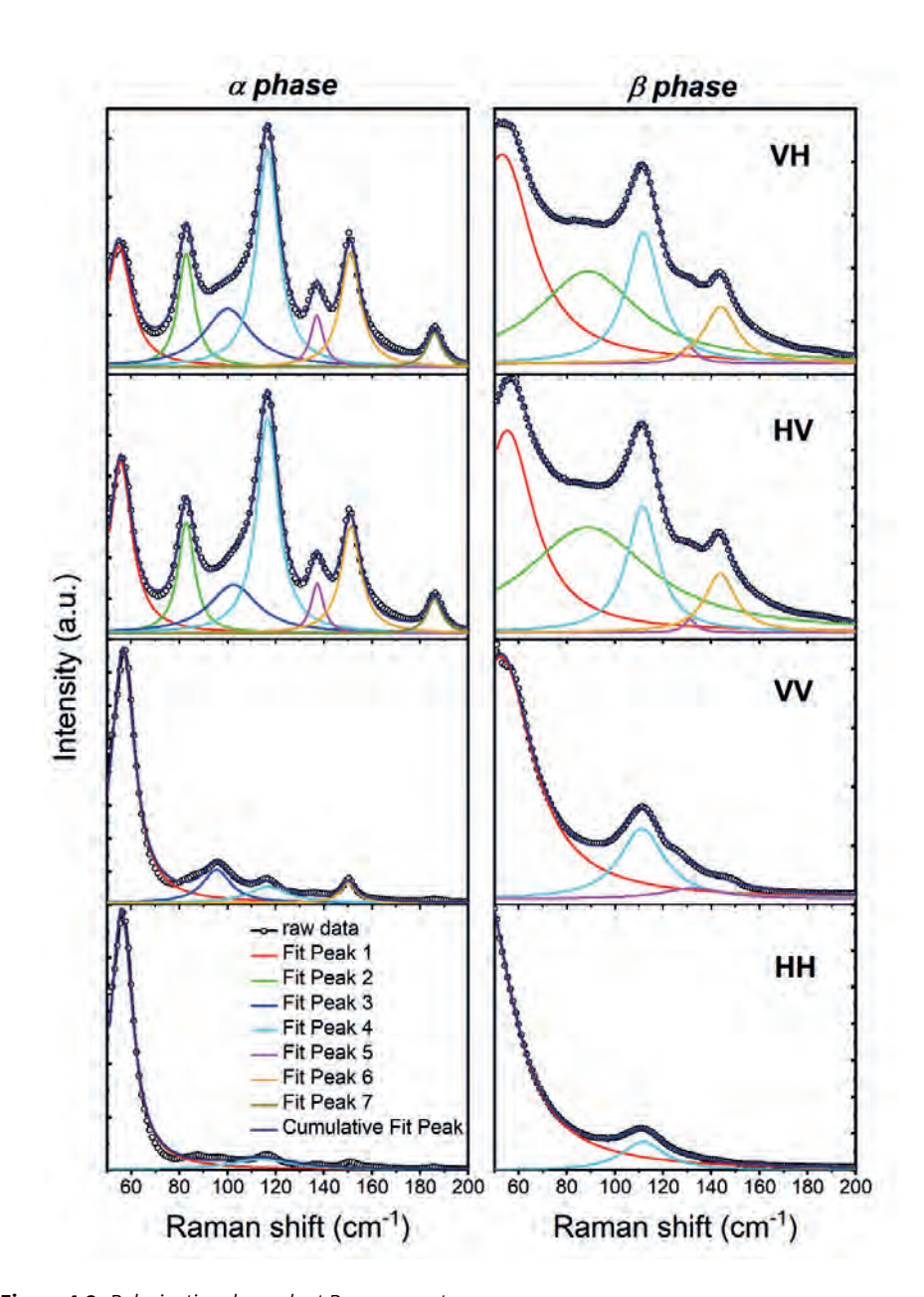


Figure 4.3. Polarization dependent Raman spectra.

Measured Raman spectra of α phase at room temperature (left column), and β phase at 189.3°C (right column). The polarizations of input laser and scattered light are denoted on the right column for each row. The raw experimental data are plotted as black solid lines with round circles. The Raman peaks, as denoted in the bottom left figure, are fitted with Lorentzian functions and are plotted in different colors. The cumulative fitted spectra are plotted in navy color and fit the raw data very well. Precise peak wavenumbers can be found in Table 4.1.

Phase	Polarization	Peak 1	Peak 2	Peak 3	Peak 4	Peak 5	Peak 6	Peak 7
α (RT)	VH	54.8	82.8	100.1	116.6	137.1	151.1	185.9
	HV	55.6	82.9	102.5	116.6	137.3	151.2	186.0
	VV	56.6	-	95.5	116.8	-	150.2	-
	нн	56.0	-	-	114.2	-	-	-
β (НТ)	VH	53.2	88.8	-	111.8	130.7	143.9	-
	HV	55.2	88.9	-	111.5	131.2	143.7	-
	vv	52.7	-	-	111.2	132.4	-	-
	нн	45.2	-	-	111.7	-	-	-

Table 4.1. A summary of Raman modes up to 200cm⁻¹.

All the wavenumbers are extracted by fitting the raw data in Figure 4.3 with Lorentzian functions.

For a well-structured solid-state crystal, the polarized Raman spectrum can assist mode assignment by diagnosing the behaviours of different modes under different polarizations. Figure 4.3 presents the raw experimental Raman spectra, including their Lorentzian fits, that were obtained under identical experimental conditions. The intensities of the raw data indicate the relative amplitudes of each Raman mode in each individual spectrum. The spectra are plotted starting from 50 cm⁻¹ as this is close to the low frequency spectral limit (as discussed in section 4.3). The peak positions of the fitted Raman modes are summarized in Table 4.1.

Analysis of the observed Raman modes.

Raman active vibrational modes can be divided in symmetric (A) and asymmetric (B) modes, where symmetric and asymmetric geometry relates to the movement of corresponding lattices. The Raman scattering probabilities of the various modes can be described by scattering matrices. Based on the point group symmetry of α phase 4-DBpFO, D_{2h} (mmm), 4 Raman tensors can be identified as stated below^{104,105}:

$$egin{array}{ccc} egin{array}{ccc} a & & & & \ & b & & \ & & c \end{array} egin{array}{ccc} egin{array}{ccc} a & & & \ & d & & \ & & \end{array} \ egin{array}{ccc} egin{array}{ccc} a & & & \ & & \ \end{array} egin{array}{ccc} egin{array}{ccc} a & & & \ & & \ \end{array} egin{array}{ccc} B_{1\mathrm{g}} & & & \ & & \ \end{array} \ egin{array}{ccc} B_{1\mathrm{g}} & & & \ & & \ \end{array} \ egin{array}{ccc} B_{2\mathrm{g}} & & & \ & f \end{array} \ egin{array}{ccc} & & & \ & f \end{array} \ egin{array}{ccc} \end{array}$$

where A_g represents symmetric modes and B_{1g} , B_{2g} , and B_{3g} represents asymmetric modes.

Experimental configuration in Porto's notation	${f A_g}$	$ m B_{2g}$
-Y(XX)Y	×	
-Y(XZ)Y		×
-Y(ZZ)Y	×	

Table 4.2. A schematic overview of potential Raman modes in a phase 4-DBpFO.

Based on the experimental configuration, not all predicted Raman modes will be observed. As shown in Table 4.2, only $A_{\rm g}$ and $B_{\rm 2g}$ modes can be seen in the backscattering geometry (Porto notation -Y(**)Y)105. Ag modes are active when the incident polarization of light is parallel to the output polarization (-Y(XX)Y and -Y(ZZ)Y) whereas B_{2g} modes are active when the input and output polarizations are crossed (-Y(XZ)Y). The -Y(XX)Y and -Y(ZZ)Y configurations correspond to VV and HH polarizations in our experiment, and (-Y(XZ)Y) corresponds to HV and VH polarizations. This suggests that the Raman spectra under HV and VH polarizations should be identical, which is confirmed by the experimental results in Figure 4.3 and the fitted results in Table 4.1. Moreover, the table also indicates that Ag modes and B_{2g} modes cannot appear in the same configuration. The modes that are present in parallel polarization are Ag (symmetric) modes (Peak 1 and Peak 4), whereas the modes that are present in crossed polarization configuration are B_{2g} (asymmetric) modes (Peak 1, Peak 2, Peak 3, Peak 4, Peak 5, Peak 6, Peak 7)^{106,107}.

Peak 1 and Peak 4 seem to exist in both crossed and parallel polarizations. Peak 1 appears as the dominant mode in parallel polarizations whereas it is the second strongest mode in crossed polarizations. The co-existence of this mode in both configurations may imply local disorder in the crystalline material. However, the intensity of Peak 4 is remarkably reduced when the polarization is changed to parallel (VV and HH in Figure 4.3). The appearance of this mode in parallel polarizations thus can be attributed to the exceptionally high intensity of this mode which is not effectively eliminated by the optical filter when it is changed to parallel polarizations.

To conclude, in lpha phase, Peak 1 is an $A_{\rm g}$ (symmetric) mode and the rest (Peaks 2-7) are B_{2g} (asymmetric) modes.

Now let's look at the β phase.

The point group of β phase 4-DBpFO is C_{2h} (2/m), with the 2 corresponding Raman tensors as stated below 105:

$$egin{array}{cccc} egin{array}{cccc} a & d & & \ d & b & & \ & & c \end{array} egin{array}{cccc} egin{array}{cccc} a & d & & \ d & b & & \ & & c \end{array} egin{array}{cccc} egin{array}{cccc} a & d & & \ & & f \ e & f \end{array} \end{array}$$

Experimental configuration in Porto's notation	${f A_g}$	$ m B_{g}$
-Y(XX)Y	×	
-Y(XZ)Y		×
-Y(ZZ)Y	×	

Table 4.3. A schematic overview of potential Raman modes in β phase 4-DBpFO.

Similar to the lpha phase, the modes that are present in parallel polarization are $A_{
m g}$ (symmetric) modes, whereas the modes that are present in crossed polarization configuration are $B_{\rm g}$ (asymmetric) modes. According to Figure 4.3 and Table 4.1, two Raman modes (Peak 3 and Peak 7) disappear in the β phase. Peak 2, 4, 5 and 6 belong to $B_{\rm g}$ (asymmetric) modes as they only exist in crossed polarizations. Peak 1 is the dominant $A_{\rm g}$ (symmetric) mode. Peak 4 is stronger than in the α phase, which is presumably related to scissoring motion of inner phenyl ring.

To compare with α phase, two asymmetric Raman modes (3 and 7) disappear in the β phase, and the intensity of peak 4 becomes larger.

4.3 Temperature dependent Raman spectra

Temperature-dependent Raman spectra were measured with assistance of a temperature controller. The incident laser beam (633 nm) was by default vertically polarized, which is parallel to the crystallographic a-axis (see Figure 2.3).

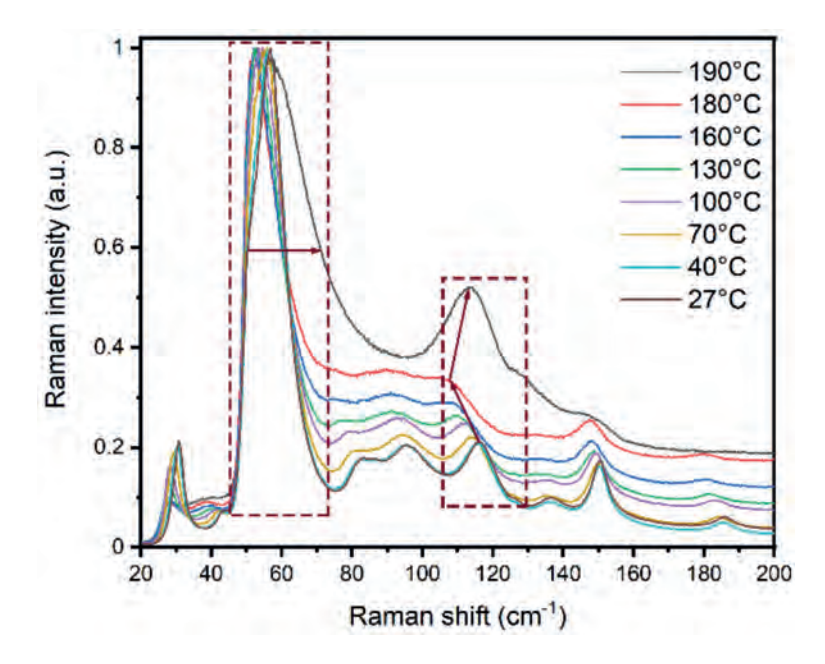


Figure 4.4. Temperature-induced spectral changes in VN polarization. The α phase 4-DBpFO single crystal was heated with intervals of 30°C, from 27°C to 190°C. 8 modes were clearly visible at room temperature and they all exhibited a red shift upon heating up to 160°C. This crystal transforms to the β phase at the temperature of 182.5°C. A sharp blue shift of the 106 cm⁻¹mode, marked with red solid arrows, was observed upon the phase transition. The spectra were normalized to 1 by the strongest intensity of each spectrum (at around 50 cm⁻¹). The red dashed boxes are quides to the eyes to accentuate the blue and red shifts upon heating.

A set of Raman spectra were first acquired in VN polarization as a function of temperature (see Figure 4.4). In general, 7 modes can be identified at room temperature, and all of them, to different extent, exhibit a red shift and broadening upon heating up to 160°C. These are induced by normal thermal (expansion) effects¹⁰⁸. The elevated baseline is attributed to increasing fluorescence at higher temperatures. Moreover, two abrupt spectroscopic changes are observed in this polarization at the highest temperature (190°C): the sudden broadening of the 50 cm⁻¹ mode and a sharp blue shift of the mode at 106 cm⁻¹. These two significant spectroscopic changes are likely to be closely related to the structural phase transition in 4-DBpFO that happened at 182.5 °C in this crystal.

As can be seen in Figure 4.4, a strong spectral broadening occurs at the right hand side of the Raman peak near 50 cm⁻¹ while on the left hand side the spectra overlap perfectly, regardless of temperature change. On the one side, the spectral broadening carries interesting and important information on the structural change between α phase to the β phase 4-DBpFO crystal. On the other side, the physical

cutting on the left hand side (due to the instrumental cut-off) makes it difficult to analyse if it is a symmetric broadening of this mode.

A set of temperature dependent Raman spectra were acquired in VH polarization, to explicitly study the mode changes in the vicinity of the phase transition temperature (see Figure 4.5). The presented spectra in Figure 4.5a are normalized by the intensity of the mode at 148 cm⁻¹ whose intensity remained relatively constant for different temperatures and phases. The spectra in Figure 4.5a are fitted with the same function as in Figure 4.3, and the 7 Raman active modes presented in table 1 can still be identified with some red shift due to thermal effects. The changes of these 7 modes as a function of temperature are extracted from the fitting results and plotted in Figure 4.5b.

Three kinds of changes can be distinguished:

- 1) frequency shifts (blue shift: mode 4, red shift: mode 6);
- 2) mode appearance (mode 1) and disappearance (mode 2 and mode 7);
- 3) no change (mode 3 and mode 5).

The Raman modes at 30 cm⁻¹ and 40 cm⁻¹ (as can be seen in Figure 4.4) are not discussed here because of the low reliability at these frequencies close to the cutting edge (~ 50 cm⁻¹) of the Raman spectrometer. This spectral limitation also leads to the fitting error of the Peak 1 at around 50 cm⁻¹. As can be seen from Figure 4.5a, a new mode emerges at the frequency of 55 cm⁻¹ as a strong shoulder peak to the Raman peak at 50 cm⁻¹. However, the spectral fitting with a Lorentzian function (Figure 4.5c and 4.5d) cannot distinguish these two modes and thus gives a blue shift after the phase transition, as stated as mode 1 in Figure 4.5b.

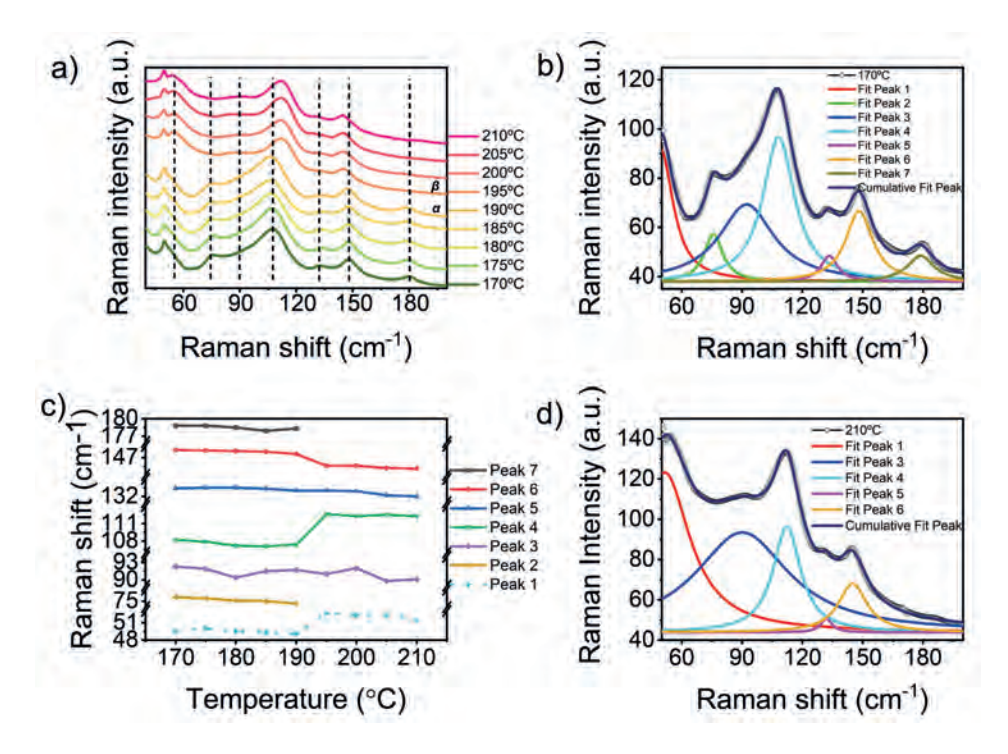


Figure 4.5. Evolution of Raman spectra of 4-DBpFO single crystal as function of temperature in VH (vertical in, horizontal out) polarization.

a) Temperature-dependent Raman spectra of the vibrational frequency region. The a phase 4-DBpFO single crystal was heated with intervals of 5° C, from 170° C to 210° C. 7 Raman-active modes are identified in the α phase and they are marked with vertical black dashed lines. This crystal transforms into the β phase at the temperature of 190° C. The spectra are normalized by the intensity at 148 cm^{-1} . b) Extracted frequency changes of 7 Raman modes as a function of temperature. Errors obtained from the fitting results are plotted together with Raman shifts but they are as small as the plotted symbols. c) and d) show the spectra of α phase (at 170° C) and β phase (at 210° C) that are fitted with the same function as in Figure 4.3. The decomposed Raman peaks are plotted corresponding to the 7 peaks in Figure 4.3 as well.

The thermal effects in the vicinity of phase transition temperature (Figure 4.5) are very small compared to the phase transition induced Raman shifts. The red shifts of the 7 modes (~1 cm⁻¹ over 20 degrees) are almost negligible compared to the large temperature induced shifts as observed in Figure 4.4. Furthermore, the volume change in the thermosalient phase transition in 4-DBpFO (2.7%²²) is too small to induce significant spectral changes. Therefore, the spectroscopic changes around 190°C in Figure 4.5b are mainly induced by the structural phase transition ^{13,109,110}.

4.4 Molecular dynamics simulated Raman spectra

To understand the observed Raman spectra, molecular dynamics simulations were done by Dr. Daria Galimberti (Theoretical Chemistry Department).

The theoretical spectra have been computed by molecular dynamic simulations through the time-correlation function formalism developed by D.R. Galimberti and H.M. Cuppen. In particular, they adapted and further developed the methodology proposed by Galimberti et al. 111,112, to accurately describe the THz Raman spectra of the system under study.

In a nutshell, the system is simulated using classical molecular dynamics simulations allowing for long time scales and large system dimensions that are required to capture the low frequency modes, but these are combined with abinitio accuracy on the Raman activity.

We have divided the molecule into three different fragments and color coded them (see also Figure 4.2): the fluorenone ring system (red), ring1 (middle phenyl rings, in green) and ring2 (outer phenyl rings, in purple). The spectrum further consists of contributions of the interactions between these three fragments. Note that the contribution of each component in the molecule to the spectrum can also be negative.

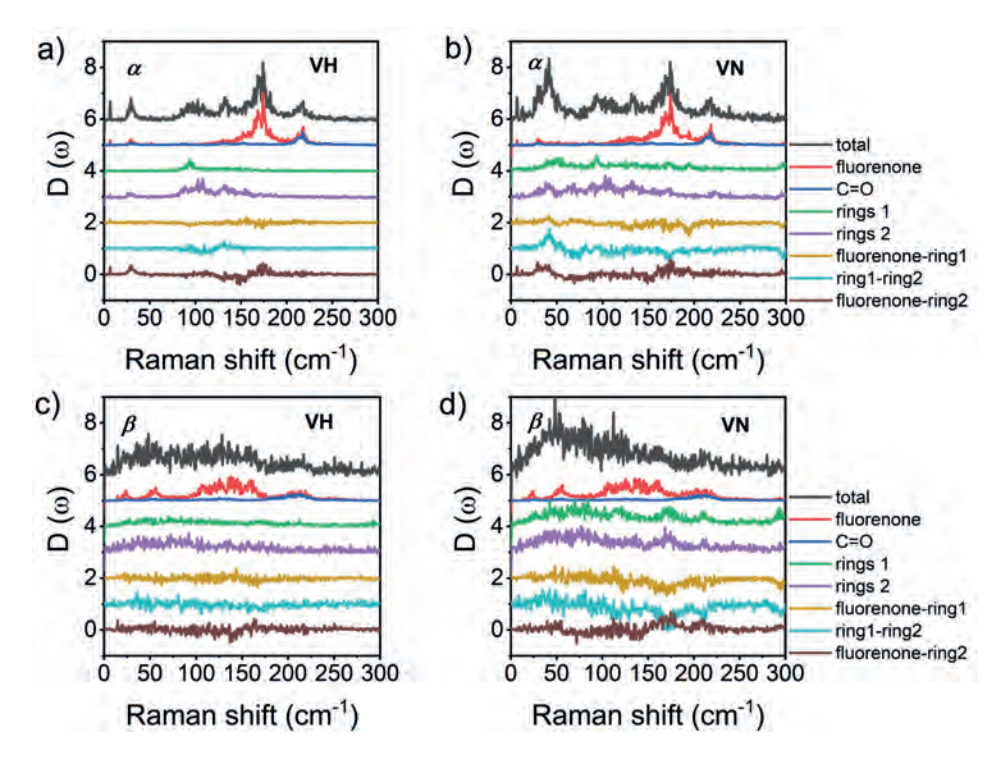


Figure 4.6. Simulated Raman spectra of α and β phase 4-DBpFO single crystal. The polarization was set as VH (a and c) and VN (b and d). The total spectrum for VH and VN is given in black at the top. It is then decomposed and assigned into different fragments of the 4-DBpFO molecule. The spectral contribution of each fragment and their interactions have been plotted in different colours.

All the simulations, for both α and β phase, were done at room temperature, so temperature induced changes between the two phases are excluded. In the α phase (Figure 4.6a and 4.6b), the fluorenone core and ring2 groups contribute the most to the overall spectrum in the VH polarization, whereas in the VN polarization ring1 and ring2 groups give the main contributions. The vibrational modes in VH polarization suggest some large amplitude motion where the molecule bends, which should be sensitive to the ac plane. In the β phase (Figure 4.6c and 4.6d), the overall Raman intensity decreases and the background noise increases. This is because of the highly unstable state of the β phase where the crystal structure is vibrating strongly.

Next, the simulated Raman spectra are discussed in combination with the experimental results and some of the modes listed in Figure 4.5b are assigned to specific vibrations in the crystal lattice.

In the α phase Raman spectra (Figure 4.6a and 4.6b), the complex mode around 55 cm⁻¹ (Figure 4.5a) is shown at 48 cm⁻¹ in VN polarization (Figure 4.6b) but not in VH polarization (Figure 4.6a), confirming its existence in parallel polarizations as discussed in section 4.2. As can be seen from Figure 4.3, in parallel polarizations, the mode at 55 cm⁻¹ is the strongest mode in both V and H incident polarizations. This implies that this mode has projections along both the a- and c-axis, as these axes are parallel to the V and H polarized beam respectively. The collinearity of the lattice vibration direction and the polarization of incident beam brings enhancement on the amplitude of the Raman spectrum. Therefore, this mode is connected to a symmetric motion that is out-of-plane (ac plane, refer to the a- and c- axis in Figure 2.3). Considering the possible out-of-plane motions in the α phase, this can be attributed to the rotations of ring1 and ring2 groups along the crystallographic b-axis.

In the β phase, this mode broadens to the higher frequency in the VN polarization (Figure 4.6d), in line with the analysis of the emerging new mode in Figure 4.5a. According to the break-down analysis in Figure 4.6d, this mode gets large contributions from the ring1 and ring2 groups. These two groups arrange in a more planar structure when the crystal transitions to the β phase, increasing the hindrance for such out-of-plane rotations, thus inducing mode hardening, leading to blue shift. In the meantime, more random vibrations can be expected from the ring2 groups due to the relatively large freedom it possesses. The new mode at relatively higher frequency could originate from ring2 groups while the ring1 group kept its original frequency. Moreover, a similar wagging vibration originating from the phenyl ring (comparable to ring2 groups in 4-DBpFO) was reported in 2021, where a Raman feature at the frequency of 50/58 cm⁻¹ was assigned to the phenyl ring wagging mode of a fluorenone derivative, DPFO¹¹³. Therefore, the mode at 55 cm⁻¹ is assigned to symmetric wagging motions of ring1 groups while ring2 groups contributed to the broadening of this mode when the structural transition occurs.

The mode at around 180 cm⁻¹ can be compared to the mode at around 175 cm⁻¹ in the simulated Raman spectra in Figure 4.6. This mode is present in the α phase but not in the β phase, in accordance with the disappearance of this mode in Figure 4.5a and 4.5b. In the α phase, this mode is visible in both VN and VH polarizations, proving the asymmetric nature of this B_{2g} mode. From the break-down analysis, this mode is mainly rooted in the fluorenone core. More specifically, the phenyl rings in the fluorenone core are the origin of this mode while the C=O bond solely contributes to the peak at 220 cm⁻¹. The interactions of fluorenone-ring1 and ring1ring2 give negative contributions to this mode, as can be seen in Figure 4.6a and 4.6b. It suggests that the motion of this mode is impeded by the ring1 groups. Therefore, this mode could be asymmetric wagging of the phenyl rings in relative to C=O bond (188a2 motion, simulations are done in gas phase 4-DBpFO by Dr. Daria Galimberti). The motion rotates the two phenyl rings to opposite directions of the fluorenone core plane, squeezing the rotating room of ring1 groups. The upand down- rotations transmit to the ring2 groups and attract the ring2 groups closer to the fluorenone core. Thus, positive contributions from fluorenone-ring2 interaction can be seen in Figure 4.6a and 4.6b. When the α phase is transformed into β , the planar construction prohibits this movement and thus this mode disappears. Therefore, this mode signals the formation of a planar structure in the β phase.

The mode at 106 cm⁻¹ exhibits a large blue shift (>7 cm⁻¹) in both VN and VH polarized Raman spectra (Figure 4.4 and 4.5). This mode is also seen in the simulated α phase spectra (Figure 4.6a and 4.6b). In the break-down analysis, the origin of this mode is attributed to ring2 (refer to purple spectrum in Figure 4.6a and 4.6b) as the peak position at ring2 matches with the total spectrum. When the crystal transforms into the β phase, the ring1 groups' contribution to this mode grows (green spectrum in Figure 4.6c and 4.6d), especially in VN polarization. In the meantime, the frequency of this mode is also shifted to ~112 cm⁻¹, which can be deduced from both the break-down analysis and the total spectrum in Figure 4.6c and 4.6d. This blue shift is in accordance with the blue shift observed in Figure 4.5. The hardening behaviour of this mode resembles the mode at 4 THz in Figure 4.8, section 4.6, where the origin is attributed to the torsion of both ring1 and ring2 groups (both θ and φ). Considering the co-contribution of ring1 and ring2 groups to this Raman mode, one can attribute this hardening behaviour of this mode to the torsion motion of ring1 and ring2 groups that causes change in the molecular bond length along the long molecular direction (transition dipole direction). This torsion motion becomes more competitive when the crystal is transformed into the more planar structure of the β phase, which leads to the hardening of the motion. This coincides with the discussion in section 4.2, where an in-plane (ac plane) vibration is expected at the mode 106 cm⁻¹. Additional support can be found in the molecule gas-phase mode simulations in the transition from 96 cm⁻¹ to 101 cm⁻¹.

4.5 Line scan across phase boundary

As discussed above, the observed thermal changes in the Raman spectra are partly caused by the normal temperature dependence of the vibration and rotation modes of any (molecular) crystal. Fortunately, as we demonstrated before²², the first order character of the thermosalient phase transition in 4-DBpFO leads to the possibility

of observing the coexistence of the α phase and β phase at a fixed temperature^{25,36}. This coexistence allows a line scan experiment that provides insight on the mode changes at the transition from the α phase to the β phase without being obscured by temperature induced effects.

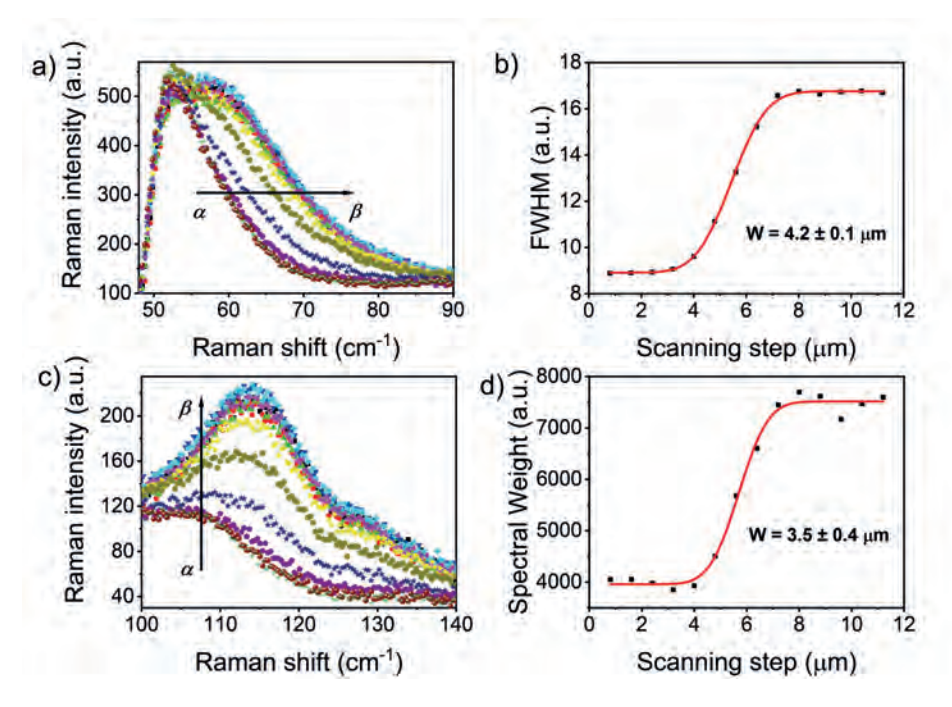


Figure 4.7. Line scan of Raman spectra across a phase boundary in VN polarization. a) and c) are the Line scan spectra at mode of 50 cm⁻¹ and 106 cm⁻¹. The dark arrows point out the phase propagation direction which is corresponding to the dark arrow direction in Figure 4.1b. b) and d) are the extracted FWHM and Spectral weight (dark solid squares) of mode 50 cm⁻¹ and 106 cm⁻¹ respectively. A step function (red lines) was applied to fit the extract the FWHM and spectral weight of these two modes. The fitted FWHM of mode 50 cm⁻¹ is 4.2 ± 0.1 µm, suggesting the width of the phase boundary. The fitted spectral weight of mode 106 cm $^{-1}$ is 3.5 \pm 0.4 μ m.

An in-situ Raman scan was carried out across the phase boundary (see Figure 4.1b) with a scanning length of 13 µm and a step size of 0.8 µm. Figure 4.7a and 4.7c present the changes of the Raman modes at 50 cm⁻¹ and 106 cm⁻¹ from the α to the β phase. The 50 cm⁻¹ mode broadens more than two times of its original width (see Figure 4.7b), which is consistent with a new band appearing at a higher frequency next to the 50 cm⁻¹ mode, as discussed in section 4.2. Note that the full width at half maximum (FWHM), which is normally used to quantify the spectral width, cannot accurately be determined, due to the instrumental cut-off, as mentioned earlier. Therefore, in Figure 4.7b we plotted the width, assuming that the band did not shift. A fitting using a step function was applied to the data of Figure 4.7b and the fitting result W = 4.2 ± 0.1 µm indicates the width of the phase boundary (see also Figure 4.1b). When the crystal is in the α phase, the width of this mode is stabilized at 9 (order parameter s = 0), whereas when the crystal fully transforms into β phase, the width is as large as 17 (order parameter s = 1). The steps captured in between are corresponding to order parameters in between 0 and 1. The definition of order parameter s is discussed in section 4.6.

As discussed in section 4.4, the mode at 106 cm⁻¹ is related to a torsional motion between ring1 and ring2 groups. In Figure 4.7c, this mode appears as a very broad band in the α phase, suggesting a very flexible and complex vibrational motion which leads to a merging with a neighboring band. With increasing order parameter, the peak of this band shifts to higher frequency (from 106 cm⁻¹ to 115 cm⁻¹, comparable to the shift in Figure 4.5b), and the shape of this band also grows into a sharp typical Gaussian-like Raman band. The blue shift indicates that the scissoring motion requires more energy in the β phase. Because of the shift and the band change, the spectral weight of this band changed dramatically after the phase transition. This is plotted and fitted in Figure 4.7d, whose sharp step behavior confirmed the first order nature of the $\alpha \rightarrow \beta$ transition.

4.6 Simulated spectrum for the transition order parameter

To understand the underlying mechanisms of the $\alpha \rightarrow \beta$ transition, molecular dynamics (MD) simulations were performed by Herma Cuppen and co-workers. Details of these simulations can be found in reference 114. In brief, MD simulates the dynamics of the materials based on Newton's equations of motion, where the forces acting on the atoms are determined from an interaction potential, a force field in this case. The resulting dynamics is due to a combination of kinetic (barriers of processes) and thermodynamic effects and the full vibration of the system is considered. As previous MD simulations showed that the transition is triggered by changes in the dihedral angles²², these angles can thus be used as the collective variable to describe the transition. If well-constructed, the collective variable (CV) should correspond to the order parameter or reaction coordinate of the phase transition. Here, they use a CV path that measures the progress of the transition by an order parameter s: at s = 0 the system is in the α phase and at s = 1the system is in the β phase. The value of s is obtained by projecting the average θ and φ dihedral angels on the path of transitioning from α (s = 0) to β phase (s = 1). The spectra (Figure 4.8a) are obtained by recording s as a function of time and taking the Fourier transformation of the autocorrelation function 114.

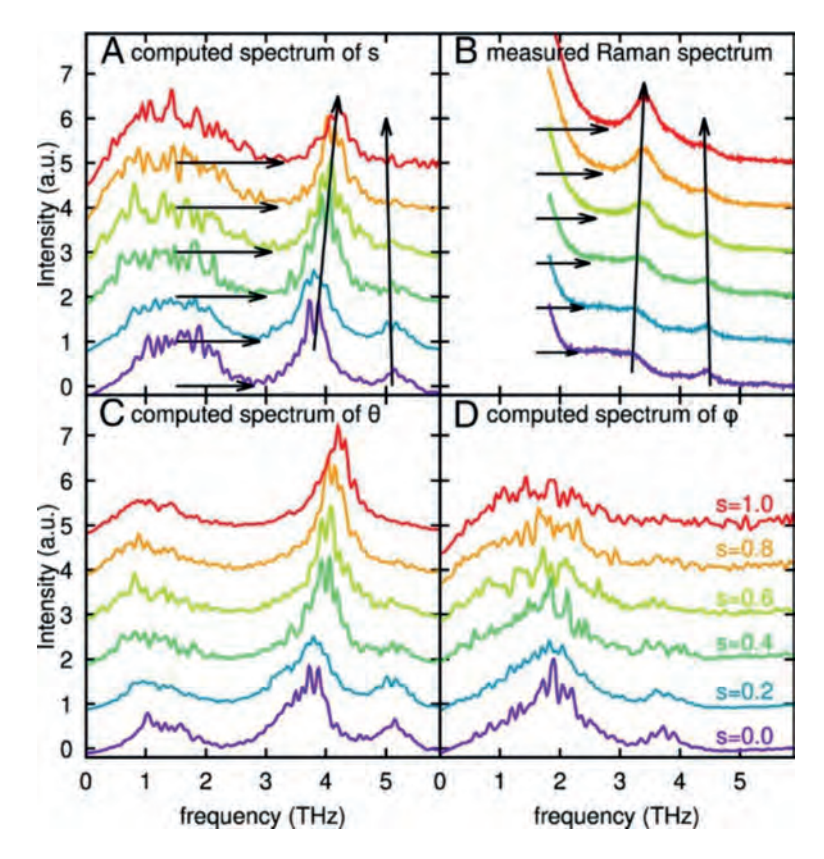


Figure 4.8. Vibrational spectra of the (A) transition order parameter for different stages along the transition pathway s. Panel (B) gives Raman spectra taken along the phase boundary of the crystal. Calculated vibrational spectra of the (C) dihedral θ and (D) dihedral φ are presented in panels (C) and (D), respectively. The spectral changes, such as peak shifts and broadening, are indicated with the vertical and horizontal arrows, respectively. The increasing noise level in the baseline with increasing s for (A) and (D) is due to the increasing mobility of the outer rings.

One should note that the modes in the calculated s spectrum can be either Raman or IR active, and hence they do not necessarily need to appear in the experimental Raman spectra, whereas also the relative intensities can be different. Furthermore, the calculated vibrational spectra only include the modes that are connected to the order parameter of the transition.

Figure 4.8 shows the good matching of the phase transition order parameter s between simulated spectra (Figure 4.8a, 4.8c and 4.8d) and experimental spectra (Figure 4.8b). These spectra were grouped based on their mean s value and averaged per group. At s =0 (α phase), four different features can be clearly distinguished. The two features around 5 THz (167 cm⁻¹) and 7 THz (233 cm⁻¹) disappear upon transition to β (increasing s), while the baseline appears to grow

"noisier". Although the 7 THz is not presented in the experimental Figure 4.5, the disappearing band is indeed observed at a frequency of 180 cm⁻¹, which probably has the same origin as the 5 THz mode in Figure 4.8a. The feature around 1.5 THz (50 cm⁻¹) moves to lower frequencies, whereas the feature around 4 THz (133 cm⁻¹) moves to higher frequencies. The blue shift of the 4 THz mode fits with the hardening mode at 106 cm⁻¹ as observed in experiment (Figure 4.5), whereas the softening at 1.5 THz mode is not seen due to the spectral limitation in the experiment. However, the broadening of this mode at 1.5 THz does match very well with the broadening in Figure 4.7a. This feature can be assigned to the outer torsion φ as can be seen in Figure 4.8d. This in turn confirms our speculation for the modes at 50 cm⁻¹ and 55 cm⁻¹, which are assigned to be wagging vibrations of ring1 and ring2 groups, respectively.

The spectral features in Figure 4.8a are further decomposed, as s is a combination of both θ and φ , to show the θ and φ spectra (see Figures 4.8c and 4.8d), respectively. These two figures also show that the two disappearing features are mainly due to the inner torsion θ . This means that the torsion of the ring1 groups is closely connected with the structural phase transition and it appears as a band disappearing at frequencies of 180 cm⁻¹ and higher (233 cm⁻¹ in the simulated spectrum of Figure 4.8). This mode is fundamentally not allowed in the β phase regardless of polarizations during the measurements, as can be seen in Figure 4.3c and 4.3f. The increasing fluctuations in the baseline are due to the outer torsion φ , and appears intrinsic to the β structure instead of due to a lack of statistics, since this would have resulted in a similar baseline in the θ spectrum. It is likely due to the large range of rotations of the outer rings in the β phase. The features around 1.5 THz and 4 THz are due to both θ and φ , although the φ contribution diminishes going toward β for the 4 THz feature. This strengthens our argument in section 3.4, where we claimed that the mode at 106 cm⁻¹ has two contributions: ring1 contributes in the β phase and ring2 contributes in the α phase. The fading contribution of φ (ring2 groups) perfectly matches with our argument. We believe that the 1.5 THz mode is directly associated with the phase transition for two reasons: this feature has strong contributions of both θ and φ and is the only feature that shifts towards lower frequencies during the $\alpha \rightarrow \beta$ transition. Unfortunately, this mode softening could experimentally not be observed, but the accompanying broadening agrees well with the experimental spectra (see Figure 4.8b).

4.7 Conclusion and outlook

To conclude, characteristic changes in the Raman features are identified near the structural phase transition in 4-DBpFO single crystals and the importance of specific modes are highlighted with comparison to simulations. Temperature dependent Raman spectra provided unambiguous mode changes before and after phase transition. The mode assignment was completed by a systematic analysis of polarization dependent Raman spectra and simulated Raman spectra. Moreover, the unique line scan results presented not only two unique mode changes but also made it possible to experimentally identify the order parameter associated with the α to β transition. The results show that the wagging mode of ring2 groups at 55 cm⁻¹ and the torsion motion at 106 cm⁻¹ between ring1 and ring2 groups are directly related to the structural phase transition. Polarization-dependent Raman measurements together with the well-defined crystalline structure assisted the assignment of the Raman features and revealed their roles in the structural phase transition of 4-DBpFO single crystals. Moreover, the results of simulated polarization-dependent Raman spectra agreed well with the experimental data. The break-down analysis further supports the mode assignment at the frequencies below 200 cm⁻¹. Molecular dynamic simulations display the order parameter change across the phase transition which agrees well with the line scan Raman identifying the dynamic changes results, unravelling and the phase transition.

To the best of my knowledge, this study is the first investigation of the thermosalient phase transition of 4-DBpFO single crystals using in-situ Raman spectroscopy. It not only fills the knowledge gap in the area of thermosalient phase transition, but also leads to further investigations on the predicted ultrafast dynamics of the thermosalient phase transitions. For example, as predicted by simulations, strong THz laser pulses at around 1.5 THz is expected to non-thermally trigger the phase transition in 4-DBpFO single crystals (see also Chapter 6). This may grant us a brand-new, all-optical way to control the phase of a crystal. Our technique is also applicable to other salient materials whose phase boundary is controllable under certain conditions.



Chapter 5

Optical pump-probe study of the phase transition in 4-DBpFO single crystals

4-DBpFO exhibits an intriguing first-order thermosalient phase transition above room temperature, characterized by a drastic shape deformation caused by a sudden change in its crystal structure. In this chapter, we study the spectroscopic properties of this crystal both statically and dynamically. An ultrafast pump-probe technique was applied in the UV-vis range to study the transient transmission change in the 4-DBpFO single crystal across its phase transition temperature. The time-resolved transmission and polarization rotation changes reveal dynamics which can be interpreted as exciton formation and its decay. Transient polarization rotation measured at various temperatures and pump powers is shown to have signatures of the structural phase transition in the crystal.

5.1 Introduction

The concept of thermosalient crystals, also called jumping crystals, can be traced back to 1983 by M. C. Etter¹⁴. Up to now, about 30 documented compounds are reported as thermosalient materials^{25,115}, and most of them tend to disintegrate when the temperature is increased above the phase transition. Even though these fragile thermosalient crystals can still find uses in single stroke actuators, such as electrical fuses, robust and repeatable thermosalient behaviour is required for energy transducers, soft microrobots and organic electronics¹¹⁶.

4-DBpFO has been demonstrated to form a robust thermosalient crystal that can undergo a structural phase transition for hundreds of times without visible wear²². The phase transition is accompanied by the appearance of a phase boundary at one of the edges of the crystal, moving at a speed of about 10 mm/s³⁶. The phase transition associated with the thermosalient effect appears to be the fastest transition in molecular crystals¹¹⁶. To unravel such fast structural changes, ultrafast techniques are required. Optical pump-probe techniques have been widely used in exploring the ultrafast dynamics in solid-state materials. Most commonly studied topics are exciton^{117,118}, polaron^{119,120}, singlet fission^{121,122} dynamics and so on, performed on organic crystals such as rubrene¹¹⁷, tetracene¹¹⁸ etc. However, no such experiments have been done on the thermosalient phase transition in 4-DBpFO.

In this chapter, a comprehensive study was conducted using ultrafast optical pump-probe techniques. Time-resolved measurement has been carried out and disclosed the dynamics in both the α and β phases at picosecond time scales. The time-resolved transmission and polarization rotation changes indicate electronic excitation and its decay at various temperatures. The polarization rotation induced by temperature and pump power is demonstrated to be a signature of the structural phase transition.

5.2 Static spectroscopic study of 4-DBpFO

Before applying the pump-probe technique to study the dynamics of 4-DBpFO crystals, a static spectroscopic study was first conducted to determine the most efficient linear absorption wavelength.

The absorbance spectrum of the bulk 4-DBpFO single crystal (Figure 5.1), measured using a home-built setup (see Figure 2.5), shows that the absorption band of the

 α phase crystal extends from 366 nm to 468 nm with a peak at 415 nm. Based on this result, 400 nm was selected as the pump wavelength, corresponding to 96.2% of the maximum absorption at 415 nm. This choice was further motivated by the availability of a stable 800 nm fundamental output from the femtosecond laser used in the optical pump-probe experiment, from which 400 nm was generated via second harmonic generation. The selected pump wavelength thus falls within the absorption band of the crystal and is expected to efficiently drive the structural phase transition.

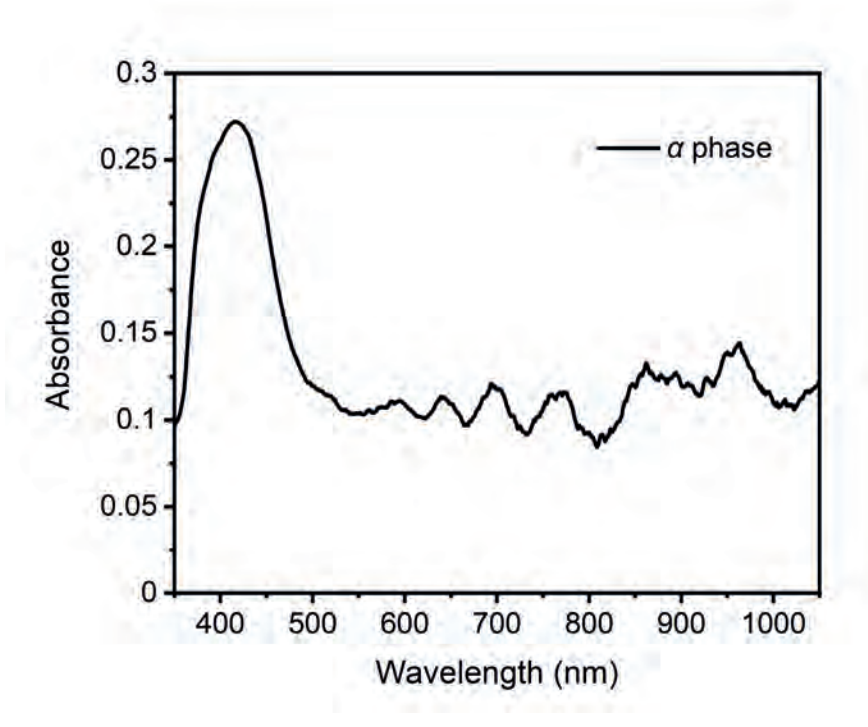


Figure 5.1. Absorbance spectrum of α phase 4-DBpFO single crystal. This is measured under ambient conditions (room temperature and atmospheric pressure). The effective absorption band is located between 366 nm and 468 nm.

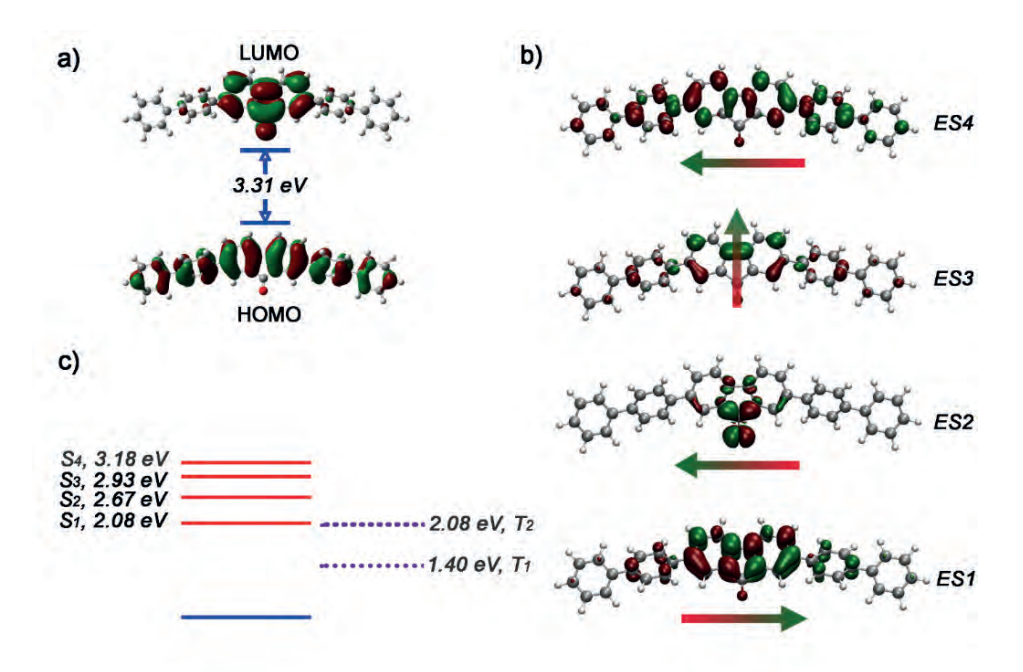


Figure 5.2. *DFT/TD-DFT calculations.*

(a) Shape of the HOMO and LUMO wavefunctions with the S_0 geometry as well as their energy levels of 4-DBpFO molecule. (b) Singlet excited states (ES) corresponding to S_1 , S_2 , S_3 and S_4 in c). The green color represents electron clouds whereas the red color represents holes. The arrows point out the transition dipole direction at corresponding excited states. (c) Electronic states of 4-DBpFO crystal123. The blue line indicates the ground state of the crystal lattice, the red lines indicate the excited singlet states of the system and the dotted purple lines indicate the excited triplet states.

In order to clarify the structure-property relationships involved in α phase 4-DBpFO crystals, theoretical calculations using the DFT/TD-DFT method were carried out in the E.01 version of Gaussian09¹²⁴ by Puxin Cheng, from Nankai University, China. The B3LYP functional and 6-31G++ basis was adopted to obtain the HOMO and LUMO wavefunction and the molecular dipole moment of 4-DBpFO S₀ state. B3LYP/6-31G+(d) basis was selected to calculate the transition density of states from S₀ to different excited states. The visualizations were displayed by VMD software¹²⁴. These calculations clearly pointed out the directions of permanent dipole and transition dipole in α phase 4-DBpFO crystals, providing guidelines for further analysis.

5.3 Time-resolved transmission changes

To investigate time-resolved transmission changes in 4-DBpFO crystals by optical pump-probe experiments, the pump wavelength was chosen at 400 nm (photon

energy is 3.1 eV), which falls in the linear absorbance spectrum (Figure 5.1) and can bring the electrons to an excited state (metastable state). Two different wavelengths, 800 nm and 400 nm, were used to probe the time traces of the transmission change with a time resolution of about 100 fs.

The experimental setup used for this set of data refers to Figure 2.7 in Chapter 2. The pump fluence was set as 1.4 mJ/cm² with a beam spot size of ~184 µm whereas the probe was focused with a spot size of ~46 μm but with two magnitude lower incoming power. The photo-induced transmitted intensity change is calibrated by dividing by the total transmission of the probe beam. The time zero is when pump and probe overlap in time. After the overlap, the sample system is in an excited state and a pump-induced transmission change is observed and registered as ΔT . After calibration by $\Delta T/T$, only the pump-induced effect can be seen. Upon the overlap of pump and probe pulses, the transmission change increases instantly from 0 to above 0.02. Transmission increases means absorption decreases. The electrons in the sample system absorb the incident pump photons and get excited to excited states, increasing the transmission of the probe beam.

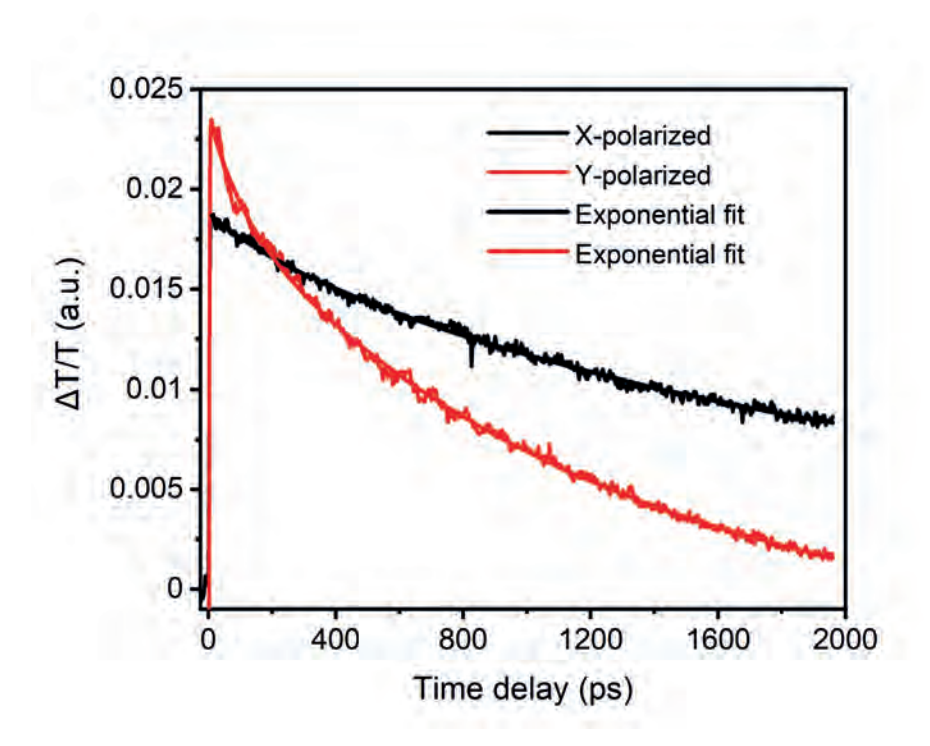


Figure 5.3. Transient transmission change under two different pump polarizations.

Figure 5.3 presents the time-resolved transmission change under X (black)- and Y (red)-polarized pump polarization. In 4-DBpFO, electrons are likely pumped up to S₄ state, as the photons have an energy of 3.10 eV which is close to the energy of S₄ (3.18 eV). When the pump beam is off, the excited electrons relax to the S₃ state and eventually relax back to the ground state. The probe registers this relaxation process and shows the dynamic change in the following 2000 ps (Figure 5.3). The spectra are well fitted with a two-exponential decay function:

$$y = y_0 + A_1 * e^{-\frac{x}{t_1}} + A_2 * e^{-\frac{x}{t_2}} (t_1 t_2).$$

The fitted spectra are presented as solid lines in the same color as the raw data. Two processes are resolved from the fitting: the fast decay process A1 and the slow decay process A2. The dynamics of these two processes as a function of pump power are discussed below.

The spectra in Figure 5.3 are obtained with identical experimental condition when both pump and probe wavelengths are at 400 nm. Comparing the amplitude of the transient transmission change, Y-polarized pump beam induces a stronger transmission change than the X-polarized pump. This could attribute to anisotropy of optical properties. The Y-polarization of the pump beam is collinear with the crystallographic a-axis (depicted in chapter 2 Figure 2.4), which is along the permanent dipole direction of the 4-DBpFO molecules. The incident pump beams interact with the permanent dipoles in the molecules, thus more electrons are excited in this polarization, leading to a higher transmission change at the overlap. This is also supported by the Gauss simulation in Figure 5.2b, where the S₃ state is dominated by the permanent dipole (along short molecular direction).

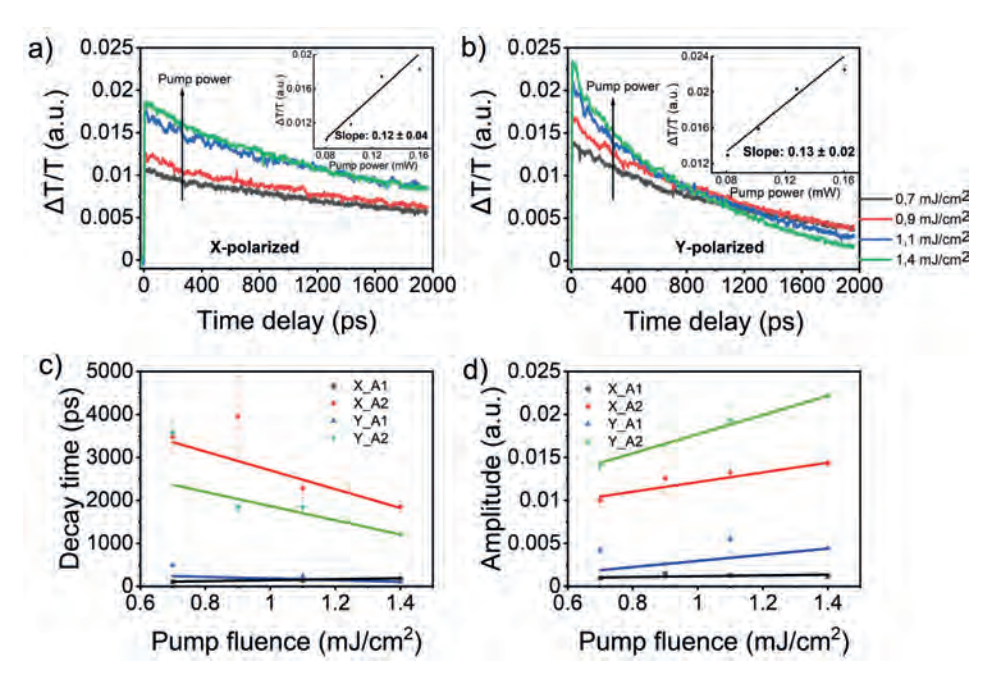


Figure 5.4. Transient transmission change with both pump and probe at the wavelength of 400 nm. Time-resolved transient transmission change under a) X- and b) Y-polarized pump polarization. The pump power is varied from 0.08 mW to 0.16 mW with a focused beam spot size \sim 220 μ m. The calculated fluence is indicated in the figures. The insets show a linear relation between the transmission change and pump power. c) Maximum transmission change as a function of pump power. The raw experimental data are extracted from a) and b) for X- (black) and Y-polarized (red) pump polarizations, and plotted as dots. The solid lines are the linear fitting results. d) The decay time of both polarizations extracted from the fitting results using the two-exponential decay function. The solid lines are a guide to the eye.

Figure 5.4 presents the time-resolved transmission spectra and the fitted results as a function of pump power. In both polarizations, the amplitude of transmission increases when the pump power increases, as can be seen in Figure 5.4a and 5.4b. The maximum transmission change shows a linear dependence of the incident pump power, as seen in the insets in Figure 5.4a and 5.4b. These changes remain within their laser damage threshold when the pump power is below 1.4 mJ/cm², as stated by the linear relation between $\Delta T/T$ and pump power as shown in the insets of Figure 5.4a and 5.4b.

The decay times of the A1 and A2 processes are plotted in Figure 5.4c. A1 decays on the time scale of a few hundred of picoseconds (100-500 ps); A2 decays on a few nanoseconds (1-4 ns). A1 seems to be independent of polarization, as it is approximately the same for both X and Y polarizations (Figure 5.4c). The A2-process, however, is faster in the Y-polarization (depicted in green in Figure 5.4c). This could be attributed to the intermolecular interactions in this direction (along permanent dipole direction) which is for the relaxation of the excited electrons.

Within the studied range of pump power, the decay time of the A1-process remains relatively stable around 200 ps, whereas the decay time of the A2-process decreases when the pump power increases. This means that the high pump power increased the probability of the relaxation of the A2-process. In the meantime, A2 dominates the relaxation process with a more than 5 times higher amplitude than A1, as can be seen from Figure 5.4d. With an increase of pump power, the amplitude of both A1 and A2 increases linearly.

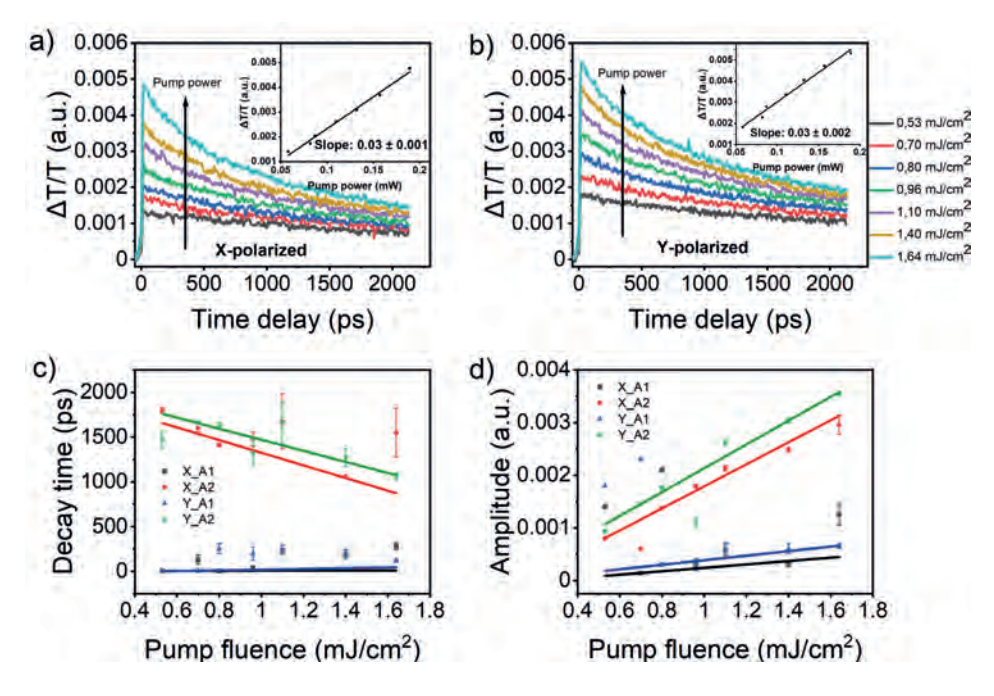


Figure 5.5. Transient transmission change with 400 nm pump and 800 nm probe. Time-resolved transient transmission change under X- (a) and Y-polarized (b) pump polarization. The pump power is varied from 0.06 mW to 0.19 mW with a focused beam spot size as ~220 μ m. The insets show the linear dependency of the maximum transmission change against pump power. The raw experimental data are plotted in dots while the fitting results are plotted as solid lines. c) The decay time of both polarizations extracted from the fitting results using a two-exponential decay function. The solid lines are linear fitting results. d) The fitted maximal transmission intensity for both polarizations using the above two-exponential decay function.

To reduce a possible excitation and/or heating effect from the 400 nm probe, we switched the probe wavelength to 800 nm and presented the transient transmission spectra in Figure 5.5. More data points as a function of pump power were obtained

within the time range of 2000 ps. The pump induced effects are similar under both Y- and X-polarizations. The Y-polarized pump induces stronger transmission change due to its coupling with permanent dipole. The incident pump power is below the damage threshold of 0.19 mW, as the maximum transmission shows a linear relation with the pump power (inset of Figure 5.5a and 5.5b).

However, the probed decay processes show significant differences. The fitted decay times for both A1 and A2 mechanisms are at least twice faster (fast decay time ranges from 4 ps to 200 ps; slow decays last for 600~1500 ps) than using 400 nm probe (Figure 5.4c). This could be attributed to the lower heating effect from the probe. Therefore, it is more suitable to use 800 nm as probe as it minimizes any possible linear absorption. In addition, with more data points, a relatively clearer tendency of the fitted amplitude of these two dynamics are plotted in Figure 5.5d. The as-fitted transmission amplitude gives a linear growth with respect to the incident pump powers, in accordance to the insets in Figure 5.5a and 5.5b. Meanwhile, the comparison between A1(fast decay) and A2 (slow decay) shows that the A2 decay is the dominant decay process that determines the time dependent traces of the transmission in Figure 4.5a and 4.5b.

5.4 Temperature dependent polarization rotation dynamics across the phase transition

As discussed in Chapter 3, the polarization rotation shows a temperature hysteresis behaviour upon the structural phase transition in 4-DBpFO single crystals, demonstrating that this polarization rotation is a good probe for the phase transition. In this section, the time evolution of the polarization rotation change is tracked and studied at various temperatures.

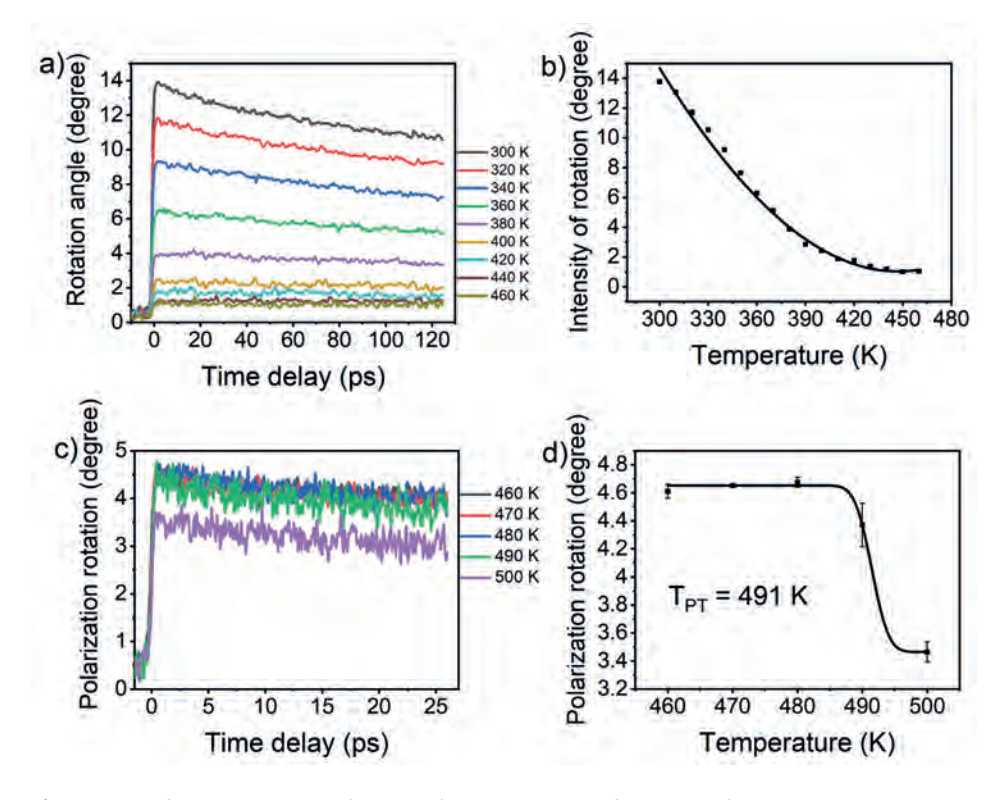


Figure 5.6. Polarization rotation change with 400 nm pump and 800 nm probe. The pump power stayed at ~0.8 mW (~7 mJ/cm²) for this set of experiments. The pump and probe polarizations were aligned to get maximum output. a) Time-resolved rotation change in a phase from 300 K to 460 K with a step of 10 K. The scanning range is about 120 ps. b) Extracted maximum rotations from Figure 5.6a. The Gaussian fitting indicates a saturation state starting from 420 K. c) Time-resolved probe polarization rotation change in the vicinity of the phase transition temperature. The scanning range is up to 25 ps. An abrupt decrease of the rotation intensity is captured when the structure of the 4-DBpFO crystal transitions from the α to the β phase. d) Extracted maximum rotation from Figure 5.6c. The solid line is a fitting curve by function 2.1. The errors are obtained by averaging three sets of experimental data.

In Figure 5.6a, the Y-axis shows the change in polarization rotation of the probe beam and it is largely altered due to the symmetry change upon the structural transition of 4-DBpFO single crystals. The phase transition temperature (491 K) for the whole crystal is determined upon the completion of the shape deformation of the crystal observed via a bluefox camera while the temperature of the sample system is modulated by a LakeShore temperature controller. Both pump and probe polarizations were set at the optimal direction which was pre-studied by a polarization scan. Before the phase transition occurs (temperature <491 K), the intensity of polarization rotation decreases with increasing temperature (Figure 5.6a). The maximal polarization rotation is extracted and plotted in Figure 5.6b. The data is well fitted with a Gaussian function, indicating an

exponential dependency of the polarization rotation against temperature. It is important to note that at high temperatures (~420 K), the decrease in the polarization rotation slowed down significantly and reached a saturation level right before the phase transition temperature. This suggests an intermediate state of the crystal when it is about to go through a structural phase transition.

Figure 5.6c and 5.6d present a clear signal of the polarization rotation change across the phase transition temperature. First of all, the polarization rotation stabilizes at the high temperature state of the α phase (intermediate state), as observed in Figure 5.6b. With further heating (up to 500 K), a sudden decrease of the rotation value occurred (Figure 5.6c) together with the completion of the transition from the α phase to the β phase. This change is attributed to the rapid structural change of the crystal symmetry as this significantly differs from the saturation behaviour observed in the α phase at high temperatures. This abrupt rotation change is the same as the static polarization rotation change shown in Chapter 3, benchmarking the structural transition from α to β . To validate the firstorder nature of this structural phase transition, the maximum rotation change is extracted and plotted in Figure 5.6d. The raw data points are fitted very well with an error function (equation 2.1) which emphasizes a large rotation change between the two phases.

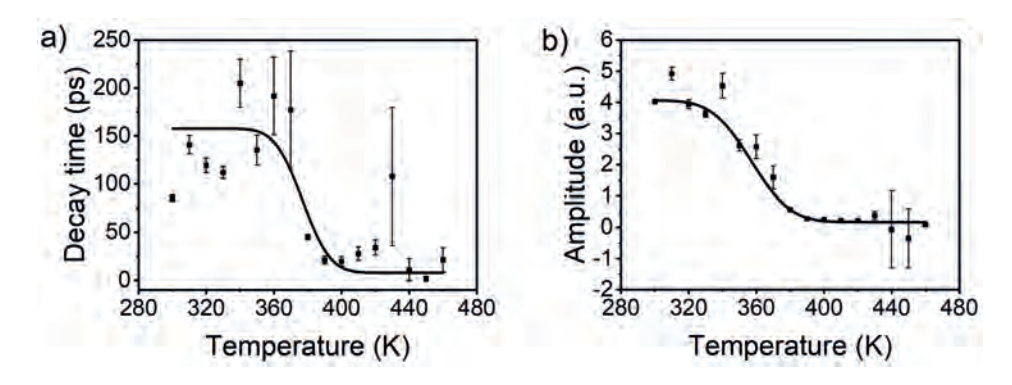


Figure 5.7. Decay time and the amplitude fitted from Figure 5.6a. Expdec1 function was used to fit the data in Figure 5.6a and the resolved decay time and its amplitude are plotted here. The fitted decay time is 150.00 ± 24.41 ps and 7.83± 15.43 ps before and after transition. The fitted amplitude is 3.90 ± 0.12 and 0.17 ± 0.03 before and after transition.

Different from the transmission change, the time-resolved rotation changes are well fitted with Expdec1 function $(y = y_o + A_1 * e^{-\frac{x}{t_1}})$, indicating a singular mechanism that influences the polarization rotation change after optical pump. Figure 5.7 presents the fitted results from Figure 5.6a. The decay time and amplitude of the mechanism can be fitted with the error function, indicating the first-order phase

transition. After fitting, the decay time shows a significant change, starting at a temperature of 352 ± 4 K and finishing at 402 ± 4 K; the change on the rotation starts at a temperature of 321 ± 2 K and finishes at 393 ± 2 K. These demonstrate microscopic changes of the mechanism before the macroscopic shape deformation occurs. However, the visible shape deformation that was observed via the camera occurred at the temperature of 491 K. The large onset temperature difference (352 K for decay time and 321 K for amplitude change) may be attributed to the local structural change upon heating by the optical pump whereas the macroscopic shape change awaits for the whole crystal to be heated above the transition temperature. This is in agreement with the nucleation-and-growth mechanism demonstrated by molecular dynamic simulations²², where a nucleation point was first identified after which the transformation spreads through the rest of the crystal in all three directions.

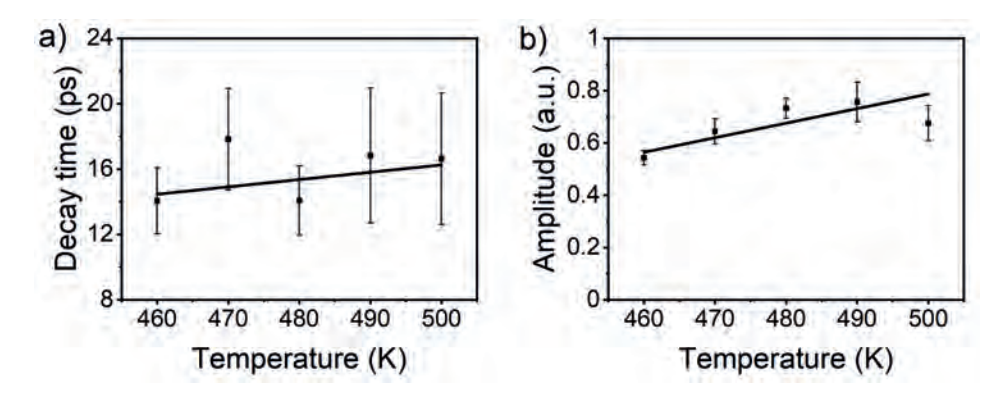


Figure 5.8. Decay time and the amplitude fitted from Figure 5.6c. Expdec1 function was used to fit the data in Figure 5.6c and the resolved decay time and its amplitude are plotted here. The decay time and amplitude are fitted with linear functions. The slopes are 0.045 ± 0.063 and 0.006 ± 0.002 , respectively.

The decay time and rotation extracted from Figure 5.6c show a steady linear relation as a function of temperature. The intensity of the decay time is comparable to that of the β phase in Figure 5.7a above a temperature of 402 K. Likewise, the intensity of Figure 5.8b is also comparable to that in Figure 5.7b above a temperature of 393 K. The similarities indicate that these two sets of data are in the same, β , phase of the crystal. The slopes of both decay time and amplitude change are close to zero, revealing a stable state in β phase.

To conclude, in the temperature dependent rotation change experiment, the intensity of polarization rotation change in 4-DBpFO typically decays in the time scale of 92 \pm 10 ps in α phase and 8 \pm 6 ps in β phase. The decay time changes significantly once the structural phase transition takes place (as discussed in

Figure 5.7a). The decay time and amplitude stabilize after the transition completed (as discussed in Figure 5.7b and Figure 5.8). There is a large temperature difference (~150 K) between the microscopic (352 K in Figure 5.7a) and the macroscopic transition (491 K in Figure 5.6c and 5.6d). This is attributed to the energy difference between a local, pump induced, or complete transition. When the whole crystal went through the phase transition, a clear polarization rotation value change can be detected, as shown in Figure 5.6c and 5.6d. This is a proof that the transition has been completed over the whole crystal.

5.5 Pump power dependent polarization rotation change

In order to drive the thermosalient phase transition in a contactless way, optical pump probe experiments were performed with strategically increasing pump power at three tempertures, 400 K, 450 K and 500 K. The pump wavelength is fixed at 400 nm to ensure efficient linear absorption and the probe wavelength is set at 800 nm. Figure 5.9 presents the ultrafast rotational change within 25 ps.

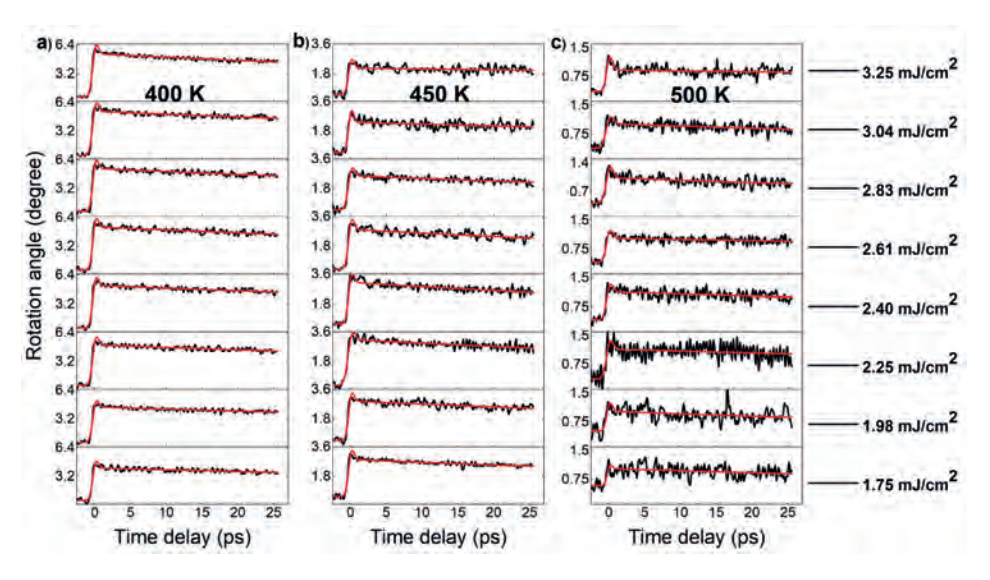


Figure 5.9. Time-resolved rotation change as a function of pump powers. Ultrafast polarization rotation change of 800 nm probe induced by optical pump pulses (400 nm) at a temperature of a) 400 K, b) 450 K, and c) 500 K. For each temperature, the pump ramped up from 1.75 mJ/cm 2 to 3.25 mJ/cm 2 . The solid red curves are the fitted results using the function125 of $y=y_o+$ $A*e^{rac{-x^2}{4w^2}}+B*e^{\left(rac{w^2}{t^2}-rac{x}{t}
ight)*(1-\mathrm{erf}(rac{w}{t}-rac{x}{2w}))}.$

At 400 K, the rotation angle is as large as 4.5° at the minimum applied pump fluence, 1.75 mJ/cm². With the increase of pump fluence, the rotation angle decreases. At a higher temperature, 450 K, the rotation angle decreased from 4° to 2° when the pump fluence is increased from 1.75 mJ/cm² to 3.25 mJ/cm². At 500 K, the rotation angle showed a similar trend as it reduced from 1.5° to 0.75° with the increase of pump fluence. The maximum rotation angle of each spectrum is extracted and plotted against pump power in Figure 5.10. Comparing these three temperatures, the rotation angle decreases with an increase of temperature. Besides, the noise level is increased at higher temperatures, probably related to the increase of fluctuations near the phase transition.

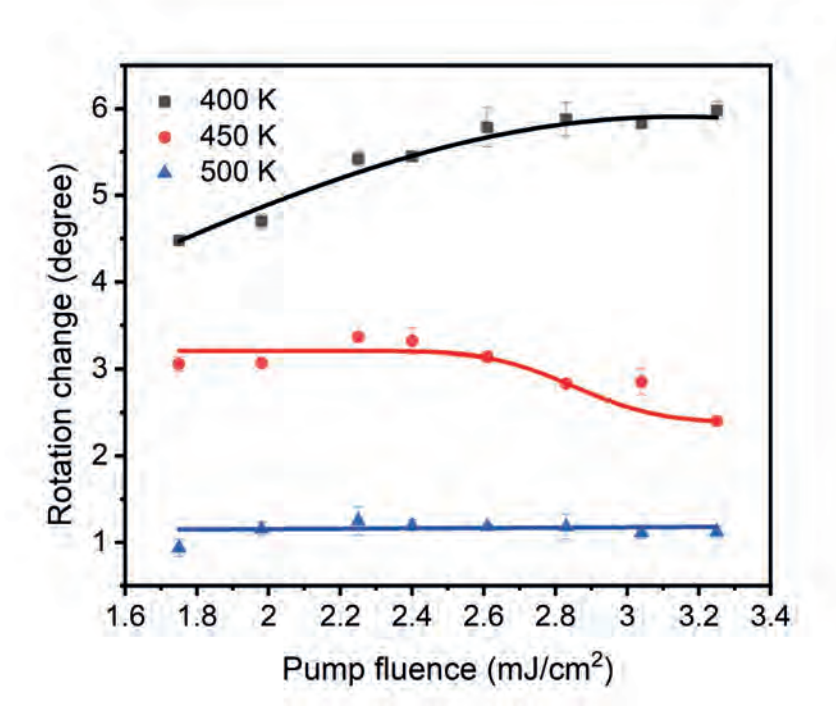


Figure 5.10. Extracted maximum rotation change as a function of pump fluence. The raw experimental data are extracted from Figure 5.9 and plotted with error bar. The rotation changes are fitted with GaussAmp function $y=y_o+A*e^{\frac{-(x-x_c)^2}{2w^2}}$, error function from equation 2.1 and linear function for 400 K, 450 K and 500 K, respectively.

In Figure 5.10, the rotation change with increasing pump power resembles the static rotational change in the α phase. As shown in Chapter 3, the linear rotation first increases with an increase in temperature, then it reaches a saturation point and stabilizes until the occurrence of the phase transition. This is also achieved by

optical pumping as can be seen in Figure 5.6. At 400 K, the rotation grows exponentially with an increase of pump power. This is still in the α phase since the system energy is too low to overcome the phase transition barrier. When the temperature is increased to the critical temperature, the sample will reach a metastable state and the rotation value will stabilize at the saturation point. When the system temperature is increased to 450 K, the rotation value started at an average value of 3.2 \pm 0.1 degree, then it decreased to 2.4 \pm 0.1. This change is fitted with a step function as can be seen from the red solid line in Figure 5.10. This is an indication of a transition from the α to the β phase. With a fixed temperature of the sample, increasing the pump power triggered the structural phase transition in 4-DBpFO. The onset pump power that was needed for driving the structural transition is fitted to be 3.1 \pm 0.3 mJ/cm². To verify the rotational change at different phases, we increased the temperature to 500 K and corresponding pump powers were applied on the sample. It showed a rather stable rotation value with a slope of 0.04 degree/(mJ/cm²) after a linear fitting, as shown with blue dots and solid fitted line in Figure 5.10.

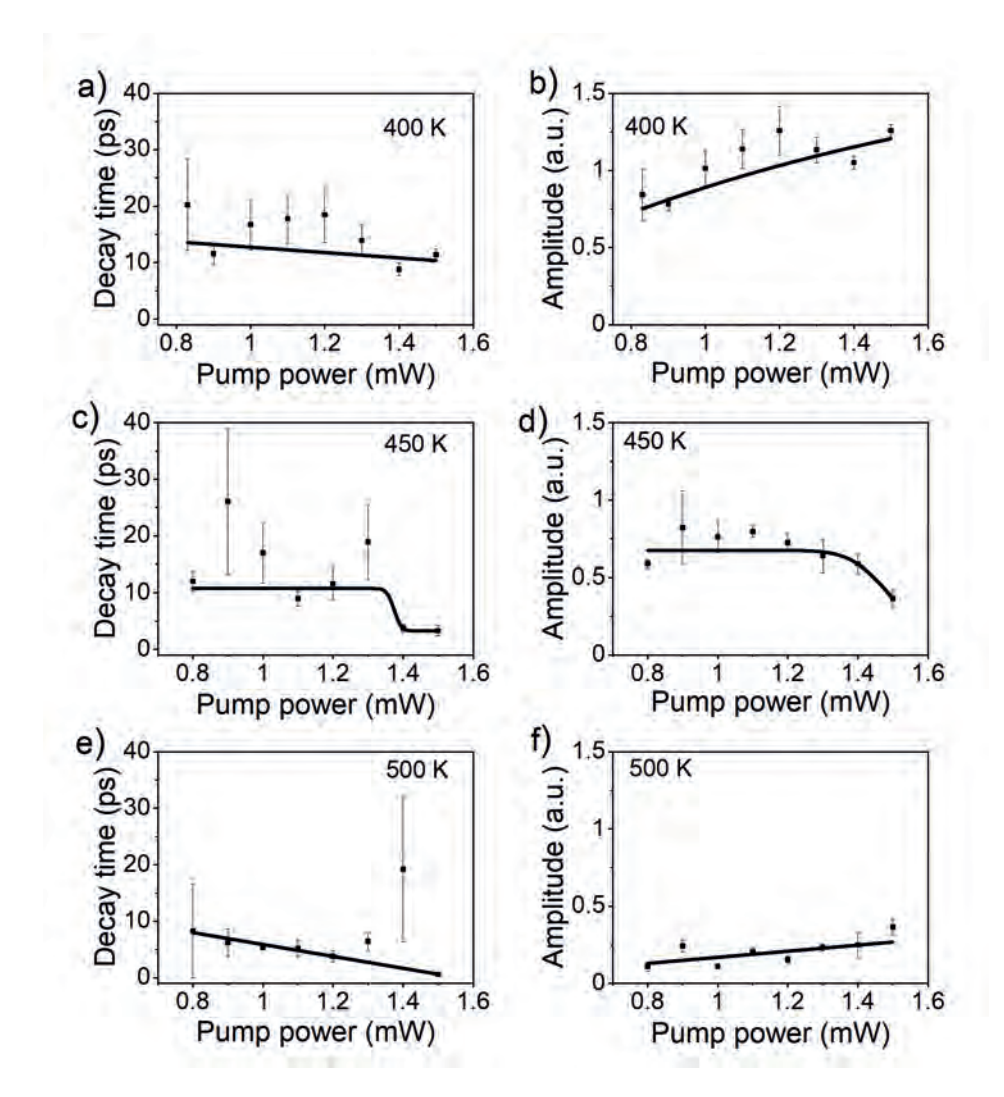


Figure 5.11. Decay time and amplitude extracted from fitting the spectra with exponential Expdec1 decay function.

The resulted decay time and amplitude of the mechanism are plotted against pump power. a) and b) are corresponding to 5.9a (400 K); c) and d) are corresponding to 5.9b (450 K); e) and f) are corresponding to 5.9c (500 K).

The time-resolved rotation change in Figure 5.9 has also been fitted with Expdec1 function and the resulted decay time and amplitude are plotted in Figure 5.11. The decay time fluctuates in a reasonable error range with an average of 8.0 ps at 400 K. At 450 K, the decay time started with the average value at around 10.8 ps then it went down to an average value of 7.5 ps at the pump power above 1.4 mW. At 500 K, despite the large error at 1.4 mW, the intensity of decay time stabilizes at around 5 ps, indicating a new state (β phase). These changes across phase

transition also match with the analysis in Figure 5.7 and 5.8. Therefore, the structural phase transition occurs, according to the fitting, at the pump power of 1.34 ± 0.02 mW (fitting result of Figure 5.11c) when the sample was kept at 450 K by the heater. The amplitude change (Figure 5.11b, d and f) showed similar trends at different temperatures. At 400 K, the intensity of the amplitude is at around 1 degree and at 500 K it is around 0.2 degree. The transition happened when the sample temperature was at 450 K. The data at 450 K was also fitted by equation 2.1. Although there is relatively large fitting error due to lack of data above 1.5 mW, the onset pump power for the structural phase transition is about 1.31 \pm 2.5 mW (fitting result of Figure 5.11d), close to the onset pump power of 1.34 \pm 0.02 mW derived from decay time fitting.

5.6 Conclusion and outlook

The time-resolved transmission and polarization rotation change of 4-DBpFO have been studied at temperatures before and after the phase transition. The transmission change suggests two mechanisms, a fast and a slow decay, described by an amplitude A1 and A2 and relaxation times of a few hundreds of picoseconds and a few nanoseconds, respectively. These two exponential decays after optical excitation reflects the dynamics of electron charges in excited states.

Unlike the transmission change, the polarization rotation change marks the structural phase transition in 4-DBpFO crystals and it is dominated by a single mechanism. The rotation change first increases in the α phase and reaches a saturation state when the temperature is near the critical temperature. At the transition, there is a significant change of the rotation value due to the sheared orientation of the crystal. The underlying mechanism is analysed by fitting its decay time and amplitude. Both the decay time and amplitude give a step-like behaviour at the transition. The onset temperature obtained by fitting the polarization rotation and the decay time has a relatively large difference. This is explained by a combination of local heating and a nucleation-andgrowth mechanism.



Chapter 6

THz pump-optical probe study of the thermosalient phase transition in 4-DBpFO single crystals

Smart materials like thermosalient crystals may find applications as actuators, medical implants and thermoswitches³. However, it is of great interest to coherently control the salient behaviour to apply these materials in practice. Raman experiments in thermosalient 4-DBpFO have revealed low frequency phonon modes that are closely related to this structural phase transition. In this chapter, we attempt to use strong THz pulses to trigger these phonon modes resonantly and achieve optical control of the structural phase transition in the 4-DBpFO. Our approach combines theoretical calculations and pump-probe experiments. The results are compared and discussed to provide ideas for further studies.

Parts of this chapter are adapted from: S. Ghasemlou, X. Li, et al. "Identifying and controlling the order parameter for ultrafast photoinduced phase transitions in thermosalient materials" Proc. Natl. Acad. Sci. U.S.A. 121 (46) e2408366121.

6.1 Introduction

The terahertz (THz) frequency falls in between the infrared and microwave region of the electromagnetic spectrum (0.1 THz to 10 THz) and it shares some properties with each of these³². There is an astonishing amount of organic materials which can be used for THz generation. The list of widely used compounds includes DAST^{55,58}, DSTMS⁵⁴, OH1⁵⁴ and HMO-TMS^{59,60}. As each of these materials only cover a part of the THz spectrum of interest, there is an ongoing search for new materials that can efficiently convert higher frequency light into the THz-frequency range. One recently discovered example is the fluorenone derivative DPFO. As reported, DPFO emits narrowband THz at a frequency around 1.5 THz, with a THz field strength comparable to that of the classic OH1 crystal. In 4-DBpFO, that shares similar molecular building blocks, a Raman active mode at 1.5 THz is also observed (see Chapter 3, the 50 and 55 cm⁻¹ modes), which appeared to be closely related to its thermosalient structural phase transition.

These observations motivated molecular dynamics simulations that demonstrated that the thermosalient phase transition in 4-DBpFO can be triggered by a strong 1.5 THz pulse¹¹⁴. We employed strong THz pulses from a home-build set up to resonantly pump this phonon mode while the structural phase transition was probed by tracing the THz-induced polarization rotation change of an optical probe beam, using the birefringence change (see Chapter 2) as a signature of the phase transition. However, after detailed analysis, it is shown that the phase transition could not be induced by the THz pulses. Nevertheless, THz induced SHG (TSHG) was observed and turned out to be related to the structural phase transition in 4-DBpFO. The TSHG is not only interesting as it is observed in centrosymmetric crystals, but also for future studies where TSHG can be utilized as a probe parameter to characterize structural phase transitions. Using the stronger THz pulses of the Nijmegen free electron laser FLARE we were indeed able to induce the thermosalient phase transition in 4-DBpFO, however, unfortunately the time resolution of the experiment did not allow to follow this transition in real time.

6.2 Simulation of photoinduced phase transition in 4-**DBpFO**

Photoinduced phase transitions allow ultrafast nonequilibrium phenomena such as THz-induced superconductivity^{126,127}, photoinduced metal-insulator transitions¹²⁸, ultrafast melting of charge and orbital order¹²⁹, optical and THz switching of magnetic states 130-133, and light-induced hexatic state in a layered material 134.

In chapter 4, we have identified the frequencies associated with the order parameter of the structural phase transition in 4-DBpFO. Here, we aim to trigger this phase transition by exciting the responsible vibration at its corresponding frequency. The simulations were performed in the group of H. Cuppen⁶¹. In classical simulations with point charges, vibrations can be excited by applying an oscillating electric field which leads to an additional force on the atoms. Dipole-allowed vibrations respond to the electric field directly whereas symmetrical vibrations can be triggered by the electric field gradient.

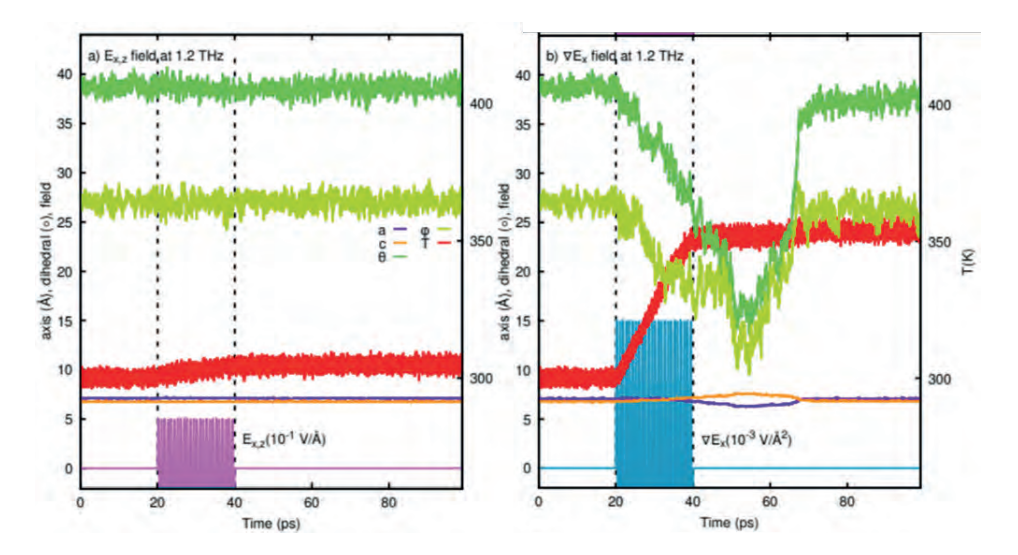


Figure 6.1. Simulation of triggering the phase transition by an a) oscillating electric field and b) oscillating electric field gradient. a) For the electric field, no energy is adsorbed and no phase change can be observed. b) For the field gradient, the temperature (in red) increases and simultaneously the system transforms to β , measured by a, c, θ , and φ . After the pulse ends, the system relaxes back to the initial a from.

Figure 6.1a and b show the attempts of pumping the 1.0–1.5 THz mode by applying an oscillating electric field and electric field gradient at 1.2 THz, respectively. The pulses are plotted in pink and blue, respectively and the temperature of the system in red. The structural changes due to the pulse can be followed in terms of crystal axis lengths a (purple) and c (orange) and the two dihedral angles θ and ϕ (dark and light green). The electric-field pulse appears not to lead to the adsorption of energy, as indicated by the minimal temperature increase, nor to any structural changes. A clear induced phase transition from the α to the β phase can be observed, if an oscillating electric-field-gradient pulse is applied instead, coinciding with a temperature increase and sudden changes in a, c, θ and ϕ . This indicates that the 1.0–1.5 THz feature is Raman and not IR active, in excellent agreement with the observation of this mode in the experimental Raman spectra

(see Figure 4.9 in Chapter 4). The changes immediately follow the temperature increase with no additional delay, indicating that the phase transition does not require the transfer of thermal energy into other vibrational modes except for this low frequency mode. It is important to note that these simulations were performed in the isoenthalphic-isobaric ensemble (NPH), meaning the system was not additionally cooled. However, it is clear from Figure 6.1 that the maximum temperature (350 K) remained well below the phase transition temperature of roughly 430 K, confirming that the phase transition was purely triggered by the induced vibrations and not by temperature. As soon as the pulse ends, the system relaxes back within 10 ps to the stable α form, still at 350 K. For the simulations in Figure 6.1b, the electric field gradient was applied along the x axis. Gradients along y and z did not result in any transition⁶¹.

In conclusion, when a THz pulse with the proper intensity and resonant frequency is applied, the phase transition occurs instantaneously. The phase transition observed in Figure 6.1 is induced by directly triggering the responsible lowfrequency mode and is accompanied by energy absorption. There is no need for any redistribution of energy in this process. Once the pulse ends the system reverts within 10 ps back to its initial α form.

In the simulations, there is obviously no limitation on the electric field strength that can be applied on the sample system. Experimentally, strong field gradients can be generated by single-cycle THz generation via optical rectification, though the achievable strength is limited by material parameters¹³⁵. In the following sections, two different approaches (using FLARE and table-top THz pulses) are presented with the aim to trigger the structural phase transition in the THz frequency.

6.3 THz pump driven phase transition using FLARE

A polarizing microscope was built with the FLARE free electron laser as a pumping source to explore resonant pumping conditions of the structural phase transition in 4-DBpFO single crystals. The shape deformation from a square shape to a diamond shape, representing the structural phase transition from an orthorhombic to a monoclinic crystal structure, was first observed via a microscope, simply by heating using a temperature controller. At the temperature of 451 K, two phase boundaries originated from the parallel sides of the square shape crystal, propagating towards each other and thus changing the crystal into a rhombic shape³⁶.

In order to drive the phase transition in 4-DBpFO by pumping with a FLARE beam at a low frequency, different repetition rates of the micro pulses (20 MHz and 3 GHz) were employed while the macro pulse was constantly operating at 5 Hz. However, no effect was observed at 20 MHz. Therefore, in the following experiments, the FLARE beam was operating at 3 GHz repetition rate for the micro pulses.

When half of the FLARE beam power (50 mW, $1.0 * 10^4 (\text{V/cm})$) was used as pump, one of the phase boundaries was moving forward and backward within a very small distance (~20 μm). When the full power FLARE beam

 $(100 \text{mW}, 4.0 * 10^4 \text{ (V/cm)})$ was incident on the crystal, both phase boundaries started to propagate towards each other and quickly relaxed back (Figure 6.2). Notably, this forward-and-backward movement occurred with irregular temporal breaks, which could be related to power fluctuations of FLARE or temperature fluctuations from the temperature controller. Therefore, the distance of this movement is highly dependent on the pumping power from FLARE and is controllable by manipulating the pumping power and the temperature.

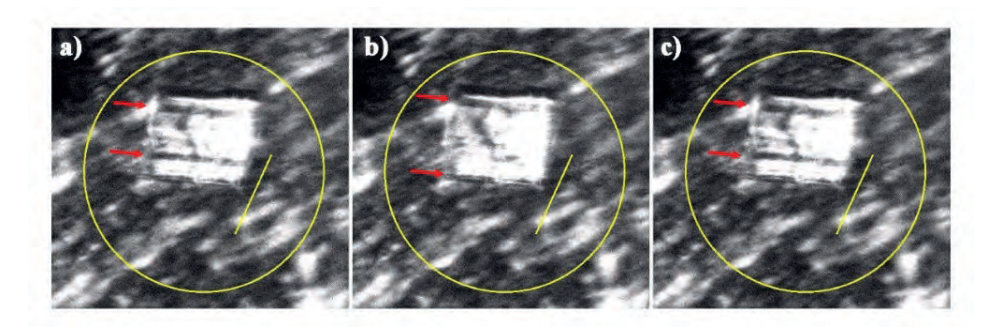


Figure 6.2. 4-DBpFO single crystal transforming via two parallel phase boundaries. a) With exposure to FLARE b) Without exposure to FLARE and c) With exposure to FLARE again. The yellow circle and yellow straight line mark the location and the scale of the crystal, respectively. The scale of the yellow line is about 110 μm, which is equivalent to the length of the square shape crystal. While exposed to the FLARE beam, this crystal remained its position but the phase boundaries move back and forth. The red arrows point out the position of the two parallel phase boundaries.

The square shaped sample was on a diamond substrate and the temperature of the system was fixed at 447.5 \pm 0.5 K, 1 K below the phase transition. Due to the birefringence effect, the crystal is seen as a bright square through crossed polarizer and analyzer. Upon the phase transition, two dark lines (phase boundaries) from both the bottom and top side of the crystal are seen via the polarizing microscope, as marked with red arrows in Figure 6.2. In the first image, these two phase boundaries were close to each other, whereas in the second image the bottom boundary completely relaxed back and the top boundary relaxed back to the edge

of the crystal. In the third image these two boundaries propagated towards each other again.

During the experiment, the jumping behavior of 4-DBpFO crystal was also seen when exposed to the FLARE beam. Unfortunately, the jumping was too fast to be captured by the camera, whose temporal resolution is 27 µs. After jumping, the crystal ended up in a standing position, in which only the side face of the crystal was in touch with the diamond substrate (Figure 6.3). A fast and reversible phase transition was also seen when the crystal was exposed to FLARE beam in this position.

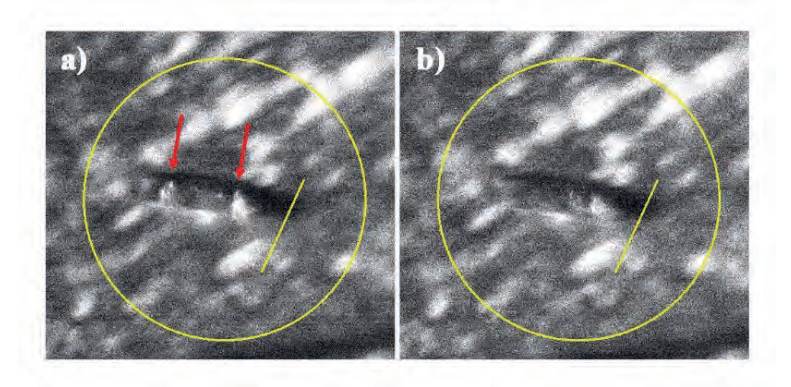


Figure 6.3. Standing a-phase 4-DBpFO crystal transforming via parallel phase boundaries upon exposing to FLARE. This is the same single crystal as shown in Figure 6.2. The yellow circle and yellow straight line have the same scale as in Figure 6.2. The red arrow points to the two parallel phase boundaries, which disappeared in the second image.

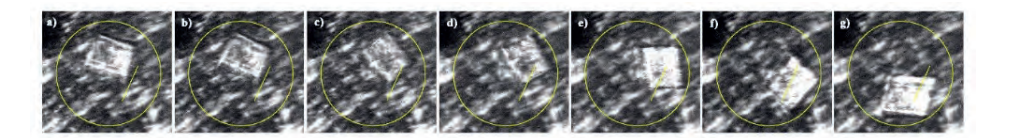


Figure 6.4. The rotation of α -phase 4-DBpFO single crystal induced by FLARE. Clockwise rotation with respect to the yellow line marker is observed upon pumping by FLARE. The presented rotation is about 180° and it is continuous when the FLARE is on. The birefringence change is seen from the different brightness of the sample. The intensity change (bright-dark-bright) indicates the birefringence change during rotation.

Moreover, a continuous rotation (~180°) of a 4-DBpFO crystal was also observed upon pumping with FLARE (Figure 6.4). The rotation is possibly due to the different strain between two layers of this specific crystal. In the meantime, the birefringence change was observed through the polarizing microscope during the rotation, consistent with previous optical experiments.

Eventually, the directions of the in-plane optical axes in the middle of the crystal became permanently changed after heating the crystal 10 °C above the phase transition temperature³⁶.

In summary, driving the structural phase transition in 4-DBpFO single crystal was achieved by applying a FLARE beam at the frequency of 1.4 THz and a power of 100 mW, and this is captured by a home-built microscope setup, as shown in Figure 6.2. Unfortunately, due to the mismatch between the time scale of the dynamics of the phase transition (ps) and the time structure of the FLARE beam (3 GHz for picosecond micro pulses / 5 Hz for microsecond macro pulses), time-resolved pump-probe results could not be obtained to disclose the dynamics of the FLARE induced structural phase transition in 4-DBpFO crystals.

6.4 Time resolved THz pump-optical probe experiments

To study the dynamics during the THz resonant driven structural phase transition in 4-DBpFO crystals, we employed a table-top THz field pump-optical probe setup. Figure 2.10 shows a schematic picture of our THz pump-optical probe set up.

For the THz pump-optical probe experiments, we employed strong THz pulses as the pump, which cover the spectral range from 0 to 2 THz, with a FWHM of 1.0 THz (Figure 2.9). The intense, nearly single-cycle THz pulses are generated by tiltedpulse-front optical rectification in LiNbO₃^{136,137}. The peak amplitude of the THz electric field is up to 1 MV/cm centered around the frequency of 0.8 THz. The phase transition was probed by measuring the birefringence of a probe beam at 800 nm and zero-time delay as a function of temperature in the absence/presence of the THz pulse.

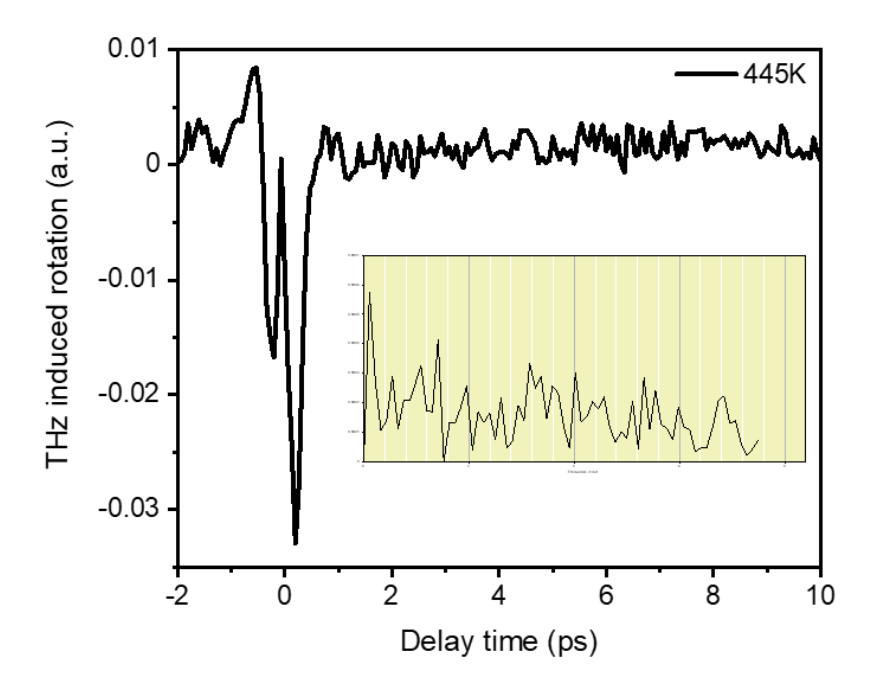


Figure 6.5. Time-resolved probe polarization rotation changes in α phase 4-DBpFO single crystal.

Figure 6.5 shows a typical result of THz-induced probe polarization rotation in α phase 4-DBpFO at 455 K (3 K below the phase transition). Upon pumping by the THz pulse, a strong polarization rotation is induced at the overlap (time zero). The shape of the signal at the overlap resembles the squared shape of the THz pump pulses (see Figure 2.9a), indicating a quadratic THz response from the 4-DBpFO crystal. A frequency spectrum of the time domain signal after the overlap obtained with fast Fourier transformation shows that no lattice vibrations were excited, as shown in the inset of Figure 6.5.

6.4.1 Pump polarization dependence

The dependence of the polarization rotational signal on the polarization of the THz pulses was performed in order to find the optimal pump incident polarization. The dependence is different in different phases of the 4-DBpFO. Figure 6.6 presented 3 states of the crystal: a) and d) correspond to the α phase; b) and e) correspond to the $\alpha \rightarrow \beta$ transition state; and c) and f) correspond to the β phase.

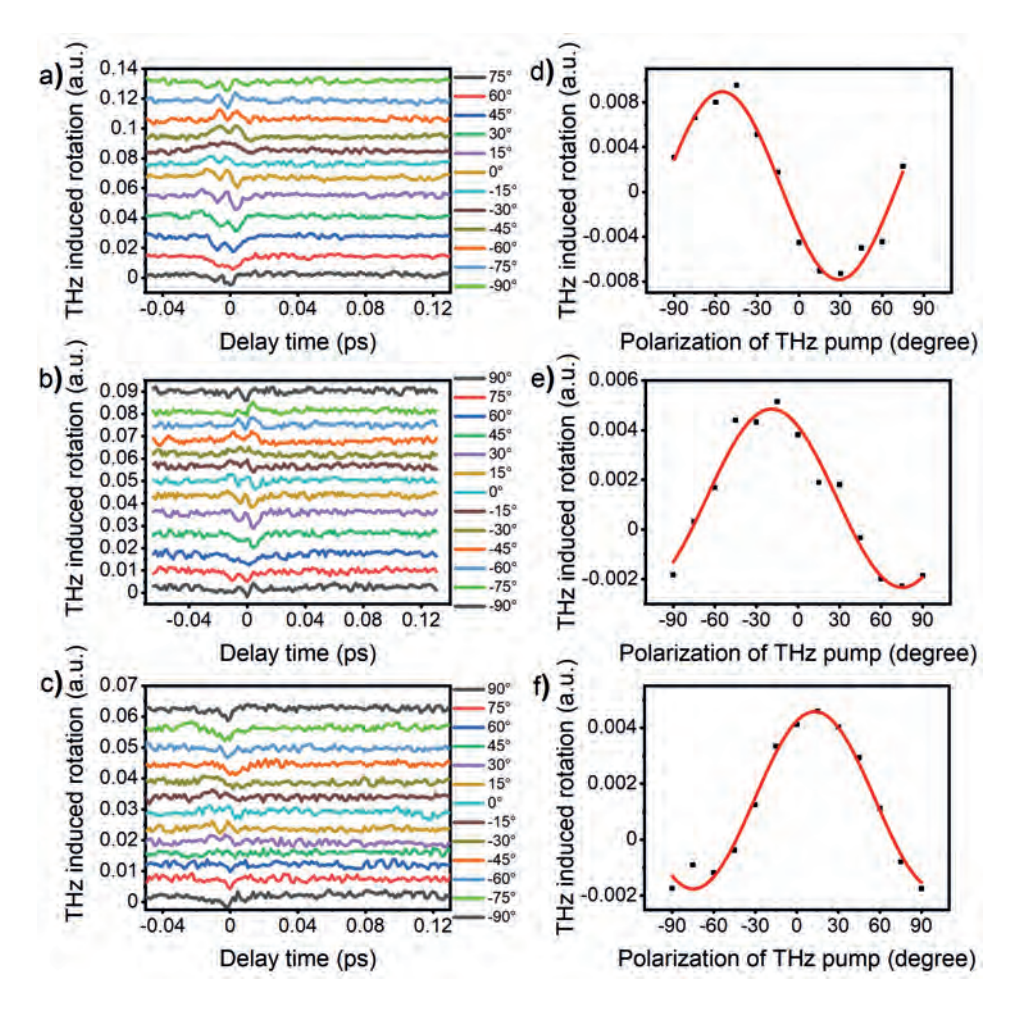


Figure 6.6. The THz induced polarization rotation dependence on the THz pump polarization in different phases of the 4-DBpFO single crystal.

a) Time-resolved dynamic measurements in the α phase of 4-DBpFO under different pump incident polarizations. b) Time-resolved dynamic measurements in transition state of 4-DBpFO single crystal under different pump incident polarizations. c) Time-resolved dynamic measurements in β phase 4-DBpFO under different pump incident polarizations. The polarization of the THz pump was rotated from -90° to 90° in steps of 15°. d) Extracted maximum rotation value at time zero as a function of pump polarization, corresponding to the α phase. e) Extracted maximum rotation value at time zero as a function of pump polarization, corresponding to transition state. f) Extracted maximum rotation value at time zero as a function of pump polarization, corresponding to the β phase.

As can be seen from the dynamic measurements, the THz induced rotation changes dramatically at zero time delay, where the THz pump and 800 nm probe overlap. In the time range of several picoseconds, we did not observe significant dynamics. Therefore, we extracted the rotation change at time zero and plotted this accordingly as a function of THz pump polarization. As can be seen in Figure 6.6c

and 6.6f, the rotation value reaches its maximum at around 20° of the incident THz pump polarization in the β phase, whereas this polarization produces near zero rotational change in the transition state (Figure 6.6b and 6.6e).

6.4.2 Time-resolved THz induced polarization rotation

To study the relation of the THz induced polarization rotation with the thermosalient phase transition in 4-DBpFO, temperature dependent measurements were performed. The sample system is first heated from 445 K to 465 K and then cooled down to 445 K again, with a heating/cooling rate of 5 K/min. As there is no response after the overlap, we mainly focused on analysing the signal at the overlap.

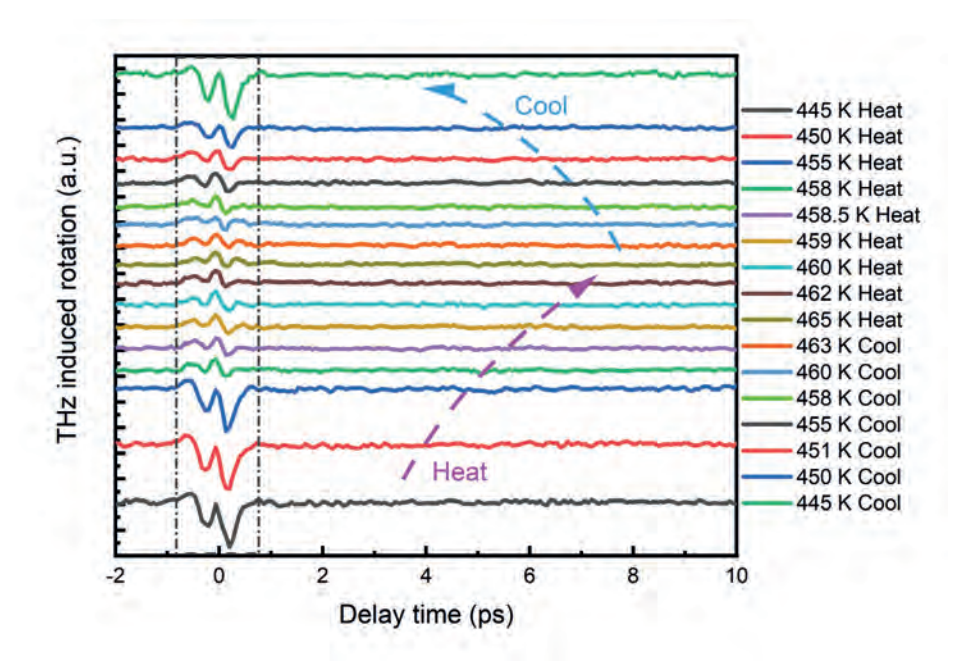


Figure 6.7. Time-resolved THz induced probe polarization rotation changes across the thermosalient phase transition in 4-DBpFO.

The studied temperature range was focused around the phase transition temperature, from 445 K to 465 K. The intensity of the rotation decreases upon heating and it increases back to its original value after cooling back to 455 K.

The time-resolved spectrum at time zero shows completely different shape between α phase (455 K) and β phase (458 K), as can be seen in Figure 6.7. Upon pumping by THz pulses, the output polarization rotates and the rotation value changes with temperature. At time zero, the THz induced rotation starts with a negative maximum value (445 K), when the temperature is increased, the intensity of this maximum decreases and reaches a minimum at the temperature of 458 K, where the crystal is transformed into the β phase. The intensity of the THz induced rotation remains stable in the β phase (458 K – 465 K – 455 K). When the crystal is cooled down, the sample transitions back from the β phase to the α phase, the absolute intensity of the rotation increases again and recovers back to the original value. By blocking the THz beam, we can measure the static birefringence in the same set up. The results are plotted in Figure 6.8 and show that both static and THz induce birefringence show a hysteresis loop around the thermosalient phase transition.

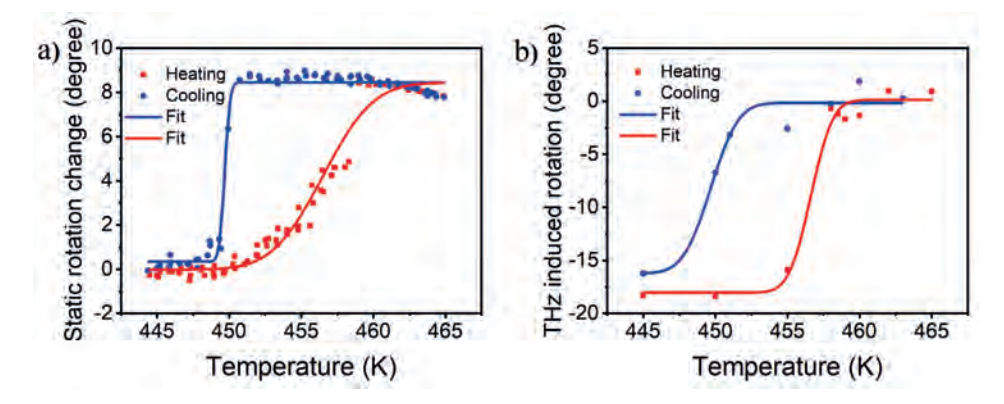


Figure 6.8. The static linear rotation change versus dynamic linear rotation change as function of temperature. a) Static linear rotation as function of temperature. Experimental data are plotted in dots while solid lines are fitted trends upon heating (red) and cooling (blue). b) Extracted linear rotation change as function of temperature in presence of THz pump (1 MV/cm). The raw data are extracted from dynamic measurements (at zero time delay) as shown in figure 6.6. The fitting results are listed in the table below.

Fitting results (K)	Static rotation	THz induced rotation	
Transition temperature $\alpha \rightarrow \beta$	456.50±0.18	456.59±0.40	
Transition duration $\alpha \rightarrow \beta$	5.52±0.42	2.26±0.96	
Transition temperature $\beta \rightarrow \alpha$	449.69±0.05	449.65±1.06	
Transition duration $eta ightarrow lpha$	0.62±0.07	3.10±3.87	

Table 6.1. The comparison of fitting results between static linear rotation change and dynamic linear rotation change presented in Figure 6.7.

The transition temperature denotes the critical temperature where the phase transition occurs.

The transition duration denotes the energy barrier (heat) that is needed for the transition to complete.

Based on the fitted data shown in Table 6.1, it seems that the needed transition energy (as indicated by the transition duration) is lower when the THz pulse is present (2.26±0.96 K < 5.53±0.42 K) whereas the onset temperatures for the reversible phase transitions ($\alpha \rightarrow \beta$ and $\beta \rightarrow \alpha$) are the same. However, this can be influenced by multiple reasons. Figure 6.9 is the same set of data but with an analysis including the heating rate factor. The corrected results seem to match each other very well, meaning the two parameters, transition temperature and transition duration, do not change upon the application of a THz pulse.

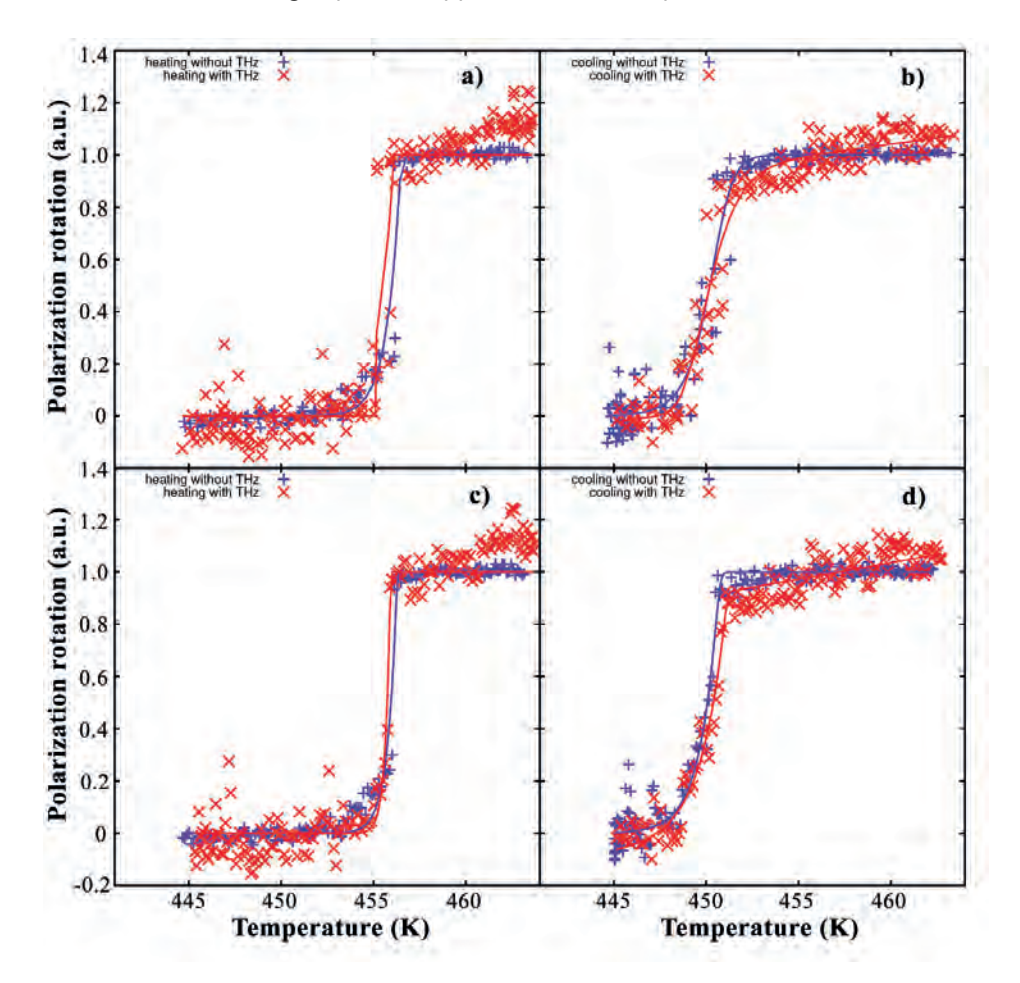


Figure 6.9. Corrected heating and cooling polarization rotation change in the absence/presence of a THz pump.

Raw experimental data of polarization rotation change during a) heating and b) cooling processes. Corrected data based on the heating rate (2 K/min) during heating c) and cooling d). The red dots and curves represent the polarization rotation change in the presence of THz pump pulses whereas the blue ones represent the polarization rotation change without THz pump. The dots are acquired during experiments at certain temperatures while the lines are fitted results by Sigmoid function.

6.4.3 Pump power dependence

To gain more insight in a potential THz effect on the phase transition, pump power dependent measurements were carried out under identical experimental conditions. The THz pump pulse was firstly blocked to ensure zero power of the THz pump, and a hysteresis loop of the detected probe polarization rotation was obtained after a heating and cooling cycle, as plotted in Figure 6.10a. This is compared to the polarization rotation change under the presence of THz pump pulses with a strength of 500 KV/cm, 750 KV/cm and a maximum of 1000 KV/cm, as presented in Figure 6.10.

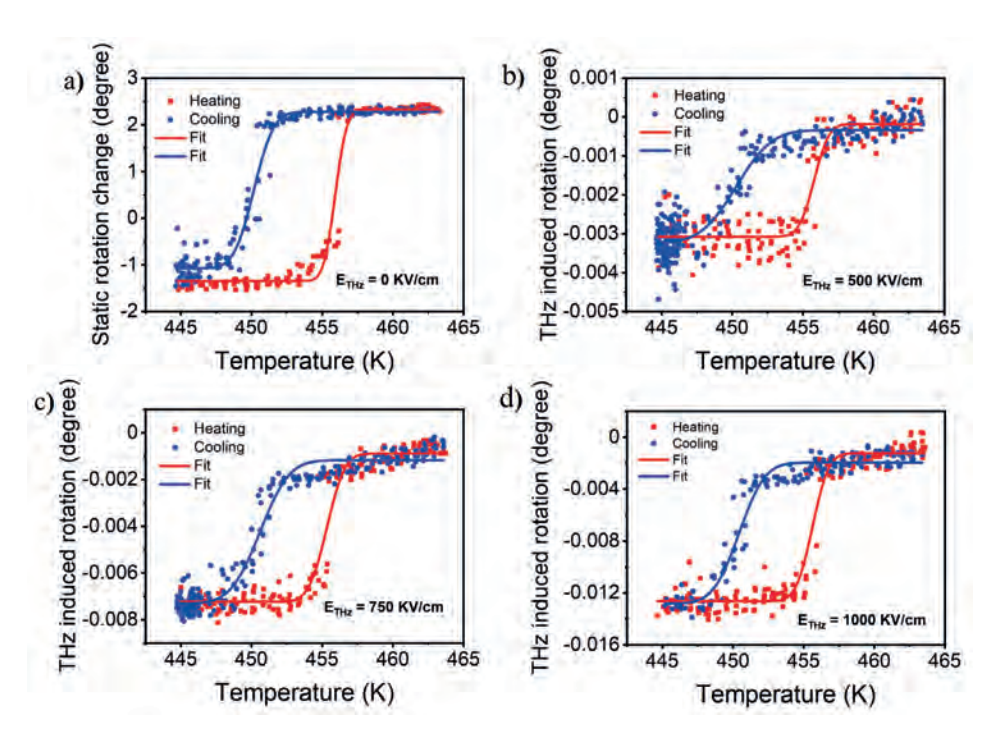


Figure 6.10. The polarization rotation change induced by the THz pump with a power of a) 0 KV/cm, b) 500 KV/cm, c) 750 KV/cm and d) 1000 KV/cm. The raw data are plotted in dots (red for heating and blue for cooling) and the solid lines indicate the fitted results with a step function.

The difference of the rotation values between the high temperature phase and the low temperature phase is a result from the structural phase transition of 4-DBpFO and it increases with the increase of pump power. The absolute THz induced rotation values (0.003°, 0.007° and 0.012°, as obtained from Figure 6.10b, c, and d) increase quadratically with the input THz pump power (500 KV/cm, 750 KV/cm, 1000 KV/cm). This matches with the discussion of Figure 6.5 that 4-DBpFO responses quadratically to the THz pulses.

Fitting results (K)	1000 KV/cm	750 KV/cm	500 KV/cm	0 KV/cm
Transition temperature $\alpha \rightarrow \beta$	455.62±0.10	455.33±0.10	455.79±0.15	455.92±0.07
Transition duration $\alpha \rightarrow \beta$	1.82±0.23	2.01±0.23	1.68±0.31	1.30±0.15
Transition temperature $\beta \rightarrow \alpha$	450.43±0.11	450.60±0.09	450.29±0.18	450.16±0.08
Transition duration $\beta \rightarrow \alpha$	2.89±0.29	3.27±0.24	3.96±0.51	2.21±0.19

Table 6.2. The comparison of fitting results between static linear rotation change and dynamic linear rotation change presented in Figure 6.10.

In summary, a detailed analysis of the experimental results shows no THz pump impact on the phase transition temperature, neither on the phase transition duration. This is most likely due to the fact that the THz gradient applied in the experiment is five orders of magnitude smaller than the one used in the theoretical simulations. The calculated electric-field-gradient in the experiment was:

$$abla E_{
m THz} = rac{1 M {
m V/cm}}{3*10^{10} {
m cm/s}*0.5 {
m ps}} = 6.7*10^7 \left({
m V/cm}^2
ight)$$

The theoretically applied electric-field-gradient was: $\nabla E_{\mathrm{theory}}$ = 1 * $10^{13} (\mathrm{V/cm^2})$, which is more than five orders of magnitude higher.

On the other hand, the field strength of the FLARE pulses is calculated 138-140 to be $E_{\rm FLARE} = 4.0 * 10^4 \, ({\rm V/cm})$:

$$E_{ ext{FLARE}} = \sqrt{rac{J}{0.3622\pi w^2 \epsilon_0 c \Delta t}}$$

J: pulse energy, $1\mu J$

w: diameter of the THz spot at the sample, 1 mm

c: speed of light in vacuum, $3*10^8(m/s)$

 ϵ_0 : permittivity of vacuum, $8.854 * 10^{-12} (F/m)$

 Δt : pulse width, 20 ps

The electric-field-gradient for the FLARE beam is calculated to be:

$$abla E_{
m FLARE} = rac{4.0*10^4 {
m V/cm}}{3*10^{10} {
m cm/s}*20 {
m ps}} = 6.7*10^4 \left({
m V/cm}^2
ight)$$

In both the FLARE experiment and the strong THz pump-probe study, the goal was to resonantly pump the structural phase transition as the wavelength was set close to the phonon mode (1.2 THz) calculated in section 6.2. This could not be achieved, most likely because the electric field gradients in both cases were several orders of magnitude weaker than the theoretically predicted one. However, a phase boundary movement was observed in the FLARE experiment. This is likely due to a heating effect for 2 reasons: first, the effect only occurred at high repetition rate (3 GHz, instead of 20 MHz); second, the electric field gradient was not enough to drive the phase transition resonantly compared to simulation results.

Besides, pumped by the FLARE beam, it was only possible to see the movements of the phase boundary. The complete shape transformation of the single crystal was achieved only by heating the sample directly in contact with a heating stage. This indicates that transforming the whole single crystal requires a higher power of the pumping beam. Moreover, the movement of the phase boundary in the FLARE experiment is on the microsecond time scale, which is too slow to be detected in an ultrafast THz pump-optical probe experiment, which normally detects dynamics on the picosecond timescale.

6.5 THz induced SHG across phase transition

Both the α and β phases of 4-DBpFO feature a centrosymmetric crystal structure, making it intrinsically non-responsive to even order nonlinear optical effects such as second harmonic generation. However, as discussed in section 1.2.2, when strong THz pump pulse is applied, SHG signals can be observed even in a medium with centrosymmetric structure. Besides, SHG is often used as an efficient probe method in ultrafast pump-probe experiments 140,141.

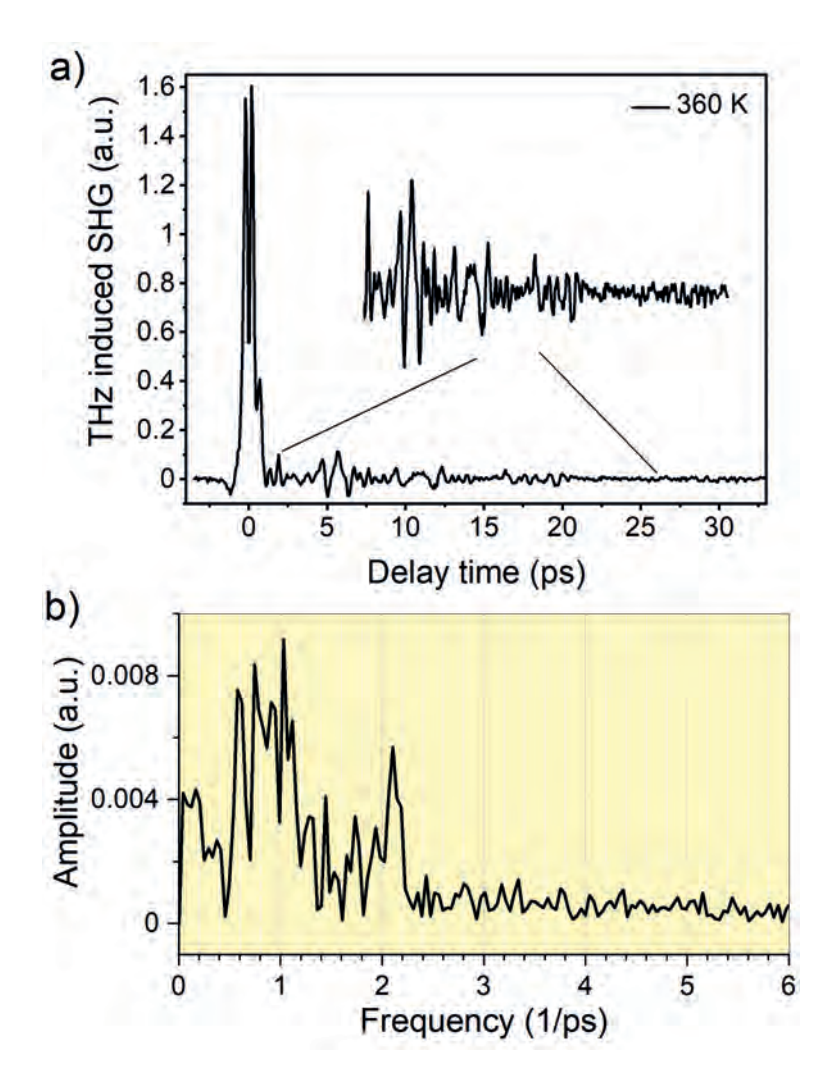


Figure 6.11. Time-resolved oscillations of THz induced SHG.

a) Time-resolved SHG signal. The inset is a magnified view of the oscillations at 360 K. b) Fourier transformation of the oscillation shown in a).

Both α (orthorhombic Pnma) and β phases (monoclinic P2₁/n) possess centrosymmetric crystal structures, meaning that there is no intrinsic SHG emission from the 4-DBpFO single crystal. However, with the strong THz pulse serving as pump beam, a THz induced SHG (TSHG) is observed during the measurements. Moreover, the TSHG signal shows a similar hysteresis loop as linear polarization rotation change described in session 6.4.2. This suggests that the TSHG is also sensitive to the birefringent change during the structural phase transition, as the TSHG signal is originally polarized. Therefore, changes in the TSHG signal contains information about the phase transition.

With FFT a strong oscillation mode at 1.0 THz is observed, which coincide with the predicted resonant phonon mode that triggers the structural phase transition in 4-DBpFO (as discussed in the section below).

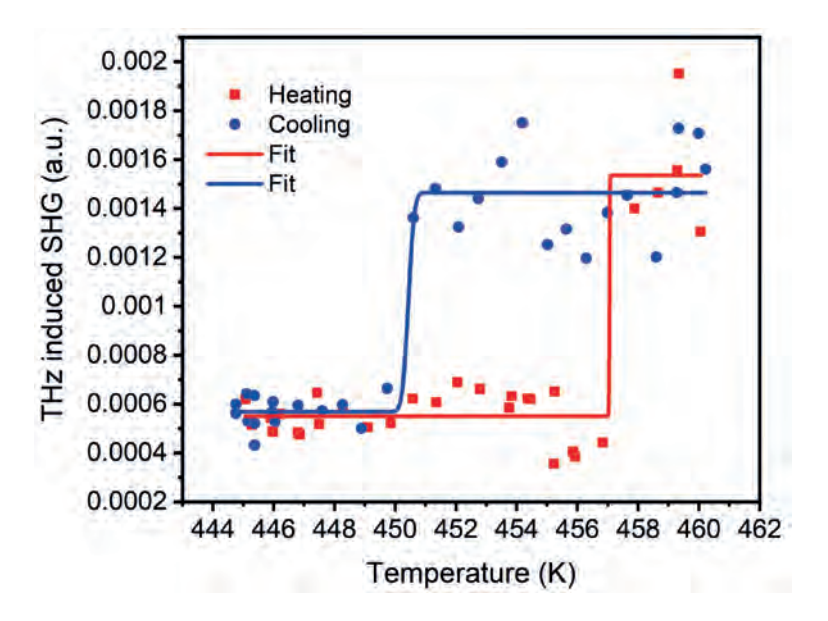


Figure 6.12. The THz induced SHG signal as a function of temperature. THz induced SHG intensity is detected at the wavelength of 400 nm with full strength THz pump and 800

nm probe. The temperature remains in the vicinity of the phase transition temperature to ensure the occurrence of the reversible structural phase transition on the 4-DBpFO crystal. Experimental data are plotted in dots while solid lines are fitted tendencies upon heating (red) and cooling (blue).

We tracked the TSHG intensity at zero time delay when the sample system was going through a heating and cooling cycle. The signal is induced by the full strength of THz pulses (1 MV/cm). The as-observed SHG intensity is plotted in Figure 6.12. The raw data are fitted with equation 2.1. The TSHG seems to be an effective way to mark the completion of the $\alpha \rightarrow \beta$ phase transition in 4-DBpFO single crystals.

6.6 Conclusion and outlook

Static experiment using FLARE as pump has shown the possibility to trigger the structural phase transition in 4-DBpFO single crystals. The home-built microscope setup recorded the phase boundary movements upon shining of FLARE beam. Unfortunately, no dynamic measurements could be realized using FLARE.

The simulation results discussed in Chapter 3 found a good match with the experimental Raman spectra and also suggested that the phase transition in 4-DBpFO crystal can be resonantly driven by applying a pulse of an electric field gradient in the frequency range of 1.0-1.5 THz. Therefore, time-resolved measurements using strong THz (1 MV/cm) pulses as pump and optical pulses (800 nm) as probe have been applied to study the THz induced phase transition in 4-DBpFO single crystals. 4-DBpFO crystals showed a quadratic response in the birefringence at the overlap of pump and probe pulses. A hysteresis change was observed upon the phase transition with and without THz pump pulses. However, after detailed analysis, it was shown that the THz pump had no measurable impact on the transition temperature nor the transition energy needed during heating or cooling. This is likely due to the relatively weak electric field gradient in the lab comparing to the theoretical calculations.

In addition, THz induced Second Harmonic Generation (TSHG) was shown to be closely related to the structural change in 4-DBpFO, which could be a new approach to study the structural phase transition in 4-DBpFO.



Summary and outlook

In summary, to reveal the origin of the intriguing thermosalient structural phase transition in the molecular crystal 4-DBpFO, its static and dynamic optical properties were studied using various spectroscopic methods. First, the birefringence and fluorescence properties of the crystal were investigated as a function of temperature. Although fluorescence emission gave no particular changes across the phase transition, the birefringence changed dramatically at the transition from the α to the β phase. This change in birefringence is further used as a probe in time-resolved pump-probe experiments.

In-situ Raman experiment combined with molecular dynamic simulations disclosed the order parameter during the structural phase transition in 4-DBpFO and presented two phonon modes at low frequency, the wagging mode of ring2 groups at 55 cm⁻¹ and the torsion motion at 106 cm⁻¹ between ring1 and ring2 groups, that together are responsible for the structural phase transition in 4-DBpFO. To experimentally follow these modes as a function of the order parameter, we used a line-scan technique across a temperature controllable phase boundary between the two phases. As predicted by simulations, strong THz laser pulses at around 1.5 THz (~55cm⁻¹) are expected to non-thermally trigger the phase transition in 4-DBpFO single crystals. The study of this is presented in Chapter 6 and partly confirmed this.

Ultrafast optical pump-probe experiments were performed with the aim to disclose the dynamics during the structural phase transition in 4-DBpFO. Based on a homebuilt setup, the time-resolved transmission was first studied. The results demonstrate two mechanisms, a fast decay with amplitude A1 and a slow decay with amplitude A2 and with decay times of a few hundreds of picoseconds and a few nanoseconds, respectively. These two exponential decays after optical excitation reflect the dynamics of electron charges from excited states. As the decay time lasts longer than nanoseconds, it suggests that the excited electrons will not come back to their ground state in a few nanoseconds, indicating that the sample system needs more time to relax back to its original state. However, the pump we applied is operating at 1kHz, giving a millisecond time for the system to relax before the next pump comes. Therefore, between two pump pulses, the sample should be relaxed back.

The observed optical pump-induced polarization rotation of the probe beam does mark the structural phase transition in 4-DBpFO crystals and is dominated by a

single mechanism. The polarization rotation first increases in the α phase and reaches a saturation state when the temperature is near the critical temperature. When the phase transition happens, the crystal changes its shape which leads to a significant change of rotation value due to the sheared orientation of the crystal. The underlying mechanism is analysed by fitting its decay time and amplitude. Both the decay time and amplitude give a step-like behaviour at the transition. The onset temperatures obtained by fitting the polarization rotation and the decay time have a relatively large difference. This is explained by the combination of local heating and the nucleation-and-growth mechanism of the structural phase transition in 4-DBpFO.

A static measurement using THz pulses from the FLARE beam of the free electron laser facility FELIX as pump has shown that the phase transition in 4-DBpFO can be triggered at a frequency near 1.5 THz. Therefore, a table top strong THz pump and optical probe experiment was designed and carried out. A strong quadratic response was observed at the overlap of the THz pump and the optical probe pulses. However, when varying the pump powers, no measurable impact was observed on the transition temperature nor on the transition energy needed during heating or cooling. Thus, no phase transition occurs under the pump of strong THz pulses up to 1MV/cm. This could be because of the relatively weak electric field gradient in the table top experiment compared to the theoretical simulations.

As an outlook, the line-scan technique that we used in Chapter 4 might be an effective tool to study phase transitions, where the phase boundary is controllable under certain conditions. Although the dynamics of the phase transition is still not clear at the microscopic level, the optical pump-probe experiment has shown that the thermosalient phase transition in 4-DBpFO can be driven by ultrafast laser pulses, opening the door for ultrafast dynamic studies on other thermosalient crystals using proper optical tools.

For example, the dynamics of the phase transition in 4-DBpFO can be further studied by an optical pump and X-ray probe, as a 400 nm pump is capable of bringing the sample over the phase transition, while an X-ray probe may provide an insight in the atomic movements at the structural phase transition. As a next step, a THz pump and an X-ray probe could be used to study the details of coherently controlling the phase transition.



Samenvatting en vooruitzicht

Samenvattend, om de oorsprong van de intrigerende thermosalient structurele faseovergang in het moleculaire kristal 4-DBpFO te onthullen, werden de statische en dynamische optische eigenschappen bestudeerd met behulp van verschillende spectroscopische methoden. Eerst werden de dubbelbreking en fluorescentie eigenschappen van het kristal onderzocht als functie van de temperatuur. Hoewel de fluorescentie-emissie geen specifieke veranderingen vertoonde tijdens de faseovergang, veranderde de dubbelbreking drastisch bij de overgang van de alfanaar de bètafase. Deze verandering in dubbelbreking werd later gebruikt als een probe voor tijdsopgeloste pomp-probe-experimenten.

Een in-situ Raman-experiment, gecombineerd met moleculaire dynamicasimulaties, onthulde dat de ordeparameter voor de structurele faseovergang in 4-DBpFO gekoppeld is aan twee laag frequente roostertrillingen: de "wagging" (rotatie) mode van de ring2-groepen bij 55 cm⁻¹ en de torsiebeweging tussen de ring1- en ring2groepen bij 106 cm⁻¹. Samen blijken deze twee verantwoordelijk voor de structurele faseovergang in 4-DBpFO. Om deze roostertrillingen experimenteel te bestuderen als functie van de ordeparameter, werd een lijn-scantechniek gebruikt over een fasegrens tussen de twee fasen. Dit was mogelijk doordat deze fasegrens met behulp van de temperatuur gestabiliseerd kon worden. De simulaties voorspelden ook dat een sterke THz-laserpulse rond de 1,5 THz (~55cm⁻¹) de faseovergang in 4-DBpFO niet-thermisch kan activeren. Dit wordt besproken in Hoofdstuk 6, waar deze hypothese gedeeltelijk werd bevestigd.

Ultrasnelle optische pomp-probe-experimenten werden uitgevoerd met als doel de dynamika tijdens de structurele faseovergang in 4-DBpFO te onthullen. Met behulp van een zelfgebouwde opstelling werd de tijdsafhankelijke transmissie bestudeerd. De resultaten tonen twee mechanismen aan: een snelle vervalcomponent met amplitude A1 en een langzame vervalcomponent met amplitude A2, met vervaltijden van respectievelijk een paar honderd picoseconden en een paar nanoseconden. Deze twee exponentiële vervallen na optische weerspiegelen de dynamika van de ladingsdragers vanuit geëxciteerde toestanden. Aangezien de vervaltijd langer duurt dan enkele nanoseconden, suggereert dit dat de geëxciteerde elektronen niet binnen enkele nanoseconden terugkeren naar hun grondtoestand. Dit impliceert dat het systeem meer tijd nodig heeft om terug te keren naar zijn oorspronkelijke toestand. Echter, aangezien de pomp werkt met een herhalingsfrequentie van 1 kHz, heeft het systeem enkele milliseconden om te relaxeren voordat de volgende pomppuls arriveert, wat ruim voldoende moet zijn.

De waargenomen optische pomp-geïnduceerde polarisatierotatie van de probe markeert de structurele faseovergang in 4-DBpFO-kristallen en wordt gedomineerd door een enkel mechanisme. De polarisatierotatie neemt eerst toe in de α -fase en bereikt een verzadigingsniveau wanneer de temperatuur nabij de kritische temperatuur komt. Wanneer de faseovergang plaatsvindt, verandert de kristalvorm, wat leidt tot een significante verandering in de rotatiewaarde door de afschuiforiëntatie van het kristal. Het onderliggende mechanisme werd geanalyseerd door de vervaltijd en amplitude te fitten. Zowel de vervaltijd als de amplitude vertonen een stapachtige verandering bij de overgang. De onsettemperaturen verkregen uit het fitten van de polarisatierotatie en de vervaltijd vertonen een relatief groot verschil. Dit wordt verklaard door een combinatie van lokale verhitting en het nucleatie-en-groei-mechanisme van de structurele faseovergang in 4-DBpFO.

Een statische meting met behulp van THz-pulsen van de FLARE-bundel van de vrijeelektronenlaserfaciliteit FELIX als pomp heeft aangetoond dat de faseovergang in 4-DBpFO kan worden geactiveerd bij een frequentie rond 1,5 THz. Daarom werd een laboratorium-experiment ontworpen en uitgevoerd met een laser-geinduceerde THz-pomp en een optische probe. Een sterke kwadratische respons werd waargenomen wanneer de THz-pomp- en optische probe-pulsen overlappen in tijd. Echter, bij variatie van de pompintensiteit werd geen meetbare invloed waargenomen op de overgangstemperatuur noch op de energie die nodig is voor de faseovergang tijdens verwarming of koeling. Dit betekent dat er geen faseovergang optreedt onder invloed van optisch gegenereerde THz-pulsen tot 1 MV/cm. Dit zou kunnen komen door het relatief zwakke elektrisch veldgradiënt in het experiment vergeleken met de simulaties.

Wat betreft de toekomst: De lijn-scantechniek die we in Hoofdstuk 4 gebruikten, zou een effectief hulpmiddel kunnen zijn voor het bestuderen van faseovergangen, waarbij de fasegrens onder bepaalde omstandigheden controleerbaar is. Hoewel de dynamika van de faseovergang op microscopisch niveau nog niet volledig begrepen is, heeft het optische pomp-probe-experiment aangetoond dat de thermosalient faseovergang in 4-DBpFO kan worden aangedreven door ultrasnelle laserpulsen. Dit opent de deur naar verdere studies over ultrasnelle dynamica in andere thermosaliente kristallen met behulp van geschikte optische technieken.

Bijvoorbeeld, de dynamika van de faseovergang in 4-DBpFO kan verder worden onderzocht met een optische pomp en een röntgenprobe. Een 400 nm pomp is in staat om het kristal over de faseovergang te brengen, terwijl de röntgenprobe inzicht kan geven in de atomaire bewegingen tijdens de structurele faseovergang. Als volgende stap zou een THz-pomp gecombineerd met een röntgenprobe kunnen

worden gebruikt om de details van coherente controle over de faseovergang te bestuderen.



Research Data Management

This thesis research has been carried out in accordance with the research data management policy of the Institute for Molecules and Materials (IMM) of Radboud University, the Netherlands. The following datasets have been produced during the research:

• Chapter 1: Sergey Semin, Xinyue Li, Yulong Duan, Theo Rasing. Advanced Optical Materials (2021).

https://doi.org/10.1002/adom.202100327

CNCZ Radboud University. smb:\\uscm-ssi-srv.science.ru.nl\uscm-ssi\Xinyue\ Nonlinear Optical **Properties** and **Applications** of Fluorenone Molecular Materials

• Chapter 3: Xinyue Li et al. in preparation CNCZ Radboud University. smb:\\uscm-ssi-srv.science.ru.nl\uscm-ssi\Xinyue\

• Chapter 4: Saba Ghasemlou, Xinyue Li, Daria R Galimberti, Timur Nikitin, Rui Fausto, Jialiang Xu, Steven Holleman, Theo Rasing, Herma M Cuppen. Proceedings of the National Academy of Sciences (2024).

https://doi.org/10.1073/pnas.2408366121

CNCZ Radboud University. smb:\\uscm-ssi-srv.science.ru.nl\uscm-ssi\Xinyue\ Identifying and controlling the order parameter for ultrafast photoinduced phase transitions in thermosalient materials

• Chapter 4: Daria Ruth Galimberti, Xinyue Li, Timur Nikitin, Rui Fausto, Jialiang Xu, Theo Rasing, and Herma Cuppen. Under review in Journal of the American Chemical Society (2025).

CNCZ Radboud University. smb: \\uscm-ssi-srv.science.ru.nl\uscm-ssi\Xinyue\ Characterizing gateway modes for solid-solid phase transitions in organic crystals: the thermosalient 4-DBpFO

• Chapter 5: Xinyue Li et al. in preparation

CNCZ Radboud University. smb:\\uscm-ssi-srv.science.ru.nl\uscmssi\Xinyue\Optical pump-probe study of the thermosalient phase transition in 4-DBpFO molecular crystals

• Chapter 6: Xinyue Li et al. in preparation CNCZ Radboud University. smb:\\uscm-ssi-srv.science.ru.nl\uscm-ssi\Xinyue\



Acknowledgements

Time flies. I can still feel the chill of the heavy snow in early 2017 on my hands, yet now I am about to welcome my ninth winter in the Netherlands. Back then, I was a fresh master student trying to communicate with my poor spoken English, but now I am an experienced researcher who can speak three languages. So many changes have happened and so many wonderful memories have etched into my life. Writing this acknowledgement is a great opportunity to look back, to cherish those years, and to express my deepest gratitude to the people who have played such an important role in my journey.

The first and foremost "thank you" goes to Theo, my dearest professor, supervisor, and mentor. Theo, there is no doubt that you are a brilliant scientist, but to me you have been far more than that—you have also been an excellent guide and a role model in my life. It has been a great honor to work so closely with you over the past eight years. I am deeply grateful not only for the way you have taught me how to conduct research, but also for the way you have inspired me to find passion and meaning in life. You have witnessed my growth, and words are not enough to express my gratitude for your scientific professionalism, your supervision, your patience, your kindness, and so much more.

Jialiang, without you, this journey would never have begun. A true turning point in my life was the moment you accepted me as your master's student. Your passion for materials science and for research in general deeply impressed me and inspired me to follow your path. You taught me invaluable skills—not only in experimentation and writing, but also in communication and collaboration. Since then, I have come a long way. Without you, I would never have met Theo, nor would I have set foot in the Netherlands.

Alexey, I had heard about your legend since my very first week in the group. You are undoubtably a brilliant scientist and a successful researcher. I feel fortunate to have had the opportunity to attend your courses and engage in scientific discussions with you. Your knowledge and your way of guiding your students sharp, strong and always to the point - have helped us build a solid foundation and develop good habits in the pursuit of science. Your confidence makes your students confident too.

Marilou, you are truly the heart of the group. You have always welcomed me with your warm smile and positive attitude. I cannot thank you enough for everything you have done for me, not only in terms of work but also in life and personal growth.

Sergey, I thank you for the training and supervision during the first two years of my PhD. Your way of working has influenced me greatly. You shaped my research habits, and without your guidance, this PhD trajectory would never have found its path to success. Dima, I will never forget the moment when we found the time zero on my setup! You guided me through all possible ways in the lab, hand in hand, to optimize the signal. I am really happy that you returned to the group and I strongly believe that you will become a great supervisor.

Chris, hartelijk dank voor alles wat u voor mij heeft gedaan. In het bijzonder dank voor de heater die u voor mij heeft gebouwd, zonder welke dit proefschrift nooit tot stand zou zijn gekomen.

Collaboration has always been a key word in research, and I have been lucky to work with many excellent researchers on various topics. I would first like to thank professor Paul Kouwer, who granted me access to his lab and provided all the organic solvents that were essential for growing the thermosalient crystals. Secondly, I would like to thank professor Rui Fausto and Dr. Timur Nikitin from Coimbra University in Portugal. Thank you for supporting me in applying the LaserLab Europe funding and working together with me to complete the Raman experiments. I am also very grateful for your kindness during my stay in Portugal. It was a truly valuable and fruitful collaboration. I am also deeply thankful to professor Herma Cuppen and Dr. Daria Galimberti for contributing your scientific insights to the Raman projects. I have treasured every discussion we shared and I am continually inspired by your passion and creativity. Working with you has been both stimulating and joyful.

Yulong, you are the pioneer in discovering this thermosalient crystal in the group. Your diligence and attention to detail have been a great role model for me. I thank you for your leading and guidance at the beginning of my PhD and I wish you and your family all the best in the future. Kamyar, I feel fortunate to have worked with you on the FLARE project, and I appreciate the effort you dedicated to it. Thank you! My gratitude also goes to Carl for the time and energy you invested in this project. To me, you are not only an outstanding researcher who tackles challenges with a hands-on attitude, but also a great friend who always brings humor and positivity to the team. I wish you all the best in continuing to pursue your passions. I would also like to thank Dr. Hans Engelkamp for supporting me with the FTIR measurements. Many thanks to Dr. Paul Tinnemans for supporting on the SCXRD experiment and helping on managing ultra-small crystals. Thanks to Peter Mulder

for supporting in defining the thickness of the crystals. Thanks to Alexander, Nikolai and Dinar on participating in the single shot pump-probe experiments and for daily discussions. You are passionate researchers with interesting personalities. Special thanks to Dinar for being my paranymph. You have always been having a strong and clear mind where to go and how to go, and I am certain that you will make it in the near future! Vlad and Lucas, thank you for helping me out on the THz experiments. You two are absolutely expert in what you do. And hopefully the results may lead to a publication in the near future. I am also looking forward to collaborate with Lucas, Dinar and Vivek on our new projects, finger crossed!

Andrei and Johan, although we haven't overlapped much for work, but I am grateful for your kindness. Anna P, Anna G, Saliba, Variely, Eugene and Kris, it was nice to have you as my office-mates and I am thankful for the kindness you showed to me; Albert, Kshiti, Fabio, Guido, Giammarico, Kiran and Kirill, Alexander and Irina, I am so happy that I met you guys and that we are still in contact. Martijn, Dominique, Hervoje, Torstein, Ketty, Rutger, Peter and Pim, you are all smart researchers and I have learned important principles from you while being in the same office with you. Thanks to Thomas M, Thomas B, Thomas W, Timur, Ketty, Peter, Paul, Rein, Jim, Lukas, Viktoriia, Sheng and Hongyi for building such a nice group atmosphere and for useful discussions. I am also grateful to Shuang Wu for patiently answering all my academic questions and for agreeing to be my paranymph.

Thank you to my dining companions Xiaochen, Siwen, and Jingyi. Those wonderful moments we shared over meals were a source of strength that kept me going throughout this journey. My gratitude also goes to my seniors, Long Cheng and Yuze—the days we spent together in Nijmegen were short but unforgettable. Thank you to my friend Yuxi; meeting you and connecting so deeply during the pandemic was one of the warmest parts of this journey. Thanks to my housemates Amy and Raisa for being my friend and giving me constant support throughout these years.

Most importantly, I would like to express my sincere gratitude to all the manuscript committee members for taking the time to read this thesis and provide constructive feedback. Your insightful comments and suggestions have greatly contributed to making this work clearer, more refined and more complete.

Last but not least, the completion of this thesis would not have been achieved without the help and support of my husband, my best friend and my lover, Dr. Guangiao Li. Even though discussions on physics somehow always bring us to arguments, that still sparked me to think and gain new perspectives. Thank you for being the constant one beside me over the years, and thank you for putting more

effort into the family when I could not. My dearest, my son, Bohan, you made me a believer. You are the true wonder in my life. I thank you for being my son and showing me the colorful meanings of life. A big thanks to my parents in law, who are always positive and supportive to our small family, who are always ready to offer all of their time and effort, who are always there with us no matter what.

一路走来,感恩我的父母。你们生我养我,在我想要前进时给我支撑和勇气,在我害怕退缩时做我坚实的后盾。谢谢你们三十多年如一日地爱我、包容我,没有你们就没有今天的我。也谢谢我弟一肩担起孝顺和陪伴的义务,以及愿意听我偶尔碎碎念还暖心开导我。

This PhD journey spans from my 20s to my 30s. During this time, I moved from China to the Netherlands, I met and married to my soul mate. A girl became a lady, the lady became a mother, and eventually, she became a doctor. These earth-shaking changes all took place in these 8 years, a dramatic period: there was pandemic, there was war, there was inflation and there was great fire in the Brazilian forest. And somewhere in Nijmegen, a girl has been simply working, even though she might not be as fast, but she has been moving firmly towards the goal.



List of Publications

- X. Li, Y. Duan, S. Semin, J. Xu, T. Rasing, "Temperature dependent optical birefringence of two polymorphs of 4-DBpFO" (in preparation)
- X. Li, S. Semin, Y. Duan, J. Xu, A. Kimel, T. Rasing, "Optical pump probe study of the phase transition in 4-DBpFO molecular crystals" (in preparation)
- D. R. Galimberti, X. Li, T. Nikitin, R. Fausto, H. M. Cuppen, J. Xu, T. Rasing, "Revealing the role of vibrational modes in a thermosalient structural phase transition using Raman spectroscopy" (in preparation).
- S. Ghasemlou, X. Li, D. R. Galimberti, T. Nikitin, R. Fausto, J. Xu, S. Holleman, T. Rasing, and H. M. Cuppen, "Identifying and controlling the order parameter for ultrafast photoinduced phase transitions in thermosalient materials" Proc. Natl. Acad. Sci. U.S.A. 2024, 121 (46) e2408366121.
- · S. Semin, X. Li, Y. Duan, T. Rasing, "Nonlinear optical properties and applications of fluorenone molecular materials" Adv. Optical Mater. 2021, 9, 2100327.
- J. Qin[#], F. Huang[#], X. Li[#], L. Deng, T. Kang, A. Markov, F. Yue, Y. Chen, X. Wen, S. Liu, Q. Xiong, S. Semin, T. Rasing, D. Modotto, R. Morandotti, J. Xu, H. Duan, and L. Bi, "Enhanced second harmonic generation from ferroelectric HfO₂-based hybrid metasurfaces" ACS Nano, 2019, 13, 1213–1222.
- Y. Dong, Y. Zhang, X. Li, Y. Feng, H. Zhang, and J. Xu, "Chiral Perovskites: Promising materials toward next-generation optoelectronics" Small. 2019, 1902237.
- C. Yuan#, X. Li#, S. Semin, Y. Feng, T. Rasing, and J. Xu, "Chiral lead halide perovskite nanowires for second-order nonlinear optics" Nano Lett., 2018, 18, 5411-5417.
- X. Li, S. Semin, L. A. Estrada, C. Yuan, Y. Duan, J. Cremers, P. Tinnemans, P. Kouwer, A. E. Rowan, T. Rasing, J. Xu, "Strong optical nonlinearities of selfassembled polymorphic microstructures of phenylethynyl functionalized fluorenones" Chin. Chem. Lett., 2017, 29, 2, 297-300.
- G. Zhai[#], X. Li[#], P. Jin, S. Semin, J. Xiao, T. Rasing, J. Xu, "Functionalized twistacenes for solid state nonlinear optical materials" Dyes and Pigments, 2017, 149, 876-881.

^{*}Contributed equally



Curriculum Vitae

Name: Xinyue Li

Date of birth: 11-01-1992

Place of birth: Qian'an city, Hebei province, China

2019-2025 – PhD Researcher

Radboud University, Nijmegen, The Netherlands

2018-2019 - Research assistant

Nankai University, Tianjin, China

2017-2019 – Guest Researcher

Radboud University, Nijmegen, The Netherlands

2016-2019 – MSc in Applied Chemistry

Tianjin University, Tianjin, China

2011-2015 – BSc in Chemical Engineering and Technology

Hebei University of Engineering, Handan, China

2008-2011 – High school diploma

Qian'an No.1 High School, Qian'an city, China



References

- 1. Cao, W., Cudney, H. H. & Waser, R. Smart materials and structures. Proceedings of the National Academy of Sciences **96**, 8330-8331, doi:10.1073/pnas.96.15.8330 (1999).
- 2. KÖK, M., Qader, İ. N., Dagdelen, F. & AydoĞDu, Y. A review of smart materials: researches and applications. El-Cezeri 6, 755-788, doi:10.31202/ecjse.562177 (2019).
- 3. Hou, I. C.-Y., Li, L., Zhang, H. & Naumov, P. Smart molecular crystal switches. Smart Molecules n/ a, e20230031, doi:https://doi.org/10.1002/smo.20230031 (2024).
- Bekas, D. G., Tsirka, K., Baltzis, D. & Paipetis, A. S. Self-healing materials: A review of advances in materials, evaluation, characterization and monitoring techniques. Composites Part B: Engineering 87, 92-119, doi:https://doi.org/10.1016/j.compositesb.2015.09.057 (2016).
- Wool, R. P. Self-healing materials: a review. Soft Matter 4, 400-418, doi:10.1039/B711716G (2008).
- 6. Sun, L. et al. Stimulus-responsive shape memory materials: A review. Materials & Design 33, 577-640, doi:https://doi.org/10.1016/j.matdes.2011.04.065 (2012).
- 7. Naresh, C., Bose, P. S. C. & Rao, C. S. P. Shape memory alloys: a state of art review. IOP Conference Series: Materials Science and Engineering 149, 012054, doi:10.1088/1757-899X/149/1/012054 (2016).
- 8. Hager, M. D., Greil, P., Leyens, C., van der Zwaag, S. & Schubert, U. S. Self-Healing Materials. Advanced Materials 22, 5424-5430, doi:https://doi.org/10.1002/ adma.201003036 (2010).
- Bogue, R. Shape-memory materials: a review of technology and applications. Assembly 9. Automation 29, 214-219, doi:10.1108/01445150910972895 (2009).
- 10. Mahmoud Halabi, J. et al. Microelectromechanical devices driven by thermosalient effects. Cell Reports Physical Science 3, 101133, doi:https://doi.org/10.1016/j.xcrp.2022.101133 (2022).
- Skoko, Ž., Zamir, S., Naumov, P. & Bernstein, J. The Thermosalient Phenomenon. "Jumping Crystals" and Crystal Chemistry of the Anticholinergic Agent Oxitropium Bromide. Journal of the American Chemical Society 132, 14191-14202, doi:10.1021/ja105508b (2010).
- 12. Naumov, P., Sahoo, S. C., Zakharov, B. A. & Boldyreva, E. V. Dynamic Single Crystals: Kinematic Analysis of Photoinduced Crystal Jumping (The Photosalient Effect). Angewandte Chemie International Edition 52, 9990-9995, doi:10.1002/anie.201303757 (2013).
- 13. Naumov, P. et al. The Rise of the Dynamic Crystals. Journal of the American Chemical Society 142, 13256-13272, doi:10.1021/jacs.0c05440 (2020).
- Etter, M. C. & Siedle, A. R. Solid-state rearrangement of (phenylazophenyl)palladium hexafluoroacetylacetonate. Journal of the American Chemical Society 105, 641-643, doi:10.1021/ja00341a065 (1983).

- Gigg, J., Gigg, R., Payne, S. & Conant, R. The allyl group for protection in carbohydrate chemistry. Part 18. Allyl and benzyl ethers of myo-inositol. Intermediates for the synthesis of myo-inositol trisphosphates. *Journal of the Chemical Society, Perkin Transactions* 1, 423-429, doi:10.1039/P19870000423 (1987).
- Ding, J., Herbst, R., Praefcke, K., Kohne, B. & Saenger, W. A crystal that hops in phase transition, the structure of trans,trans,anti,trans,trans-perhydropyrene. *Acta Crystallographica Section B* 47, 739-742, doi:doi:10.1107/S0108768191004500 (1991).
- 17. Fattah, J., Twyman, J. M. & Dobson, C. M. A variable-temperature 13C cross-polarization magic angle spinning NMR study of some unusual dynamic and phase properties of (±)-3,4-di-O-acetyl-1,2,5,6-tetra-O-benzyl-myo-inositol, 'jumping crystals'. *Magnetic Resonance in Chemistry* 30, 606-615, doi:https://doi.org/10.1002/mrc.1260300706 (1992).
- Steiner, T., Hinrichs, W., Saenger, W. & Gigg, R. `Jumping crystals': X-ray structures of the three crystalline phases of ([plus-minus sign])-3,4-di-O-acetyl-1,2,5,6-tetra-O-benzyl-myo-inositol. Acta Crystallographica Section B 49, 708-718, doi:doi:10.1107/S0108768193000795 (1993).
- Naumov, P., Chizhik, S., Panda, M. K., Nath, N. K. & Boldyreva, E. Mechanically Responsive Molecular Crystals. *Chemical Reviews* 115, 12440-12490, doi:10.1021/acs.chemrev.5b00398 (2015).
- Gaztanaga, P., Baggio, R., Halac, E. & Vega, D. R. Thermal, spectroscopic and structural analysis
 of a thermosalient phase transformation in tapentadol hydrochloride. *Acta Crystallographica*Section B 75, 183-191, doi:doi:10.1107/S2052520619001148 (2019).
- Gupta, P., Karothu, D. P., Ahmed, E., Naumov, P. & Nath, N. K. Thermally Twistable, Photobendable, Elastically Deformable, and Self-Healable Soft Crystals. Angewandte Chemie International Edition 57, 8498-8502, doi:10.1002/anie.201802785 (2018).
- 22. Duan, Y. et al. Robust thermoelastic microactuator based on an organic molecular crystal. Nature Communications 10, 4573, doi:10.1038/s41467-019-12601-y (2019).
- Mirvakili, S. M. & Hunter, I. W. Artificial Muscles: Mechanisms, Applications, and Challenges. Advanced Materials 30, 1704407, doi:https://doi.org/10.1002/adma.201704407 (2018).
- 24. Wei, C. et al. Flexible molecular crystals for optoelectronic applications. *Chemical Society Reviews*, doi:10.1039/D3CS00116D (2024).
- Sahoo, S. C., Panda, M. K., Nath, N. K. & Naumov, P. Biomimetic Crystalline Actuators: Structure–Kinematic Aspects of the Self-Actuation and Motility of Thermosalient Crystals. *Journal of the American Chemical Society* 135, 12241-12251, doi:10.1021/ja404192g (2013).
- 26. Zamir, S., Bernstein, J. & Greenwood, D. J. A Single Crystal to Single Crystal Reversible Phase Transition Which Exhibits The "Hopping Effect". Molecular Crystals and Liquid Crystals Science and Technology. Section A. Molecular Crystals and Liquid Crystals 242, 193-200, doi:10.1080/10587259408037751 (1994).
- 27. Klaser, T. *et al.* Does Thermosalient Effect Have to Concur with a Polymorphic Phase Transition? The Case of Methscopolamine Bromide. *Crystals* **8** (2018).

- 28. Seki, T., Mashimo, T. & Ito, H. Anisotropic strain release in a thermosalient crystal: correlation between the microscopic orientation of molecular rearrangements and the macroscopic mechanical motion. Chemical Science 10, 4185-4191, doi:10.1039/C8SC05563G (2019).
- Srirambhatla, V. K., Guo, R., Dawson, D. M., Price, S. L. & Florence, A. J. Reversible, Two-Step Single-Crystal to Single-Crystal Phase Transitions between Desloratadine Forms I. II. and III. Crystal Growth & Design 20, 1800-1810, doi:10.1021/acs.cgd.9b01522 (2020).
- Davey, R. J. et al. Morphology and Polymorphism of Terephthalic Acid. Molecular Crystals and Liquid Crystals Science and Technology. Section A. Molecular Crystals and Liquid Crystals 242, 79-90, doi:10.1080/10587259408037740 (1994).
- 31. Li, L. et al. Martensitic organic crystals as soft actuators. Chemical Science 10, 7327-7332, doi:10.1039/C9SC02444A (2019).
- 32. Semin, S., Li, X., Duan, Y. & Rasing, T. Nonlinear Optical Properties and Applications of Fluorenone Molecular Materials. Advanced Optical Materials 9, 2100327, doi:https://doi.org/10.1002/adom.202100327 (2021).
- Li, X., Duan, Y. & Rasing, T. H. M. Nonlinear Optical Properties and Applications of Fluorenone Molecular Materials. Advanced Optical Materials 9, 1-20, doi:http://dx.doi.org/10.1002/adom.202100327 (2021).
- 34. Xu, J. et al. Self-Assembled Organic Microfibers for Nonlinear Optics. Advanced Materials 25, 2084-2089, doi:10.1002/adma.201204237 (2013).
- Duan, Y. et al. Aggregation Induced Enhancement of Linear and Nonlinear Optical Emission from a Hexaphenylene Derivative. Advanced Functional Materials 26, 8968-8977, doi:10.1002/adfm.201602765 (2016).
- Duan, Y., Semin, S., Tinnemans, P., Xu, J. & Rasing, T. Fully Controllable Structural Phase Transition in Thermomechanical Molecular Crystals with a Very Small Thermal Hysteresis. Small 17, 2006757, doi:https://doi.org/10.1002/smll.202006757 (2021).
- Roitburd, A. L. & Kurdjumov, G. V. The nature of martensitic transformations. Materials Science and Engineering 39, 141-167, doi:https://doi.org/10.1016/0025-5416(79)90055-7 (1979).
- 38. inLight—Matter Interaction 1-18 (2003).
- 39. Born, M. & Wolf, E. Principles of optics: electromagnetic theory of propagation, interference and diffraction of light. (Elsevier, 2013).
- 40. Szymanski, H. A.Raman spectroscopy: theory and practice. (Springer Science & Business Media, 2012).
- 41. Grishunin, K. et al. Transient Second Harmonic Generation Induced by Single Cycle THz pulses in Ba0.8Sr0.2TiO3/MgO. Scientific Reports 9, 697, doi:10.1038/s41598-018-36686-5 (2019).
- 42. Grishunin, K. A. et al. THz Electric Field-Induced Second Harmonic Generation in Inorganic Ferroelectric. Scientific Reports 7, 687, doi:10.1038/s41598-017-00704-9 (2017).
- 43. Cornet, M., Degert, J., Abraham, E. & Freysz, E. Terahertz-field-induced second harmonic generation through Pockels effect in zinc telluride crystal. Opt. Lett. 39, 5921-5924, doi:10.1364/OL.39.005921 (2014).

- 44. Xu, J. et al. Controlling Microsized Polymorphic Architectures with Distinct Linear and Nonlinear Optical Properties. Advanced Optical Materials 3, 948-956, doi:10.1002/adom.201400637 (2015).
- Nogueira, B. A., Milani, A., Castiglioni, C. & Fausto, R. The correlation between experimental polarized Raman spectra and their density functional theory prediction in the LCAO framework: The R3c LiNbO3 crystal as a test case. *Journal of Raman Spectroscopy* 52, 995-1010, doi:https://doi.org/10.1002/jrs.6091 (2021).
- 46. Pavia, D. L., Lampman, G. M., Kriz, G. S. & Vyvyan, J. R. Introduction to spectroscopy. *Belmont, USA*, 13 (2001).
- 47. Douglas, A. S. & Donald, M. W. Principles of instrumental analysis. *Holt, Rinhart, Winston, New York* (1971).
- 48. Hu, T. C. et al. Optical spectroscopy and ultrafast pump-probe study of the structural phase transition $1T^{'}-TaTe_{2}$. Physical Review B **105**, 075113, doi:10.1103/PhysRevB.105.075113 (2022).
- 49. O'Connell, R. M. & Vogel, R. A. Abel inversion of knife-edge data from radially symmetric pulsed laser beams. *Appl. Opt.* **26**, 2528-2532, doi:10.1364/AO.26.002528 (1987).
- Plass, W., Maestle, R., Wittig, K., Voss, A. & Giesen, A. High-resolution knife-edge laser beam profiling. Optics Communications 134, 21-24, doi:https://doi.org/10.1016/S0030-4018(96)00527-5 (1997).
- Han, P., Wang, X. & Zhang, Y. Time-Resolved Terahertz Spectroscopy Studies on 2D Van der Waals Materials. Advanced Optical Materials 8, 1900533, doi:https://doi.org/10.1002/adom.201900533 (2020).
- 52. Gu, P., Tani, M., Kono, S., Sakai, K. & Zhang, X. C. Study of terahertz radiation from InAs and InSb. *Journal of Applied Physics* **91**, 5533-5537, doi:10.1063/1.1465507 (2002).
- 53. Liu, K., Xu, J., Yuan, T. & Zhang, X. C. Terahertz radiation from InAs induced by carrier diffusion and drift. *Physical Review B* **73**, 155330, doi:10.1103/PhysRevB.73.155330 (2006).
- 54. Liu, P. et al. in 2016 41st International Conference on Infrared, Millimeter, and Terahertz waves (IRMMW-THz). 1-2.
- 55. Yoshimine, I. et al. in 2018 43rd International Conference on Infrared, Millimeter, and Terahertz Waves (IRMMW-THz). 1-2.
- 56. Bach, T. et al. in 2019 44th International Conference on Infrared, Millimeter, and Terahertz Waves (IRMMW-THz). 1-1.
- 57. Shen, Y. R. Principles of nonlinear optics. (Wiley-Interscience, New York, NY, USA, 1984).
- 58. Vicario, C. *et al.* High efficiency THz generation in DSTMS, DAST and OH1 pumped by Cr:forsterite laser. *Opt. Express* **23**, 4573-4580, doi:10.1364/OE.23.004573 (2015).
- Lu, J. et al. Tunable multi-cycle THz generation in organic crystal HMQ-TMS. Opt. Express 23, 22723-22729, doi:10.1364/OE.23.022723 (2015).

- 60. Kim, P.-J. et al. Highly Efficient Organic THz Generator Pumped at Near-Infrared: Quinolinium Single Crystals. Advanced Functional Materials 22, 200-209, doi:https://doi.org/10.1002/adfm.201101458 (2012).
- 61. Ghasemlou, S. et al. Identifying and controlling the order parameter for ultrafast photoinduced phase transitions in thermosalient materials. Proceedings of the National Academy of Sciences of the United States of America (2024).
- 62. Yoshimine, I. et al. in 2019 44th International Conference on Infrared, Millimeter, and Terahertz Waves (IRMMW-THz). 1-2.
- 63. Grishunin, K. THz-control of antiferromagnetic spins. PhD Dissertation, doi:https://hdl.handle.net/2066/283336 (2022).
- 64. McCall, M. W., Hodgkinson, I. J. & Wu, Q.Birefringent thin films and polarizing elements. (World Scientific, 2014).
- Evans, J. W. The birefringent filter. JOSA 39, 229-242 (1949).
- Yang, H. et al. Optical waveplates based on birefringence of anisotropic two-dimensional layered materials. Acs Photonics 4, 3023-3030 (2017).
- 67. Chen, X. et al. Designing an excellent deep-ultraviolet birefringent material for light polarization. Journal of the American Chemical Society 140, 16311-16319 (2018).
- Zhang, X., Kang, L., Gong, P., Lin, Z. & Wu, Y. Nonlinear Optical Oxythiophosphate Approaching the Good Balance with Wide Ultraviolet Transparency, Strong Second Harmonic Effect, and Large Birefringence. Angewandte Chemie 133, 6456-6460 (2021).
- 69. Guo, J., Tudi, A., Han, S., Yang, Z. & Pan, S. Sn2B5O9Cl: A Material with Large Birefringence Enhancement Activated Prepared via Alkaline-Earth-Metal Substitution by Tin. Angewandte Chemie International Edition 58, 17675-17678, doi:https://doi.org/10.1002/anie.201911187 (2019).
- 70. Liu, S. et al. An exceptional peroxide birefringent material resulting from $d-\pi$ interactions. Angewandte Chemie 132, 9500-9503 (2020).
- 71. Gai, M., Wang, Y., Tong, T., Yang, Z. & Pan, S. ZnIO3F: Zinc iodate fluoride with large birefringence and wide band gap. Inorganic chemistry 59, 4172-4175 (2020).
- 72. Tong, T., Zhang, W., Yang, Z. & Pan, S. Series of crystals with giant optical anisotropy: A targeted strategic research. Angewandte Chemie International Edition 60, 1332-1338 (2021).
- 73. Dong, W. et al. Te 3 O 3 (PO 4) 2: a phosphate crystal with large birefringence activated by the highly distorted [TeO 5] group and antiparallel [PO 4] pseudo-layer. Journal of Materials Chemistry C 8, 9585-9592 (2020).
- 74. Bai, Z. et al. [Al (H 2 O) 6](IO 3) 2 (NO 3): a material with enhanced birefringence induced by synergism of two superior functional motifs. Chemical Communications 56, 11629-11632 (2020).
- Mutailipu, M., Zhang, M., Zhang, B., Yang, Z. & Pan, S. The first lead fluorooxoborate PbB 5 O 8 F: achieving the coexistence of large birefringence and deep-ultraviolet cut-off edge. Chemical Communications 54, 6308-6311 (2018).

- 76. Jin, C. et al. Hydroxyfluorooxoborate Na [B3O3F2 (OH) 2][B (OH) 3]: Optimizing the Optical Anisotropy with Heteroanionic Units for Deep Ultraviolet Birefringent Crystals. Angewandte Chemie (2021).
- 77. Zhang, M. et al. Rational design via synergistic combination leads to an outstanding deepultraviolet birefringent Li2Na2B2O5 material with an unvalued B2O5 functional gene. *Journal* of the American Chemical Society **141**, 3258-3264 (2019).
- 78. Sigman, M. B. & Korgel, B. A. Strongly birefringent Pb3O2Cl2 nanobelts. *Journal of the American Chemical Society* **127**, 10089-10095 (2005).
- 79. Liu, C.-K., Hsu, C.-H. & Cheng, K.-T. Temperature-independent quarter wave plate compensated liquid crystal shutter with a self-diagnostic shutter monitor. *Optics & Laser Technology* **126**, 106060 (2020).
- 80. Kragt, A. J., van Gessel, I. P., Schenning, A. P. & Broer, D. J. Temperature-Responsive Polymer Wave Plates as Tunable Polarization Converters. *Advanced Optical Materials* **7**, 1901103 (2019).
- 81. Wang, D. *et al.* Switchable ultrathin quarter-wave plate in terahertz using active phase-change metasurface. *Scientific reports* **5**, 1-9 (2015).
- Kato, K. Temperature-tuned 90/spl deg/phase-matching properties of LiB/sub 3/O/sub 5.IEEE journal of quantum electronics 30, 2950-2952 (1994).
- 83. Setaka, W. & Yamaguchi, K. Thermal modulation of birefringence observed in a crystalline molecular gyrotop. *Proceedings of the National Academy of Sciences* **109**, 9271-9275 (2012).
- 84. Fujiwara, A. *et al.* A crystalline molecular gyrotop with a biphenylene dirotor and its temperature-dependent birefringence. *CrystEngComm* **19**, 6049-6056 (2017).
- 85. Horie, M. et al. Thermally-induced phase transition of pseudorotaxane crystals: changes in conformation and interaction of the molecules and optical properties of the crystals. *Journal of the American Chemical Society* **134**, 17932-17944 (2012).
- 86. Wang, F., Huber, L., Maehrlein, S. F. & Zhu, X.-Y. Optical Anisotropy and Phase Transitions in Lead Halide Perovskites. *The Journal of Physical Chemistry Letters* **12**, 5016-5022 (2021).
- 87. Duan, Y. et al. Aggregation induced enhancement of linear and nonlinear optical emission from a hexaphenylene derivative. Advanced Functional Materials 26, 8968-8977 (2016).
- 88. Zhan, Y., Xu, Y., Jin, Z., Ye, W. & Yang, P. Phenothiazine substituted phenanthroimidazole derivatives: Synthesis, photophysical properties and efficient piezochromic luminescence. *Dyes and Pigments* **140**, 452-459, doi:https://doi.org/10.1016/j.dyepig.2017.01.070 (2017).
- 89. Wheeler, D. A. & Zhang, J. Z. Exciton Dynamics in Semiconductor Nanocrystals. *Advanced Materials* **25**, 2878-2896, doi:https://doi.org/10.1002/adma.201300362 (2013).
- 90. Di, Q. et al. Fluorescence-based thermal sensing with elastic organic crystals. *Nature Communications* **13**, 5280, doi:10.1038/s41467-022-32894-w (2022).
- Wang, J.-X. et al. Tunable Fluorescence and Afterglow in Organic Crystals for Temperature Sensing. The Journal of Physical Chemistry Letters 13, 1985-1990, doi:10.1021/acs.jpclett.2c00168 (2022).

- 92. Chen, W., Wang, W., Zhang, Y., Zhang, S. & Long, X. Physical mechanism underlying temperature effects on phase retardation. Applied optics 51, 4569-4573 (2012).
- 93. Koshima, H., Taniguchi, T. & Asahi, T. in Mechanically Responsive Materials for Soft Robotics 57-82 (2020).
- 94. Chung, H. et al. Single Atom Substitution Alters the Polymorphic Transition Mechanism in Organic Electronic Crystals. Chemistry of Materials 31, 9115-9126, doi:10.1021/ acs.chemmater.9b03436 (2019).
- 95. 이상연 & Society, 부. J. B. o. t. K. C. Molecular structure and vibrational spectra of 9-fluorenone density functional theory study. 17, 760-764 (1996).
- Florence, G. E., Bruce, K. A., Shepherd, H. J. & Gee, W. J. Metastable 9-Fluorenone: Blueshifted Fluorescence, Single-Crystal-to-Single-Crystal Reactivity, and Evaluation as a Multimodal Fingermark Visualization Treatment. Chemistry - A European Journal 25, 9597-9601, doi:https:// doi.org/10.1002/chem.201901301 (2019).
- 97. Wang, J., Li, Y., Wu, S., Song, P. & Xia, L. Chemical mechanism of surface-enhanced Raman scattering via charge transfer in fluorenone-Ag complex. Journal of Physics: Condensed Matter 28, 214002, doi:10.1088/0953-8984/28/21/214002 (2016).
- 98. Schneider, T., Srinivasan, G. & Enz, C. P. Phase Transitions and Soft Modes. Physical Review A 5, 1528-1536, doi:10.1103/PhysRevA.5.1528 (1972).
- Scott, J. F. Soft-mode spectroscopy: Experimental studies of structural phase transitions. Reviews of Modern Physics 46, 83-128, doi:10.1103/RevModPhys.46.83 (1974).
- 100. Bosshard, C., Spreiter, R., Degiorgi, L. & Günter, P. Infrared and Raman spectroscopy of the organic crystal DAST: Polarization dependence and contribution of molecular vibrations to the linear electro-optic effect. Physical Review B 66, 205107, doi:10.1103/PhysRevB.66.205107 (2002).
- 101. Gao, C. et al. Stability and Phase Transition of Metastable Black Arsenic under High Pressure. The Journal of Physical Chemistry Letters 11, 93-98, doi:10.1021/acs.jpclett.9b03148 (2020).
- 102. Turrell, G.Infrared and raman spectra of crystals. (Academic Press, 1972).
- 103. Zhang, K. et al. Raman signatures of inversion symmetry breaking and structural phase transition in type-II Weyl semimetal MoTe2. Nature Communications 7, 13552, doi:10.1038/ ncomms13552 (2016).
- 104. Loudon, R. The Raman effect in crystals. Advances in Physics 50, 813-864, doi:10.1080/00018730110101395 (2001).
- 105. Aroyo, M. I., Kirov, A., Capillas, C., Perez-Mato, J. M. & Wondratschek, H. Bilbao Crystallographic Server. II. Representations of crystallographic point groups and space groups. Acta Crystallographica Section A 62, 115-128, doi:doi:10.1107/S0108767305040286 (2006).
- 106. Genet, F., Loridant, S., Ritter, C. & Lucazeau, G. Phase transitions in BaCeO3: neutron diffraction and Raman studies. Journal of Physics and Chemistry of Solids 60, 2009-2021, doi:https:// doi.org/10.1016/S0022-3697(99)00031-1 (1999).

- 107. Tenne, D. A. et al. Single crystals of the organic semiconductor perylene tetracarboxylic dianhydride studied by Raman spectroscopy. Physical Review B 61, 14564-14569, doi:10.1103/PhysRevB.61.14564 (2000).
- 108. Loudon, R. The Raman effect in crystals. *Advances in Physics* **13**, 423-482, doi:10.1080/00018736400101051 (1964).
- Rao, R., Sakuntala, T. & Deb, S. K. Order-disorder transition in triethylenediamine: A Raman scattering study. *Journal of Molecular Structure* 789, 195-199, doi:https://doi.org/10.1016/j.molstruc.2005.12.025 (2006).
- 110. Rao, R. et al. High pressure Raman scattering studies on adamantane. The Journal of Chemical Physics 112, 6739-6744, doi:10.1063/1.481227 (2000).
- 111. Galimberti, D. R., Milani, A., Tommasini, M., Castiglioni, C. & Gaigeot, M.-P. Combining Static and Dynamical Approaches for Infrared Spectra Calculations of Gas Phase Molecules and Clusters. *Journal of Chemical Theory and Computation* 13, 3802-3813, doi:10.1021/acs.jctc.7b00471 (2017).
- 112. Maggiore, E., Galimberti, D. R., Tommasini, M., Gaigeot, M.-P. & Ossi, P. M. The contribution of surfaces to the Raman spectrum of snow. *Applied Surface Science* 515, 146029, doi:https://doi.org/10.1016/j.apsusc.2020.146029 (2020).
- Ivanov, M. et al. Thickness-Dependent High-Temperature Piezo- and Ferro-Electricity in a Fluorenone-Based Molecular Crystal. Advanced Materials Interfaces 9, 2201103, doi:https://doi.org/10.1002/admi.202201103 (2022).
- 114. Ghasemlou, S. *et al.* Identifying and controlling the order parameter for ultrafast photoinduced phase transitions in thermosalient materials. *Proceedings of the National Academy of Sciences* **121**, e2408366121, doi:10.1073/pnas.2408366121 (2024).
- 115. Ahmed, E. et al. Ultrafast, Light, Soft Martensitic Materials. Advanced Functional Materials 32, 2112117, doi:https://doi.org/10.1002/adfm.202112117 (2022).
- 116. Naumov, P., Chizhik, S., Commins, P. & Boldyreva, E. Bending, Jumping, and Self-Healing Crystals. *Mechanically Responsive Materials for Soft Robotics*, 105-138 (2020).
- Tao, S. et al. Relaxation Dynamics of Photoexcited Excitons in Rubrene Single Crystals Using Femtosecond Absorption Spectroscopy. *Physical Review Letters* 109, 097403, doi:10.1103/PhysRevLett.109.097403 (2012).
- 118. Camposeo, A. *et al.* Polarized superradiance from delocalized exciton transitions in tetracene single crystals. *Physical Review B* **81**, 033306, doi:10.1103/PhysRevB.81.033306 (2010).
- 119. Wu, T., Ni, W., Gurzadyan, G. G. & Sun, L. Singlet fission from upper excited singlet states and polaron formation in rubrene film. RSC Advances 11, 4639-4645, doi:10.1039/D0RA10780H (2021).
- 120. Jin, Z. *et al.* Photoinduced large polaron transport and dynamics in organic–inorganic hybrid lead halide perovskite with terahertz probes. *Light: Science & Applications* **11**, 209, doi:10.1038/s41377-022-00872-y (2022).

- 121. Ma, L. et al. Singlet fission in rubrene single crystal: direct observation by femtosecond pumpprobe spectroscopy. Physical Chemistry Chemical Physics 14, 8307-8312, doi:10.1039/C2CP40449D (2012).
- 122. Cabanillas-Gonzalez, J. et al. Two-step field-induced singlet dissociation in a fluorene trimer. Physical Review B 71, 155207, doi:10.1103/PhysRevB.71.155207 (2005).
- 123. Li, X. et al. Strong optical nonlinearities of self-assembled polymorphic microstructures of phenylethynyl functionalized fluorenones. Chinese Chemical Letters 29, 297-300, doi:https://doi.org/10.1016/j.cclet.2017.11.001 (2018).
- 124. Zheng, Y. et al. Self-assembled organic nonlinear optical crystals based on pyridine derived fluorenone. Materials Chemistry Frontiers 7, 698-704, doi:10.1039/D2QM01173E (2023).
- 125. Kissin, P. et al. Quasiparticle relaxation dynamics in URu_{2-x}Fe_xSi₂ single crystals. Physical Review B 99, 165144, doi:10.1103/PhysRevB.99.165144 (2019).
- 126. Fausti, D. et al. Light-Induced Superconductivity in a Stripe-Ordered Cuprate. Science 331, 189-191, doi:10.1126/science.1197294 (2011).
- 127. Mitrano, M. et al. Possible light-induced superconductivity in K3C60 at high temperature. Nature 530, 461-464, doi:10.1038/nature16522 (2016).
- 128. de Jong, S. et al. Speed limit of the insulator-metal transition in magnetite. Nature Materials 12, 882-886, doi:10.1038/nmat3718 (2013).
- 129. Beaud, P. et al. A time-dependent order parameter for ultrafast photoinduced phase transitions. Nature Materials 13, 923-927, doi:10.1038/nmat4046 (2014).
- 130. Radu, I. et al. Transient ferromagnetic-like state mediating ultrafast reversal of antiferromagnetically coupled spins. Nature 472, 205-208, doi:10.1038/nature09901 (2011).
- 131. Mangin, S. et al. Engineered materials for all-optical helicity-dependent magnetic switching. Nature Materials 13, 286-292, doi:10.1038/nmat3864 (2014).
- 132. Li, G. et al. Ultrafast kinetics of the antiferromagnetic-ferromagnetic phase transition in FeRh. Nature Communications 13, 2998, doi:10.1038/s41467-022-30591-2 (2022).
- 133. Zhang, Z. et al. Terahertz-field-driven magnon upconversion in an antiferromagnet. Nature Physics 20, 788-793, doi:10.1038/s41567-023-02350-7 (2024).
- 134. Domröse, T. et al. Light-induced hexatic state in a layered quantum material. Nature Materials 22, 1345-1351, doi:10.1038/s41563-023-01600-6 (2023).
- 135. Ferguson, B. & Zhang, X.-C. Materials for terahertz science and technology. Nature Materials 1, 26-33, doi:10.1038/nmat708 (2002).
- 136. Blank, T. G. H. et al. Two-Dimensional Terahertz Spectroscopy of Nonlinear Phononics in the Topological Insulator MnBi₂Te₄. Physical Review Letters **131**, 026902, doi:10.1103/PhysRevLett.131.026902 (2023).
- 137. Mashkovich, E. A. et al. Terahertz light-driven coupling of antiferromagnetic spins to lattice. Science 374, 1608-1611, doi:10.1126/science.abk1121 (2021).

- 138. Mashkovich, E. A. *et al.* Terahertz Optomagnetism: Nonlinear THz Excitation of GHz Spin Waves in Antiferromagnetic FeBO₃. *Physical Review Letters* **123**, 157202, doi:10.1103/PhysRevLett.123.157202 (2019).
- 139. Sitnikov, D. S. *et al.* Estimation of THz field strength by an electro-optic sampling technique using arbitrary long gating pulses. *Laser Physics Letters* **16**, 115302, doi:10.1088/1612-202X/ab4d56 (2019).
- 140. Saeedi, K. et al. Short lifetime components in the relaxation of boron acceptors in silicon. Physical Review B 97, 125205, doi:10.1103/PhysRevB.97.125205 (2018).
- 141. Glinka, Y. D. *et al.* Ultrafast dynamics of interfacial electric fields in semiconductor heterostructures monitored by pump-probe second-harmonic generation. *Applied Physics Letters* **81**, 3717-3719, doi:10.1063/1.1521573 (2002).

